Baryon stopping and quark-gluon plasma production at RHIC and LHC

Dissertation
zur Erlangung des Doktorgrades
der Naturwissenschaften

vorgelegt beim Fachbereich Physik
der Johann Wolfgang Goethe–Universität
in Frankfurt am Main

von
Konstantin Lyakhov
aus Moskau (Russland)

Frankfurt am Main 2008
(D 30)

vom Fachbereich Physik der Johann Wolfgang Goethe–Universität
als Dissertation angenommen

Dekan . . . .

Gutachter . . . .

Datum der Disputation . . . .

I dedicate this thesis to my mam Lyakhova Olga Victorovna

0.1 abstract

Strong chromofields developed at early stages of relativistic heavy-ion collisions give rise to the collective deceleration of net baryons from colliding nuclei. We have solved classical equations of motion for baryonic slabs under the action of time-dependent chromofield. We have studied sensitivity of the slab trajectories and their final rapidities to the initial strength and decay pattern of the chromofield as well as to the back reaction of produced plasma. This mechanism can naturally explain significant baryon stopping observed at RHIC, an average rapidity loss $\langle \delta y \rangle \approx 2$. Using a Bjorken hydro-dynamical model with particle producing source we also study the evolution of partonic plasma produced as the result of chromofield decay. Due to the delayed formation and expansion of plasma its maximum energy density is much lower than the initial energy density of the chromofield. It is shown that the net-baryon and produced parton distributions are strongly correlated in the rapidity space. The shape of net-baryon spectra in midrapidity region found in the BRAHMS experiment cannot be reproduced by only one value of chromofield energy density parameter ϵ_0, even if one takes into account novel mechanisms as fluctuations of color charges generated on the slab surface, and weak interaction of baryon-rich matter with produced plasma. The further step to improve our results is to take into account rapidity dependence of saturation momentum as explained in thesis. Different values of parameter ϵ_0 has been tried for different variants of chromofield decay to fit BRAHMS data for net-baryon rapidity distribution. In accordance with our analysis, data for fragmentation region correspond to the lower chromofield energy densities than mid-rapidity region. χ^2 analysis favors power-law of chromofield decay with corresponding initial chromofield energy density of order $\epsilon_f = 30 GeV/fm^3$.

0.2 Übersicht

Starke Farbfelder, die früh in relativistischen Schwerionenkollisionen entstehen, sorgen für das kollektive Abbremsen von Baryonen der kollidierenden Kerne. In dieser Arbeit werden die klassischen Bewegungsgleichungen für diese Baryonen unter der Einwirkung von zeitabhängigen Farbfeldern gelst. Darber hinaus wird die Abhängigkeit der Trajektorien und ihrer Endrapiditäten

von der anfänglichen Stärke und dem Zerfallsmuster des Farbfeldes sowie von der Rückreaktion des produzierten Plasmas untersucht. Dieser Mechanismus kann mit einem mittlerem Rapiditätsverlust von $\langle \delta y \rangle \approx 2$ auf natürliche Weise das deutliche Baryonenstoppen erklären, welches am RHIC beobachtet wurde. In einem Bjorken-hydrodynamischen Modell mit einer Teilchen-erzeugenden Quelle untersuchen wir auch die Evolution des partonischen Plasmas, das durch den Zerfall des Farbfeldes produziert wird. Aufgrund der verzögerten Bildung und der Expansion des Plasmas ist seine maximale kinetische Energiedichte viel kleiner als die anfängliche Energiedichte des Farbfeldes. Es wird gezeigt, dass die Verteilungen der Baryonen und der erzeugten Partonen im Rapiditätsraum stark korreliert sind. Die Form der Netto-Baryonen Spektren im mittleren Rapiditätsbereich des BRAHMS Experimentes kann nur reproduziert werden wenn man neuartige Mechanismen berücksichtigt, welche die Fluktuationen der auf der Scheibchenoberfläche erzeugten Farbladungen und die schwache Wechselwirkung der Baryonenreichen Materie mit dem produzierten Plasma berücksichtigen. Es zeigt sich, dass alle getesteten Varianten des Zerfalls des Farbfeldes die mittlere Rapiditätsregion reproduzieren können, wenn der Paramter ϵ_0 variiert wird, welcher in die Abschätzung der anfänglichen Energiedichte eingeht.

0.3 Zusammenfassung

Die betrachteten Strahlenergien in relativistischen Schwerionen Experimenten sind so hoch, daß die kollidierenden Kerne vor der Kollision als dünne, Lorentz-kontrahierte Blätter angesehen werden können. Jedes Blatt ist aufgeteilt in kleinere Elemente oder Scheibchen der Fläche σ_a mit Index a, wobei $a = p$ für den Projektilkern und $a = t$ für den Targetkern steht. Jede dieser Scheibchen ist charakterisiert durch die Baryonenzahl N_a, die als erhalten angenommen wird.

Wir zerteilen die Kern-Kern Kollision in eine Vielzahl von paarweisen Kollisionen der Scheibchen von Projektil- und Targetkern. Darüber hinaus nehmen wir an, daß vor und nach der Überdeckung bei $t = 0$, jede Scheibchen als starrer Körper entlang der Strahlaxe z propagiert. Energie und Geschwindigkeit einer Scheibchen a sind parametrisiert durch ihre Masse M_a und ihre longitudinale Geschwindigkeit Y_a,

$$E_a = M_a \cosh Y_a \ , \quad P_a = M_a \sinh Y_a \tag{1}$$

Es ist sinnvoll, M_a durch

$$M_a = m_\perp \tilde{N}_a \tag{2}$$

auszudrücken, wobei $m_\perp = \sqrt{m_N^2 + \langle p_\perp \rangle_\tau^2}$ die anfängliche Energie pro Baryon bzw. die tranversale Masseïst. Diese wird ausgedrückt durch den durchschnittlichen transversalen Impuls $\langle p_\perp \rangle_\tau$. Wie später gezeigt werden wird, hängt die zeitliche Entwicklung von $\langle p_\perp \rangle_\tau$ von der Plasmarückkopplung ab, Gleichung (2).

Im Glauber Modell ist die durchschnittliche Anzahl der an der Kollision beteiligten Protonen und Neutronen des Kerns a bei einem Stoßparameter von **b** und einem Radius von **s** gegeben durch:

$$\tilde{N}_a(b, s) = A_a T_a(b, s)(1 - (1 - \sigma_{NN} T_{\bar{a}}(b, s))^{A_{\bar{a}}}) \tag{3}$$

Die Verteilung der Baryonenzahl in der transversen Ebene ist gegeben durch die Integration des Woods-Saxon Profils $\rho(\mathbf{r})$ entlang der Strahlaxe

$$N_a = \int \rho(\mathbf{r})dz \equiv A_a T_a(\mathbf{b}, \mathbf{s}) \quad, \tag{4}$$

worin die normalisierte Profilfunktion T_a eingeführt wurde. Die Anzahl der Nukleon-Nukleon Kollisionen in einem Zylinder mit Querschnitt σ ist gegeben durch:

$$N_{coll}(\mathbf{b}, \mathbf{s}) = \sigma \sigma_{NN} N_p(\mathbf{b} - \mathbf{s}) N_t(\mathbf{s}) \tag{5}$$

mit $\sigma_{NN} = 4.21 fm^2$ für inelastische Nukleon-Nukleon Kollisionen bei RHIC Energien. Der Parameter $0 < \beta < 1$ kontrolliert den Grad des String-Durchflusses. Für unabhängige Strings, die zwischen den Scheibchen gespannt sind ist $\beta = 1$ und für überlappende Strings ist $\beta = 0.5$. In den folgenden Rechnungen ist der Zylinderquerschnitt gleich dem Wirkungsquerschnitt für inelastische Nukleon-Nukleon Kollisionen. Für $\beta = 1$ sind die Ergebnisse alledings unabhängig hiervon, wie später gezeigt werden wird.

Die Gleichungen für die Scheibchentrajektorien und für die Zeitentwicklung ihrer Massen und Geschwindigkeiten wurden unter der Annahme expliziter Energie-Impuls-Erhaltung in den Scheibchen hergeleitet. Die Erzeugung und Entwicklung des Plasmas wird durch einfache Gleichungen beschrieben, die auf Bjorken Hydrodynamik basieren, mit zusätzlichen phenomenologischen Quellentermen um den Feldzerfall zu berücksichtigen. Wir haben drei Möglichkeiten für den Feldabfall in Betracht gezogen: exponentiell, polynomisch (ein solcher Abfall folgt aus dem Schwinger Mechanismus) und eine Möglichkeit die sich aus den Anfangsbedinungen für ein Farbglaskondensat (Color Glass Condensate, CGC) ergibt. Wir konnten experimentelle Ergebnisse für den polynomischen Zerfall mit vernünftigen Abfallszeiten von ungefähr 0.6 fm reproduzieren. Wir haben zwei verschiedene Varianten von Rechnungen betrachtet. In der ersten wird angenommen, daß

die Scheibchendynamik von dem produzierten Plasma in Einklang mit der Energie-Impuls-Erhaltung beeinflußt wird. Es konnte gezeigt werden, daß wegen der verzögerten Bildung die maximale Energiedichte des Plasmas nur 20%-40% der anfänglichen Energiedichte des Feldes erreicht. Die Baroyon-reichen und Baryon-freien Komponenten des QGP werden als ideale Flüssigkeiten angesehen. Die Wechselwirkung zwischen diesen zwei Flüssigkeiten führt zu einer ansteigenden Temperatur der Scheibchen und somit zu einem Zuwachs an transversalem Impuls der Baryonen. Der experimentelle Wert von $\langle p_\perp \rangle \approx 1 GeV$ ergibt so eine Obergrenze für die Scheibchen-Plasma Wechselwirkung. Es wurde beobachtet, daß Baryon-reiche Materie nur bis zu einem begrenzten Wert aufgeheizt wird. Die Plasmarückkopplung führt zu einer Sättigung der Abbremsung mit steigender Farbfeldenergiedichte, oder mit anderen Worten, steigender Strahlenergie. Es ist interessant, daß die experimentellen Daten ein logarithmisches Verhalten anstelle eines linearen Anstiegs zeigen. Da der Einfachheit halber eine boost-invariante Verteilung der produzierten Partonenangenommen wurde, ist der Einfluß des Plasmas derartig groß. Das bedeutet auch, daß die Randeffekte vernachlässigt worden sind. Um dieses Problem zu beheben, können Anfangsbedingungen gewählt werden, die die endliche Ausdehnung der partonischen Flüssigkeit berücksichtigen, für ihre weitere, isentropische Entwicklung. Es ist wichtig, sich klarzumachen, daß unser Modell eine drastische Vereinfachung der realen physikalischen Prozesse darstellt.

Eine angemessene Untersuchung der Rückkopplungseffekte sollte auf einem mikroskopischen Verständnis der Teilchenproduktion in einem starken, zeitabhängigen und endlich ausgedehnten Feld basieren. Im Prinzip kann dies auf der Grundlage der Quantenfeldtheorie (QFT) oder von kinetischen Theorie stattfinden. Für eine komplette Lösung des Problems mit Hilfe der Quantenchromodynamik müsste ein Satz gekoppelter Gleichungen, inklusive der Dirac und Yang-Mills Gleichung gelöst werden. Da dies ein sehr schwieriges Unterfangen ist, ist es wünschenswert, eine praktizierbare Methode zu finden. Diese Methode sollte eine direkte Verbindung zwischen Feldtheorie und kinetischer Theorie beinhalten. Allerdings, ist die Verbindung der beiden bis heute nicht genau bekannt und sie zu finden stellt eine ebenso anspruchsvolle Herausforderung dar.

Betrachten wir nun den Einfluß starker Farbfelder auf die netto-Baryonen Geschwindigkeitsverteilung. Unsere Rechnungen zeigen, daß sich die Fragmentationsregion der netto-Baryon Spektren von den Anfangsgeschwindigkeiten zu zentraleren Geschwindigkeiten verschiebt, ein Effekt dessen Größe von der Anfangsenergiedichte der Farbfelder abhängt. Andererseits wächst die Rückkopplung des produzierten Plasmas mit zunehmender Farbfeldstärke an, was die Baryonverteilung aus der Region mittlerer Geschwindigkeiten

in die usseren Regionen verschiebt. Unsere Rechnungen für diesen Fall zeigen, daß die Region mittlerer Geschwindigkeiten fast frei von netto-Baryonen bleibt, unabhängig von der anfänglichen Energiedichte des Farbfeldes.

Eine andere extreme Annahme ist, daß das produzierte partonische Plasma keinen Einfluß auf die Dynamik der Baryonen hat. In diesem Fall ist die Geschwindigkeitsverschiebung in Richtung zentraler Geschwindigkeiten groß genug, um den durchschnittlichen Geschwindigkeitsverlust zu erklären. Allerdings kann die Verteilung der netto-Baryonen Geschwindigkeiten nicht mit festen Farbfeldwerten reproduziert werden. Um BRAHMS Daten zu reproduzieren haben wir die Farbladung als eine Gaußsche Zufallsvariable angenommen. Genauer gesagt ist im Einklang mit dem McLerran-Venugopalan Modell die Farbladung eine klassische Zufallsvariable, die innerhalb einer Region der transversalen Ausdehnung $\frac{1}{Q_s}$ fluktuiert, wobei Q_s die sogenannte Saturationsskala ist. Die durchschnittliche Farbladung in dieser Region ist natürlich gleich Null. Auf diese Weise können physikalische Größen wie die Anzahl der emittierten Partonen oder der netto-Baryonen Geschwindigkeitsverlust ausgewertet werden, indem man über viele verschiedene Events, korrespondierend zu verschiedenen Anfangsbedingungen, mittelt. Auf diese Weise werden die Beiträge von höheren Energiedichten mit angemessenen statistischen Gewichten berücksichtigt.

Die beste Übereinstimmung mit experimentellen Daten wurde für Stapel erziehlt, die sich unabhängig vom produzierten Plasma bewegen, bei einem polynomischen Farbfeldabfall mit anfänglichen Farbfeldenergiedichten von ungefähr $30 GeV/fm^3$. In diesem Fall wird ein transversaler Baryonenimpuls nur bei den anfänglichen, harten Prozessen generiert. Geschwindigkeitsverteilungen von netto-Baryonen und produzierten Partonen wurden für unterschiedliche Zentralitäten berechnet. Die Mittelung über die Zentralitäten wurde unter Annahme der Wood-Saxon Verteilung der Nukleonen im Kern durchgeführt. Es wurde gezeigt, daß Fluktuationen der Farbladung helfen, die Regionen mittlerer Geschwindigkeit in der netto-Baryonen Geschwindigkeitsverteilung zu füllen. Die Berechnungen wurden unter Vernachlässigung einer Rückkopplung des produzierten Plasmas durchgeführt, da nur so eine gute Übereinstimmung mit den BRAHMS Daten bei mittleren Geschwindigkeiten erzielt werden konnte. Hieraus ziehen wir die Schlußfolgerung, daß die Randeffekte bei der Partonenproduktion sehr wichtig sind, genauer gesagt, daß die Dichte der produzierten Partonen in der Nähe der Stapel stark abnimmt. Der netto-Baryonen Geschwindigkeitsverlust in Gold-Gold Kollisionen bei RHIC Energien $\langle \delta y \rangle \approx 1.5 - 4$ kann durch die Wirkung von Farbfelder mit anfänglichen Energiedichten von ungefähr $17 - 83 GeV/fm^3$ erklärt werden. Eine Extrapolation zu LHC Energien ermöglicht es eine Prognose von

$\langle \delta y \rangle \approx 3.5 - 6.5$ und anfänglichen Feldenergiedichten von $45 - 224 GeV/fm^3$.

Contents

Chapter 1

Introduction

The goal of this dissertation is to develop a simple dynamical model for ultra-relativistic heavy ion collisions which includes explicitly strong chromofields generated at early stage of the collision. There exist various suggestions concerning the space-time structure of these fields from string-like configurations as in the color flux-tube model [1] to merely transverse configurations of the Weizscker-Williams type [2]. The decay of these fields will eventually lead to the creation of Quark Gluon Plasma (QGP). This process has been studied by several authors under different assumptions about the field decay mechanism (see e. g. Refs. [3, 4, 5, 6]). Obviously, search for the QGP is closely related to one of the basic problems of the modern elementary particle physics: verification of Quantum Chromodynamics (QCD) as the true theory of strong interactions. Importance of such investigations does not call any doubt because of urgent necessity to interpret recent RHIC data and to propose new ideas for coming soon experiments at LHC. It should be mentioned that current experimental data, at least for SPS and lower energies, do not exclude purely hadronic scenarios for evolution of produced system, as shown by ultrarelativistic Quantum Molecular Dynamics (uRQMD) [7] and Hadron String Dynamics (HSD) [8] models. At the same time, results of SPS experiments can be also reproduced by combination of parton and hadron pictures as it was done in [9] by using quark Molecular Dynamics(qMD) model, where only initial and final stage of evolution are described in terms of hadronic degrees of freedom. It should be mentioned that quark matter is expected to exist not only in experimentally controlable situation but also in nature, where superdense baryonic matter can be formed in such astrophysical objects as neutron stars and hypothetical quark stars, [10].

Heavy-ion physics has a long and ambiguous history. Fermi was the first who applied methods of statistical physics to study relativistic hadron collisions [11]. Later Landau proposed a hydrodynamical model where complete

stopping of produced matter in the boost contracted volume was assumed
[12]. This model predicts a gaussian shape for the rapidity distributions of
produced particles which is in agreement with experimental data. Later on,
Bjorken has proposed a scaling model, which takes into account finite forma-
tion time of produced particles [13]. This model predicts a plateau in rapidity
distribution, which height depends on the c.m. energy. Ideas of Landau were
not fully accepted because Quantum Field Theory(QFT) of Strong Interac-
tions had a hard times in this period. Because of that it was not possible
to prove classical limit of such ill-developed theory. It took almost 20 years
with invention of QCD to understand that classical approach is natural way
for describing relevant phenomena. Therefore success of Landau model in
describing of data for multiparticle production was not accidental.

Recently a remarkable success in explaining hadron yield ratios was demon-
strated by simple thermal models [14]. The experimental data can be well
fitted with only three parameters: the temperature, the volume and the
baryonic chemical potential μ_b of the hadron gas at the point of the chem-
ical Freeze-Out (F-O). These models can even reproduce hadron yields in
e^+e^- and hh collisions, where thermal equilibrium is not expected [15]. This
can be explained rather by phase space population than by established local
thermal equilibrium. Indeed, elementary collisions do not exhibit hydrody-
namical behavior at all because analysis of hadronic spectra shows little sign
of the transverse expansion predicted by the hydrodynamical description of
produced system. Thus, the excited systems produced in these elementary
collisions are not macroscopic. In contrast, relativistic heavy ion collisions
show evidence for a hydrodynamic expansion. Momentum correlations as-
sociated with collective flow are observed at SPS and RHIC. This is firmly
established by a combined analysis of particle spectra and HBT correlations.
In non-central collisions soft particles ($p_t < 2GeV$) reveal the so called ellip-
tic flow. Certainly, hydrodynamics is not valid when the mean free path of
particles becomes too long and one must impose a certain F-O criterion in
order to compare the observed hadron spectra to hydro calculations.

Up to now there is no completely computable dynamical theory (like
Magneto-Hydrodynamics for QED plasmas), which is able to describe con-
sistently the overall evolution of produced system in relativistic heavy-ion
collisions. Much more rich structure of QCD and nonperturbative nature of
the confinement put the limit on the applicability of the QCD to realistic
situations in experiment. Serious restrictions are also imposed by limited
performance of modern computers since the lattice QCD which is assigned
to explore nonperturbative region become exact only in continuum limit.
Another difficulty is so-called sign problem, which arises in calculations at
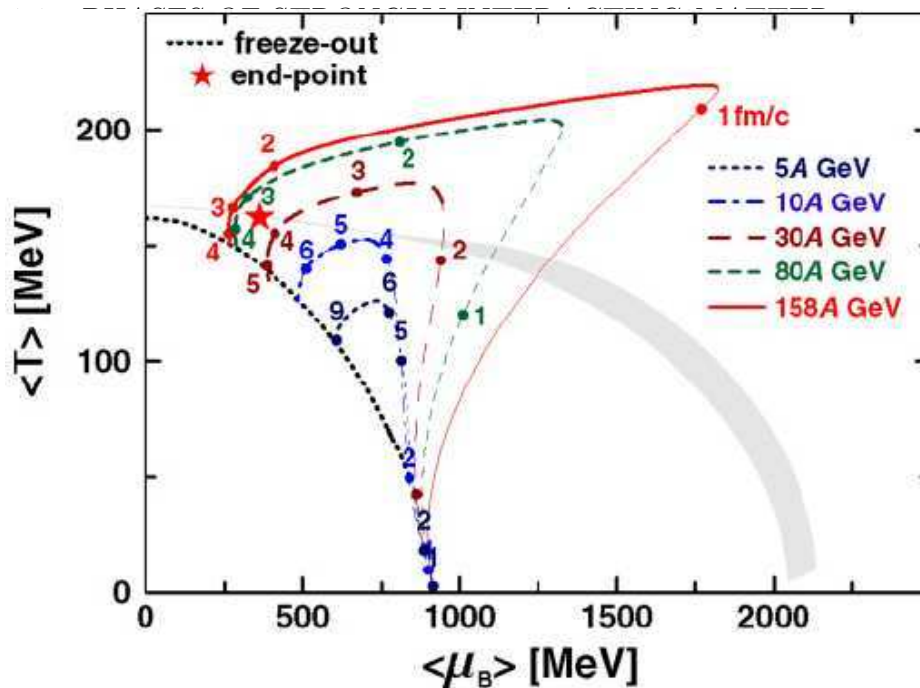finite baryon density. Therefore theorists working with lQCD must exercise

Figure 1.1: Dynamical trajectories for central(**b**=2.5 fm) Pb+Pb collisions for various bombarding energies, calculated within the relativistic 3-fluid hydrodynamics with hadronic EoS [17]. Numbers near the trajectories correspond to the different times after the first contact of nuclei. The phase boundary is obtained in a two-phase bag model [22]. Critical end-point calculated in the lattice QCD [23] is marked by the star and shaded region corresponds to the uncertainties of the bag model.

caution to separate really valuable physical information from various lattice artefacts. Equation of state of baryon-free matter is one of the most important outcomes of lattice calculations so far. Lattice results show that even at temperature much larger than the deconfinement temperature T_c the equation of state is still by $15\% - 20\%$ away from the ideal gas limit [16]. For RHIC energies corresponding to $1.25T_c < T < 2.4T_c$ and higher this is still the case. This fact is usually interpreted as an indication that the residual interactions are still present.

1.1 Phases of strongly interacting matter

A convenient way to present a variety of possible states accessible in heavy ion collisions with different beam energies is to look at the trajectories in the temperature-baryon density plane shown in the Fig.1.1. One can see that the higher is beam energy the more compressed and heated system is produced.

The degree of compression and heating of baryon-rich matter at low energies is related with the entropy generated on a strongly nonequilibrium stage of the collision. Within the three-fluid model [17] this entropy is determined by inter-fluid friction acting on this stage. However uncertainties of calculations in this model are still large, since these dynamical trajectories were calculated for pure hadronic gas equation of state, and in the presence of a phase transition they may be strongly modified. Near the phase transition the strongly interacting QCD system behaves like a liquid rather than a gas, as it was clarified recently at small μ_B from both partonic [18] and hadronic [19] side. In the limit of vanishing baryon density the deconfinement temperature practically coincides with the transition temperature for chiral symmetry restoration. What happens at larger baryon densities is a completely open question. It is worth to mention that low energy experiments are very important to investigate the transition region on the phase diagram between confined and deconfined phases. The experimental programs at FAIR in GSI(Darmstadt) [20], and at Nuclotron in JINR(Dubna) are assigned to investigate this mixed phase region, [21].

1.2   Picture of relativistic heavy ion collision

One can devide collision process into the following stages:

1. Initial Conditions. Formation of coherent chromofield.

2. Decay of chromofields to incoherent QGP.

3. Thermalization process which can be studied by some of transport models: Parton Cascade Model(PCM), uRQMD, HSD.

4. Hydrodynamic evolution of deconfined matter.

5. Hadronization or dynamical mechanism of parton-hadron conversion by parton recombination mechanism employed in macroscopic approach or color neutral clusters fragmentation as it was implemented in qMD model [9].

6. Hadron transport: The final state interactions of the expanding dense hadronic matter prior to F-O.

7. Freeze-Out

The schematic picture of collision is visualized in Fig.1.2. The time interval between hadronization and F-O hypersurfaces (F-Oh) depends on a hadron
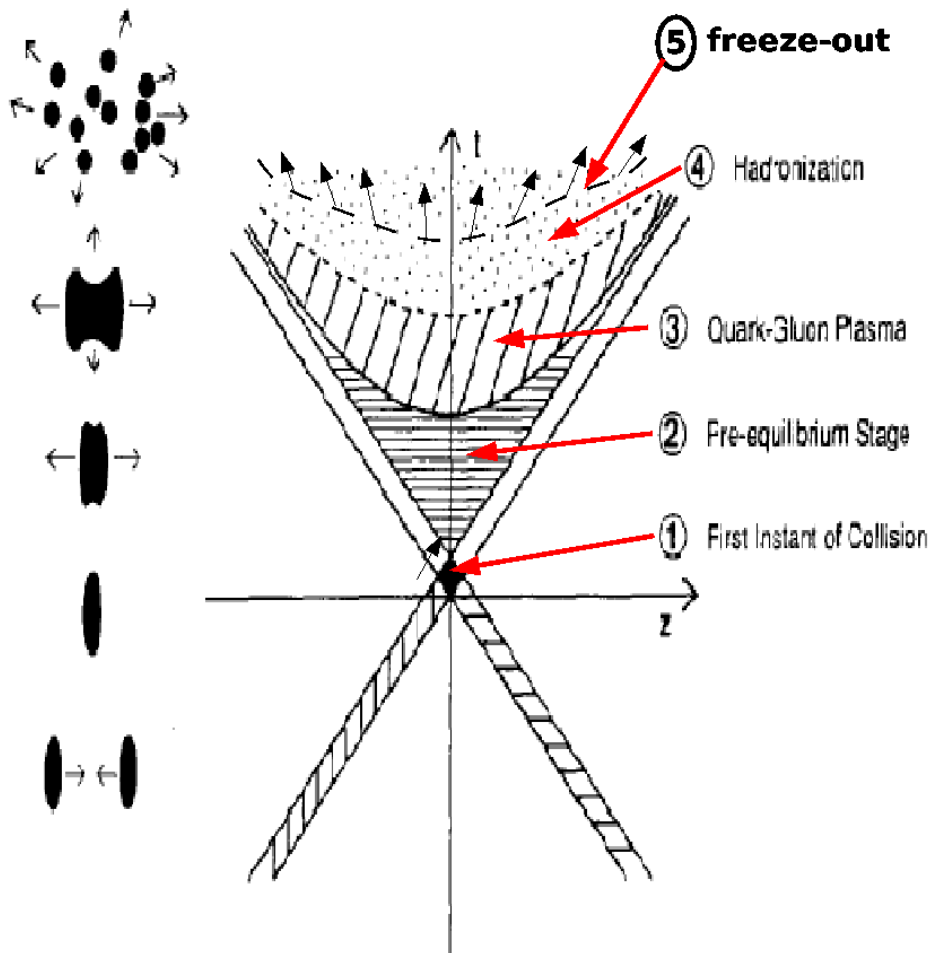
Figure 1.2: Space-time diagram of the longitudinal evolution of a relativistic nucleus-nucleus collision from the first moment of collision, via preequilibrium stage and quark-gluon plasma to the final hadron formation and Freeze-Out.

emission time. At RHIC energies both hypersurfaces practically coinside due to extremely short hadron emission time measured in the local frame [24].

1.3   Physics of initial state

There are two generic approaches to derive initial conditions for high energy A+A collisions. In the first one initial conditions are computed via classical Yang-Mills(YM) or pQCD equations. In the second approach initial conditions are constructed by extrapolating final observable backwards via suitable dynamical scenario. The second approach is traditionally based on solution of hydrodynamic equations. In this section we consider the first one, and in Section 1.5, the second one.

Immediately after heavy ion collision at RHIC and higher energies the nuclei acquire stochastic color charge because of multiple soft gluon exchange. These color charges produce multitude of color flux tubes occupying space between receding slabs. Apparently initial string tension depends on the beam energy. In principle as it will be shown later, the string tension can be related to the color charge by Gauss law. Color charges fluctuate from event to event around zero average value. For asymptotically large number of events these fluctuations are described by Gaussian distribution. In this range of energies a new state of very dense partonic plasma is expected to form. This new state can be described by the classical Yang-Mills theory, which is known as the Color Glass Condensate(CGC) model [28]. This model provides a general method to compute initial conditions. What are the general properties of this initial state? One of remarkable features of rapidity distribution of produced hadrons is so-called limiting fragmentation. If we plot rapidity distribution of produced hadrons at different energies as a function of $y - y_{proj}$, the rapidity distributions in vicinity of y_{proj} are to a good approximation independent of beam energy. This means that as we go to higher and higher energies the degrees of freedom at large x are held fixed. The new physics is associated with additional degrees of freedom at smaller rapidities in c.m. frame ($x \leq 10^{-2}$). Partons at small x are in the high-density semi-classical regime. At the same time, degrees of freedom at $x \sim 1$ do not change much. This suggests that one can apply some kind of a RG description of rapidity distributions that is done in the CGC model.

Formally the CGC model is introduced via following generating functional:

$$Z = \int_{X_0} [dA][dj] exp(iS[A, j] - \chi[j]), \qquad (1.1)$$

which corresponds to an effective theory defined below some cutoff in x at X_0,

which separates fast and slow degrees of freedom. Fast degrees of freedom serve as sources of slow degrees of freedom. Arbitrariness in choice of X_0 is cured by the RG equation which requires that physics should be independent on it. This effective theory describes gluon field in the presence of an external source j. This source arises from quarks and gluons with $x \geq X_0$, and is a variable of integration. The fluctuations in j are controlled by the weight function $\chi[j]$. This weight function satisfies the JIMWLK equations which make the theory independent on X_0. If the parton densities are not so high, this RG equation can be linearized and have been shown to agree identically with the leading log BFKL [25] and small x DGLAP equations [26]. Very high parton densities correspond to CGC saturation regime. In this regime density of gluons is large and interaction of probability is close to 1. The border between dense and dilute regions is defined by saturation criterion:

$$\sigma\rho \sim 1, \tag{1.2}$$

where ρ is the density of partons in the transverse plane, and σ is the cross section of interaction of hard probe with partons

$$\sigma \approx \alpha_s(Q^2)\frac{\pi}{Q^2} \tag{1.3}$$

Generic momenta corresponding to this regime are less than the saturation scale,

$$Q^2 \leq Q_s^2(x) \tag{1.4}$$

Dependence on x appropriate for given energy range can be evaluated as

$$Q_s^2 = Q_0^2(x_0/x)^\lambda GeV^2 \tag{1.5}$$

This formula approximates with about 15% uncertainty $\lambda = 0.3$ HERA data at $x_0 \sim 10^{-4}$ [29].

As was shown in Ref.[27] saturation criterion can be reformulated in terms of classical Yang-Mills fields as well. Namely, in saturation regime non-linear terms in the field stress tensor become important: $\partial_\mu A_\nu \sim g_s A_\mu A_\nu$. In momentum space, this condition corresponds to $g_s A_\mu \sim Q_s$. Therefore chromofield energy density in saturation regime is

$$\epsilon_f = \frac{\mathbf{E}^2}{2} = \frac{Q_s^4}{g_s^2} \tag{1.6}$$

Limit case corresponding to very small x and very large nuclei can be described by McLerran-Venugopalan (MV) model. For this model perturbative treatment is valid, since strong coupling constant calculated on the

characteristic scale Q_s is small $\alpha_s(Q_s) \ll 1$. This means that the quantum states of the system associated with the condensate are multiply occupied: $n_k \sim \frac{1}{\alpha_s}$. These states are highly coherent, and share some properties of Bose condensate. The gluon occupation number is very high, but it is logarithmically increasing with increasing the energy, or decreasing the transverse momentum. This provides saturation and cures the next to leading order problem of BFKL approach which leads to very large corrections. Therefore, the Froissart limit appears naturally in this model.

The basic ingredients of the MV model are hard probes distributed stochastically in transverse plane and corresponding to them classical YM equation. These hard probes or external currents are assumed moving along the light cone or recoilless. Hard probe cross section has such extent that mean color charge squared inside it is large but average color charge is zero. It can be estimated from condition (1.2), and in further calculations we take it as $s_\perp = \frac{\pi}{Q_s^2}$. In this picture all partons with large rapidities can be considered as sources for classical color fields or gluons with lower rapidities. This follows from the fact that classical and quantum calculations for tree-level radiative process corresponding to emission of soft gluons by fast partons give the same results. It can be also shown that further quantum corrections do not invalidate this description, but simply renormalize the properties of classical source, in particular, its correlations. For example if we want to compute the gluon distribution in the small region $\Delta y \sim 1$ around $y = 0$, then the source of these gluons is dominated by hard partons with rapidities much larger than 1. Since this can be done at any reference frame, the classical gluon field may be thought of as arising from rapidity dependent classical source. At ultra-high energies the coordinate space rapidity is of the same order as the momentum space rapidity. It is used coordinate space rapidity because classical equation of motion is formulated in terms of coordinate space variables. In the case of collision of projectile p and target t nuclei it takes the following form:

$$D_\mu F^{\mu\nu} = g_s^2(\delta^{\nu+}\rho_p(x^-, \mathbf{b}, \mathbf{s}) + \delta^{\nu-}\rho_t(x^+, \mathbf{b}, \mathbf{s})), \qquad (1.7)$$

where ρ_p, ρ_t are recoilless sources of the classical Yang-Mills field. The space-time rapidity η is related to the light-cone variable, $x^\pm = \frac{t \pm z}{\sqrt{2}}$ as $\eta = \frac{1}{2}\ln(x^+/x^-)$.

In the MV model averaging on ensemble of color charges in transverse plane is carried out with the Gaussian weight:

$$P[\rho_p, \rho_t] = N \exp\left[-\int d\eta d^2s \left(\frac{1}{2\mu_p^2(\eta, \mathbf{b}, \mathbf{s})}Tr\rho_p^2(\eta, \mathbf{b}, \mathbf{s}) + \frac{1}{2\mu_t^2(\eta, \mathbf{b}, \mathbf{s})}Tr\rho_t^2(\eta, \mathbf{b}, \mathbf{s})\right)\right]$$
$$(1.8)$$

Rapidity density of color charge per unit area is usually normalized as

$$\langle\rho_A^a(\eta,\mathbf{b},\mathbf{s})\rho_A^b(\eta',\mathbf{b},\mathbf{s}')\rangle = \mu_A^2(\eta',\mathbf{b},\mathbf{s}')\delta^{ab}\delta(\eta-\eta')\delta^{(2)}(\mathbf{s}-\mathbf{s}') \tag{1.9}$$

where a,b are reserved for color indecies, and index $A = p,t$ specifies the nucleus. Rapidity density of average color charge squared per unit area and per color μ_A^2, as shown in Ref.[30], in the general case has contributions from valence quarks and hard gluons color charges both:

$$\mu_A^2(\mathbf{b},\mathbf{s},Q^2,y) = N_A(\mathbf{b},\mathbf{s})\left(\frac{1}{2N_c}xq(x,Q^2) + \frac{N_c}{N_c^2-1}xg(x,Q^2)\right) \tag{1.10}$$

where $q_A(x,Q^2)$ and $g_A(x,Q^2)$ are valence quark and gluon distribution functions. As was shown in Ref.[31] saturation momentum squared for nucleus $A = p,t$ can be found by iterative solution of the following equation:

$$Q_s^2 = \frac{8\pi^2 N_c}{N_c^2-1}\alpha_s(Q_s^2)N_A(\mathbf{b},\mathbf{s})xg(x,Q_s^2) \tag{1.11}$$

where α_s is the fine-structure constant calculated at some virtuality Q^2.

$$\alpha_s(Q^2) = \frac{4\pi}{(11-\frac{2}{N_c}N_f)ln\frac{Q^2}{\Lambda_{QCD}^2}} \tag{1.12}$$

Iterations are started from parton distribution functions defined at initialization scale Q_0^2. This scale should be taken large enough to provide convergence of the DGLAP evolution to higher virtualities.

Since valence quark and gluon distribution functions are normalized as following:

$$\int_{x_0}^1 dxq(x,Q^2) = N_c, \qquad \int_{x_0}^1 dxg(x,Q^2) = N_c^2 - 1 \tag{1.13}$$

integration on pseudorapidity reproduces results of Ref.[32] obtained for charging of nucleus by random walk of classical color charge in SU(3) space:

$$\mu_A^2(\mathbf{b},\mathbf{s}) = g_s^2 N_A(\mathbf{b},\mathbf{s})\left(N_c + \frac{1}{2}\right) \tag{1.14}$$

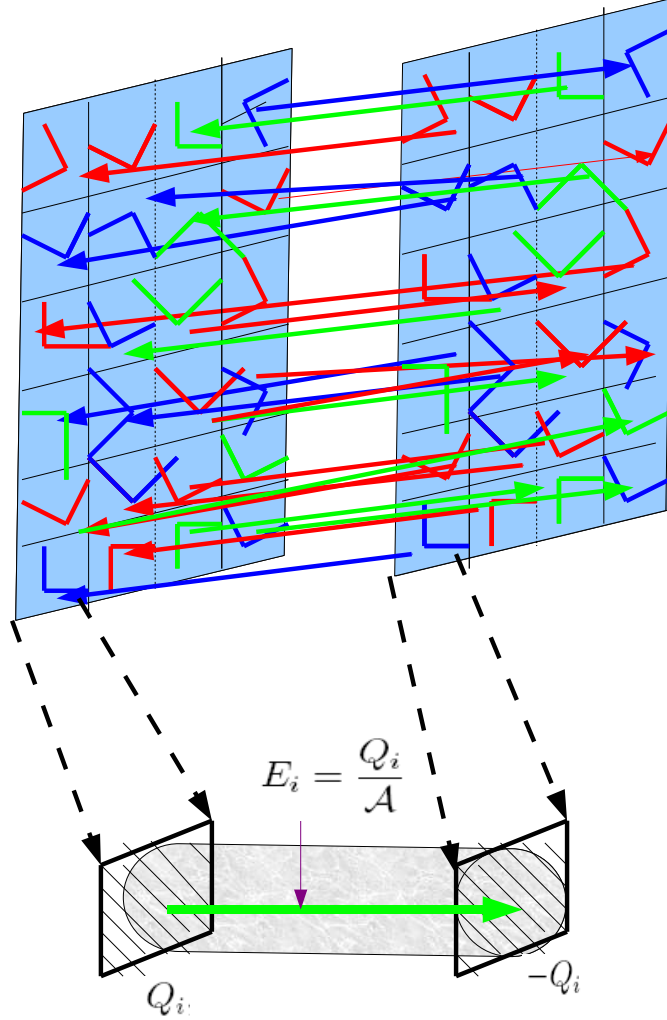Fig.1.3 shows the generic configurations of CGC fields after collision.

Figure 1.3: Longitudinal and transverse components of MV chromofield produced by stochastic color charges generated on nuclear sheets after collision, as proposed in Ref. [2]. Directions of the field can be opposite, but total force between the slabs is attractive. Each slab area is subdivided on smaller elements or spots of minimal area $s_\perp = \pi a^2 = \frac{\pi}{Q_s^2}$, which can be resolved by hard probe of given energy. Classical field produced between two spots with opposite charges Q_i has a color flux tube configuration displayed on the bottom figure.

1.4 Microscopic models

Effective QCD motivated models for hadron-hadron and heavy ion collisions at different energies are constructed to mimic some characteristic features of the QCD such as asymptotic freedom and confinement. It should be noted that while asymptotic freedom of QCD was proved by the RG analysis, the analytical proof of confinement for QCD is still an open issue. At present it is treated only phenomenologically, as for instance in Friedberg-Lee model [33] or in a simple string model, where it is assumed that the string can be broken by a pair creation. The deconfinement transition is predicted at high T, large μ or in strong external field (at ultra-high energies this external field can be modeled as the Color Glass Condensate (CGC)[2, 35]). The basic idea of Friedberg-Lee model is to model confinement by the color-dielectric function $0 < \kappa(\sigma) < 1$. QCD vacuum in this model is introduced by assuming that it can be treated as a color dielectric medium. Outside the medium we have usual nonperturbative QCD vacuum: $\kappa(\sigma) = 0$. The dynamics of color flux tube formation in this model is studied by Lagrangian:

$$\mathcal{L}_{FL} = \sum_i \bar{q}_i \left(i\gamma_\mu \left(\partial_\mu + ig_s \sum_a A_\mu^a T_a \right) - g_0\sigma - m_i \right) q_i - \frac{1}{4}\kappa(\sigma) \sum_a F_{\mu\nu}^a F^{\mu\nu a} + \mathcal{L}_\sigma \tag{1.15}$$

The field tensor is given by

$$F_{\mu\nu}^a = \partial_\mu A_\nu^a - \partial_\nu A_\mu^a + g_s f_{abc} A_\mu^b A_\nu^c. \tag{1.16}$$

To study static properties it is usually considered only gluon sector of the theory in the Abelian approximation. Then non-Abelian interactions are merged in the confinement field σ and its dielectric coupling $\kappa(\sigma)$. The confinement field is evolving in the presence of a scalar self interaction $U(\sigma)$

$$\mathcal{L}_\sigma = \frac{1}{2}\partial_\mu\sigma\partial^\mu\sigma - U(\sigma), \qquad U(\sigma) = \frac{a}{2!}\sigma^2 + \frac{b}{3!}\sigma^3 + \frac{c}{4!}\sigma^4 + B. \tag{1.17}$$

However, as shown in Ref. [34] non-Abelian self-interaction is important to confine dynamical gluons. Placing the color charge in QCD vacuum produce the dielectric cavity around it. In the static case chromoelectric displacement induced by color charge is calculated by the Gauss theorem

$$\vec{D}^a = \frac{g_s q^a}{4\pi r^2}\vec{e}_r \tag{1.18}$$

Since outside this cavity the energy of color charge $\int d^3r \frac{D_a^2}{2\kappa(\sigma)}$ is divergent, color charge is effectively locked. In this model quarks behave like quasi-free

particles inside the soliton, but they are confined at larger distances. Results of this model approach the MIT bag model limit, which has the advantage that it can be solved analytically in its static variant. Dynamical MIT model is a very complicated problem in Quantum Field Theory, which has been solved only in 1+1 dimensional case [36]. Soliton field describing dielectric medium in the CDM model is effectively reduced to the MIT bag constant, which amounts to the volume energy to produce bubble of perturbative QCD vacuum.

Other popular class of models is dealing with binary parton potentials. The potential is usually divided into short range and long range parts. Short-range part corresponds to processes with high virtualities. It is described by Coloumb-like potential. Long-range part corresponds to one or multiple soft gluon exchange processes, and it is described by linear potential. Due to gluon self-interaction chromofield is assumed to be confined in the tube with a constant energy per unit length. When two hadrons collide color flux tube is formed due to single soft gluon exchange. In the simplest case of excited hadrons, the chromofield appears as a single string, and corresponding string tension can be extracted from the slope of Regge trajectory, which relates hadron mass and its spin. In the case of multiple soft gluon exchange a color flux tube may appear and corresponding chromofield energy density can be calculated by Gauss law [5].

If energy accumulated in the color electric field is high enough, it can create parton pairs. Strings can percolate to form a color flux tube whose color field is determined by color charges on the one of flux tube cap. Since these charges are bigger than in a single string this will lead to enhanced heavy flavor and baryon-antibaryon production due to increased string tension. The possibility of string fusion was studied within the Quark Gluon String Model (QGSM) [37]. Output of this model can be used as initial conditions for further rescattering dynamics. Initial longitudinal and transverse momentum fractions of newly created complexes of strings and hard gluons are governed by Pomeron theory [38]. String fragmentation proceeds in an iterative way: String fragments are taken as new strings which are broken again, until enough energy for further division. String decay probability is given by Schwinger formula, and for longitudinal string break up, an invariant area law is employed [46] (see e.g. (1.21)).

In the flux tube model in addition to the possibility of baryon production via the diquark-antidiquark creation, there exist a possibility to produce baryons via successive creation of $q\bar{q}$ pairs by 'popcorn' mechanism [39]. In high energy collisions the majority of primary particles are soft partons and jets are in minority. If energy of jets is high enough they initiate further cascade development in course of propagation inside continuously formed

medium of soft partons. This medium of soft particles at ultra-high energies can be modeled as Color Glass Condensate (CGC) [40]. Proper treatment of the CGC leads to a cut-off in parton momentum distribution at saturation momentum $p_t \sim Q_s \gg \Lambda_{QCD}$. As shown in [40], the parton interaction with the CGC environment in small x regime is characterized by QCD coupling constant evaluated at Q_s. In the process of propagation jets lose some part of their energy due to interaction with this medium. This phenomenon is called "jet quenching". The mechanism of jet quenching is different in QGP and hadron gas. In the case of hadron gas partons are decelerated according to the string tension. In partonic medium the jet loses energy due to collisions with color charges. Taking into account Debay screening leads to IR finite results for energy loss without introducing a cutoff. Multiple parton production neutralizes external field gradually. This process was investigated in Ref.[5] in a kinetic approach including the interaction of partons with chromofield. There neutralization of Abelian chromofields occupying infinitely long cylinder had been studied by solving the kinetic equation. Interaction of hard modes was treated by Boltzmann-like collision term, and soft modes by Debye screened potential. Moreover at early times treatment of parton production in a constant classical background field is well justified in the CGC parton cascade picture since fast degrees of freedom can be considered as effectively frozen over the life-time of the soft gluons [28].

Understanding of experimental data from the first principles is rather difficult for heavy ion collisions, but at the same time QCD-based calculations are quite successful for the description of l^+l^- and lN collisions at high energies [41]. The main components of such calculations are parton distributions and fragmentation functions. These functions are universal and once extracted from experiment they can be used to describe hadron production in the other hard QCD processes. A fragmentation function $D(z)$ allows to know how much of the energy-momentum carried by the initial quarks and gluons ends up in each of the produced hadrons. It is defined as probability to produce a hadron of some type anywhere in the jet with energy-momentum fraction:

$$z = \frac{(E + p_{||})_{hadron}}{(E + p_{||})_{parton}} \tag{1.19}$$

from an initial parton. It should be kept in mind that complicated picture of quark-gluon shower development is absorbed in the fragmentation function. The primary hadron multiplicity in a jet produced in l^+l^- annihilation event is calculated as:

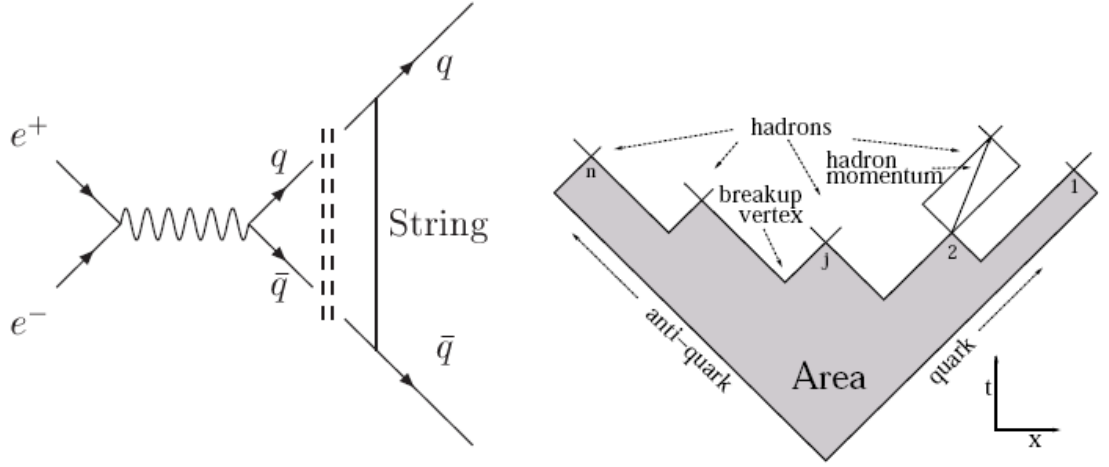$$n = \int\limits_{z_{min}}^{1} D(z)dz \tag{1.20}$$

Figure 1.4: The figure shows a typical Lund String break-up. The left panel shows a e^+e^- annihilation into $q\bar{q}$ pair. Receding q and $\bar{q}$ are connected by a string. The right panel shows the hadron formation after string break up. Each hadron is understood as quark-antiquark pair moving along yo-yo trajectory. Probability to produce a set of hadrons is dependent on area spanned by primary quarks corresponding to some proper time.

where z_{min} is a minimum z which is kinematically allowed. For instance in two jet event $z_{min} = 2M_h/\sqrt{s}$.

There exist several competing Monte-Carlo event generators to simulate shower development and fragmentation process in l^+l^- annihilation. The simplest one is based on independent jets model leading to so-called Feynman-Field fragmentation function [42]. Most advanced are either based on pQCD branching processes as in Marchesini-Weber model, [43], or, as its rival Lund parton shower on string fragmentation model [44, 45].

In the Lund model, firstly, after a virtual photon emission in l^+l^- collision, a high energy $q\bar{q}$ pair is produced. Quark and antiquark move apart along the light cone in opposite directions connected by a relativistic string with constant energy per unit length. New $q\bar{q}$ pairs can be created in the color field and accelerated by the field in opposite directions. The probability of string breaking in a length δx and time δt is a universal constant γ times the space-time volume, $\gamma \delta x \delta t$: Breaking the string destroys the color flux in the future light cone of the vertex. This leads to so-called Area Law, which states that the non-normalized probability to produce a set of hadrons with

momenta $p_1, p_2, \ldots, p_n$ and total momentum P_{tot} is given by:

$$dP_n(\{p_j\}; P_{tot}) = \prod_{j=1}^{n} N_j d^2 p_j \delta(p_j^2 - m_j^2) \delta\left(\sum_{j=1}^{n} p_j - P_{tot}\right) exp(-\gamma A), \quad (1.21)$$

where A is the area spanned by the string state before it decays, Fig.1.4. Recent developmet of Lund model includes gluon production also [46].

As more $q\bar{q}$ pairs are produced, small pieces of string with quark from one vertex, and antiquark from another one form a bound states via the attractive color force (a 'yo-yo' type of binding). The process of pair creation can be considered as tunnelling through the energetic gap of width $2m_\perp = 2\sqrt{m^2 + p_\perp^2}$ between the negative-energy states in Dirac sea and the positive-energy states (produced pairs are characterized by their quantum numbers (p, σ), where σ runs over spin and color indecies). This gap is schematically illustrated in Fig.1.5 for the case of a linear static potential. It can be shown that in the case of external field occupying infinite volume the famous Schwinger's result can be reproduced [47]. In the time-dependent case, the evolution mixes states with positive and negative energies, resulting in non-diagonal terms of Hamiltonian which are responsible for pair production. The diagonalization of the Hamiltonian in the homogeneous chromofields can be achieved by a time-dependent Bogoliubov transformation. Applying this transformation to the initial oscillator type differential equation with time dependent frequency reduces the latter to the system of two Heisenberg-like equations of motion [48].

Strings which are formed between receding partons can break-up only if they are long enough to have sufficient energy to form a hadron. Thus, the finite size effects are important for chromofield decay probability. They were taken into account only for linear static vector potential with field volume restricted by a finite cylinder, [49] and linear time dependent vector potential with field volume restricted by an infinite cylinder, [50]. Schwinger formula is reproduced in infinite volume limit for both cases. In accordance with QCD, chromofield can decay either on $q\bar{q},gg$ or ggg in the different color, flavor and spin states. Due to interaction between each other produced partons can form new strings. These strings again decay and so on, and so on, until the partons form bound states via recombination. It is believed that mesons, baryons, and their excited state are formed in this way.

The simplest way to study finite size effects is based on the static MIT bag model [51]. One can consider a Color Flux Tube of a cylindrical shape. The finite size effects in transverse direction can be taken into account by applying so called MIT boundary conditions on the tube surface [5], and in longitudinal direction by applying the continuity condition for the wave
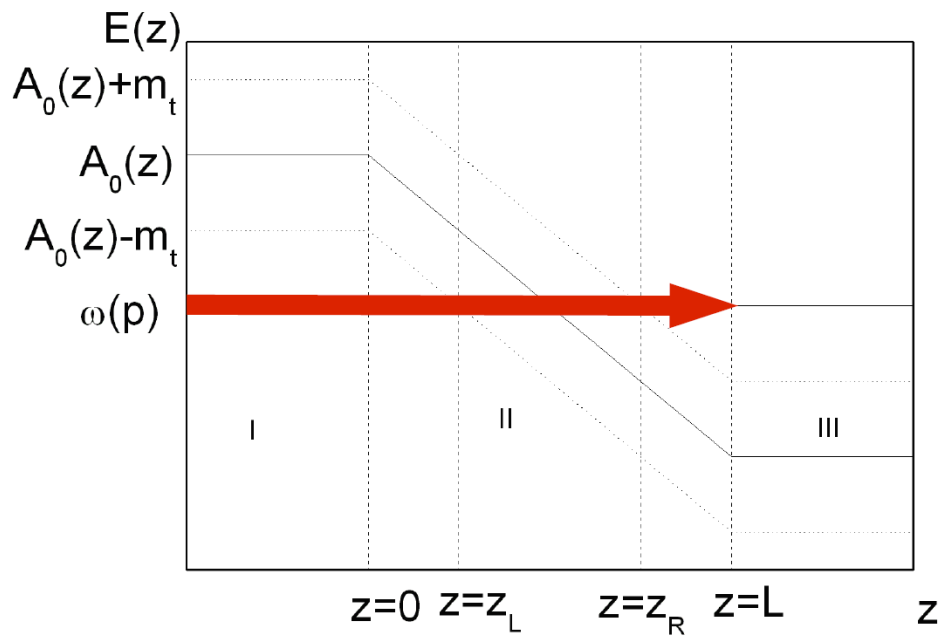
Figure 1.5: Energy gap between positive and negative continuum in the presence of an external field (linear string-like potential) as a function of longitudinal coordinate, where L is the string length, and $z_L = \frac{-E-m_\perp}{\sigma}$, $z_R = \frac{-E+m_\perp}{\sigma}$ are the left and right bounds of energy gap corresponding to the energy of incident wave $E = \omega(p)$.

function in different regions of external potential. The alternative way to study these effects is based on expansion of corresponding Green functions in powers of inverse volume occupied by the field, [52].

In reality physical situation is highly dynamical, since receding partons stretch the string. Hence boundary conditions on the edge of expanding flux tube are also dynamical. In two-dimensional case the problem with non-stationary boundary conditions is always reduced to a static case by means of conformal transformations, provided that the vacuum expectation value of the energy-momentum tensor can be neglected [53].

Parton cascade models [54, 55, 56] use different philosophy to generate the final state hadrons. Parton interactions are described within the leading-log approximation of perturbative QCD (pQCD). The cross section of producing a primary hadron of some type in e^+e^- annihilation is factorized on the basis of the QCD factorization theorem [57] on the perturbative ($e^+e^- \rightarrow q\bar{q}$) and non-perturbative parts (fragmentation function). This theorem is formulated for an inclusive reaction, like ep deep inelastic scattering. There are two mass scales in the problem. One is renormalization scale, and the other one is the factorization scale. If virtuality Q^2 is greater than the factorization scale one has coefficient functions, while opposite case corresponds to the parton distribution function. It can be proved that the structure functions can be factorized into short-distance part calculable in pQCD and a long-distance (nonperturbative) part which is parameterized according to experimental data. Short-distance evolution of parton distributions, given at some initial scale Q_0^2 towards higher virtualities Q^2 is governed by so-called DGLAP equations [26]. The initial partons are mostly gluons, which split into $q\bar{q}$ pairs and then recombine into primary hadrons or color singlet clusters. These clusters decay via many-body phase space into final hadrons.

In nuclei the situation is complicated by shadowing ($x < 0.01$), and anti-shadowing ($0.1 < x < 0.4$) effects, as well as by saturation phenomenon [35]. Parameterization of nuclear quark distribution functions was obtained by combined χ^2 analysis of the data at given virtuality with further DGLAP evolution [58]. But for gluon distribution function the fit is still unreliable. The investigation in Ref. [59] has revealed that the NNLO DGLAP analysis is convergent only at $Q_0^2 > 5 GeV^2$, but convergence deteriorates with decreasing x. Therefore other approaches are needed to probe the whole kinematical region. One of them is BFKL equation which resumes leading logarithms of $\alpha_s log(1/x)$ in QCD [25]. It allows to describe evolution on $1/x$ at some fixed Q^2. The BFKL kinematic region overlaps with saturation region at small x corresponding to high parton density produced in heavy ion collisions. As it will be discussed later, only in the small x region and for very large nuclei the parton distributions can be calculated in MV model

within perturbative theory [32].

Copious production of minijets which are unresolved pQCD jets with $p_t > p_0$ makes it possible to employ the pQCD formalism. Determination of the scale p_0 separating soft and hard interactions is ambiguous. To simulate the minijet production a Monte-Carlo model HIJING (Heavy Ion Jet Interaction Generator) is often used. It can be classified as dilute parton-gas model. Such models are based on the extrapolation of pQCD from high p_t down to a scale of p_0. It has the following characteristics: a)Soft beam jets are modeled by diquark-quark strings within the Lund phenomenology. Multiple low p_T exchange among end point constituents are included in the initial state interactions; b)Initial and final state radiation; c)An impact parameter-dependent structure function is introduced to study the influence of shadowing on observables; d)jet quenching.

The early stages of a nuclear collision, up to times $\sim \frac{1}{Q_s}$, can be described as the melting [60] (or explosion?) of the CGC by formation of minijets and soft gluons. The gluons resulting from the decay of the classical saturated field are uncorrelated at $k_\perp \lesssim Q_s$. In turn partons with larger transverse momenta have strong back-to-back correlations. This is in accordance with well known results of pQCD calculations.

The forthcoming thermalization process can be studied by solving relativistic quantum field equations, but such kind of calculations in QCD is intractable at present. Instead of that some simplified QFT models simulating some generic features of strong interactions are usually used. Numerical simulations of thermalization process are carried out in various domains of physics from Heavy Ion Collisions to Cosmology. For instance, in Cosmology they were applied to study post-inflationary preheating stage in the evolution of the Early Universe [61]. The decomposition of field into the classical background field and quantum fluctuations [62], with further Bogoliubov's transformation of obtained dynamical equations into kinetic equations, was applied in Ref. [63, 64] to study back reaction mechanism and thermalization process in some simple scalar QFT models. Due to interaction with mean field quasiparticles gain a time dependent mass. As shown in Ref.[63] the calculated spectra of quasiparticles are rather close to thermal. In Ref.[64] a more advanced QFT model was proposed to simulate QGP. Gluon self-interaction was modeled by a scalar term φ^4. Collision integral was taken in Landau approximation, i.e. assuming small momentum transfer in elastic qq,qg and gg collisions. But it turned out that this model can hardly provide thermal equilibration. In contrast to abundances calculated in pQCD gluons are not dominant at the very early stage of interaction for this model. This can be explained by spin effects in source term suppressing low $P_{||}$ gluons.

Most popular microscopic models to study thermalization process are based on the relativistic transport theory. The fundamental assumption underlying transport models is that the state of the partonic system can be characterized by a set of one-body distribution functions. The starting point for deriving corresponding kinetic equations is Liouville equation. In particular BBGKY hierarchy [65, 83] was derived in this way. It has two physically important limits. In one of them, when mean free path is much smaller than the size of the system, it leads to hydrodynamics, and in another one, when mean free path is of order of system size, it transforms to Boltzmann equation. Derivation of quantum kinetic equation starts from evolution equation for density matrix. Fourier transform of the density matrix is known as the Wigner function which in semiclassical limit can be interpreted as a one-body distribution function. It's evolution in phase space is obtained by Wigner transform of the von Neymann equation. The main advantage of this method is that functions sharply peaked with respect to relative coordinate variable translate into smooth functions with respect to coordinate and momenta. Smoothness of Wigner function can be enforced even more by averaging it over a phase space volume larger than $\hbar^3$, what is called coarse-graining. Of course, by doing so one is losing information about quantum correlations. Coarse-grained volume is chosen in accordance with relaxation time generic to the problem of interest. Smoothening over the phase space volume which is characteristic for given problem is essential to make equations solvable. In the simplest case of binary collisions this equation is reduced to the standard Boltzmann equation, which can be solved by subdivision technique [66]. The collision integral is usually taken in the most simple form, where transport cross sections are calculated by pQCD or taken from experiment. Physical region between this two limiting cases corresponds to the dense quantum gases, and it is very difficult for numerical analysis. But as shown in Refs.[56, 67] corrections to the Boltzmann equation corresponding to $2 \rightarrow n > 2$ processes, in particular $gg \rightarrow ggg$, are important for studying thermalization in QGP at RHIC energies. Unfortunately, there is no practical algorithm at the moment to solve kinetic equations with collision term of higher order. Therefore, if hydrodynamics applies to A+A at RHIC, then some other nonperturbative mechanisms leading to thermalization should be considered. Recently such a mechanism was proposed in Ref. [68]. The idea is to study time evolution of classical fields in CGC cascade picture. It was pointed out two important effects for the classical field evolution in the CGC cascade. It is increasing the field frequency due to the interactions between produced partons, and screening the original color field by produced color charges. By consideration based on the background field method [62] and relation between the gluon distribution function and

imaginary part of the gluon propagator in the strong classical field [69] the
first effect leads to increasing the temperature of gluon spectra

$$T = \frac{\omega}{4\pi} \tag{1.22}$$

and the second one to fall-off of the field amplitude. In the same work the
both effects were incorporated in the simple model of chromofield decay:

$$A_+(x_-) = \frac{E_0}{\omega}\left(1 - \exp(-\omega x_-)\right) \tag{1.23}$$

As one can see, the early time evolution of the classical field is static, which
corresponds to the initial stage of the CGC cascade development: parton
production can be thought as a process of emission by a frozen system of
fast partons. It should be pointed out inconsistency of the model based on
potential (1.23), since it does not take into account oscillations of classical
field. Therefore it is quite crude approximation of potential, which should
describe damping oscillations with increasing frequency. In the low color
charge density approximation analytical solution of Yang-Mills equation has
a form (2.31), which should lead to the more adequate model.

Moreover, application of pQCD for near-equilibrium evolution is question-
able. For instance, linear response analysis based on pQCD predicts highly
viscous state of produced matter [70] while experimental data indicate on
practically ideal fluid behavior. In Ref.[71] it was argued that the QGP must
expand as nearly perfect fluid due to large jump of entropy density at the
deconfinement transition. On the other hand, alternative calculations within
the AdS_5/CFT correspondence predict a very low viscosity for strongly cou-
pled plasma. Only forthcoming LHC program can clarify these questions.

There exist other models to describe approach to kinetic equilibrium
and/or momentum isotropzation. Most of them are based on solving the
Boltzmann equations with different corrections and modifications. The PCM
[54] is one of them. Initial conditions are given by appropriate parameteri-
zation of parton distributions sampled at initialization scale Q_0^2. Partons are
assumed on their mass shell, except before the first collision. In this model
non-perturbative, collective field effects on parton dynamics are neglected.
The weak point of the PCM is dependence of results on low momentum cut-
off p_t^{min}, which is needed to regularize the infrared divergent perturbative
parton-parton cross section. Under certain assumptions, the low momentum
cut-off $p_t^{min} \sim Q_0$ can be extracted from the experimental data for elementary
hadron-hadron collisions [72]. In addition, one has to take into account the
LPM effect [73], namely that, in a dense medium the radiation of soft gluons
is suppressed. In the improved so-called self-screened parton cascade model

this problem has been solved by introducing a medium which screens the long range color fields associated with soft modes [74]. Natural and consistent treatment of plasma screening effects is based on the thermal field theory [75]. The medium is produced in early parton-parton collisions. When two nuclei collide at sufficiently high energy, the screening occurs on the length scale where pQCD is still applicable. This approach yields predictions for the initial conditions for the QGP formation without any need for momentum and virtuality cut off parameters.

Another popular model is the so-called uRQMD model [7], which can be classified as a string based hadron cascade model. In string models non-interacting strings are formed and then decay into hadrons which later on perform rescatterings. The description of particles in the uRQMD takes into account their quantum nature by representing them by Gaussian wave pockets. Hadrons interact either by elastic or inelastic scatterings, or, at higher energies, by the formation and decay of strings. Moreover, inelastic scatterings can produce hadronic resonances, which will subsequently decay. These interactions are implemented by using known vacuum masses and cross sections or, where data are not available, extrapolations from known vacuum cross sections and estimates based on additive quark model. The conversion of the excited string into hadrons is obtained according to the Field-Feynman string fragmentation function [42]. The excitation and fragmentation of strings dominates the production of new particles in the uRQMD. At any time step of simulations the uRQMD code propagates only particles not strings. Therefore, all hadrons which are to be formed by the string fragmentation are determined from the very instant of the string formation, and propagated for a certain amount of time without interaction with the remainder of the hadronic system. Transparency of the nuclei is strongly dependent on this so-called formation time.

Due to the small transverse pressure at early times the uRQMD predicts a decrease of elliptic flow from SPS to RHIC, but 50% increase was observed instead [76]. In contrast to these microscopic models, hydrodynamic calculations at the SPS and RHIC, give a good description of the observed radial and elliptic flows, but offer no insight into the microscopic mechanism of equilibration.

In analogy with Coloumb plasma, where different instabilities play crucial role, one can expect them also in the QGP and in the hadron medium, when mean fields are taken into account in the kinetic approach. Let us consider so-called two-flux instability [77]. At the initial stage the mean field is small, and hard dynamics which is described by collision integral is dominating. Hard collisions between plasma constituents can be described in a semiclassical approximation by Lennard-Balesku collision integral for

color particles. Stability analysis reveals fast growing mode corresponding to Weibel or filamentational instability, [77, 78]. This instability can be experimentally measured from essentially nonequilibrium stage of reaction, and can be interpreted as a signal of QGP formation. It can be detected by intensive γ-radiation (bremsstrahlung) in the perpendicular plane to the beam axis. At the late stages mean fields are strongly nonlinear and may pose a turbulent behavior. This can be possibly detected only at LHC energies when the QGP is expected to live long enough. This effect was studied in [79], where significant grows of chromofield transverse mode was demonstrated. Moreover anomalously low viscosity generation is expected [80].

The evolution of thermalized and dense partonic matter(QGP) have been studied in various microscopic and macroscopic approaches. In particular, thermal properties of QGP on microscopic level have been studied within the qMD model with initial conditions provided by the uRQMD. Time evolution of the system of quarks interacting via linear potential is described by Newton equations which are solved by Runge-Kutta method. The knowledge of particle trajectories in phase space is used to calculate the Hamiltonian and corresponding statistical weights on each time step. After that the Metropolis algorithm is applied to find the most probable equilibrium configuration. In some test cases shaking of all coordinates and momenta is applied instead of step by step solving equations of motion. Temperature is either given by hand or extracted from inverse slope of the momentum spectra. The net-baryon density is introduced by specifying the numbers of quarks and antiquarks. Quark color is treated in Abelian approximation which assumes it as a fixed quantum number. No gluons are included explicitly in the model. This is serious obstacle to apply the qMD for RHIC and higher energies. But if gluons would be included in dynamical description of produced system the other problem arises, namely, how to cope with hard gluons at hadronization. Further possible extension of this model is to treat color as dynamical variable evolving in time by classical Wong equations. A more realistic treatment should deal with parton Wigner functions in induced self-consistent field. Kinetic equations for partonic Wigner functions were derived in Ref. [81]. Due to the high complexity only linearized version of these equations was considered up to now. In particular, it was used to study possible instabilities in the system [77]. The other shortcoming of the qMD model is that quarks are treated as classical particles, and as a consequence it cannot yield realistic hadron spectrum. However it can be used as a first step to obtain a fully dynamical description of deconfined quarks and their hadronization through formation of color-neutral clusters via the implemented recombination mechanism. Using current masses in qMD does not mean that the color neutral clusters have low mass, but opposite, they can be quite heavy, gaining large

part of their mass from the large potential energy. In contrast to the qMD, in the coalescence model quarks carry large constituent masses, and recombination criteria requires proximity in momentum space, i.e. quarks with small relative three-momenta. One of possible ways to incorporate quantum mechanics in the qMD model is to treat the problem of color neutral cluster decay in the MIT bag model. Each produced cluster occupy finite volume in space-time. This volume is constrained by energy-momentum and potential energy stored in the bag. The latter is usually parameterized by bag constant and set of coupling constants. This constants are fitted to the hadron ground state properties. Due to boundary conditions, the spectrum of quantum states of the bag is discrete. Each energy level has definite width reflecting probability to decay into some lower states. Each excitation is identified with an appropriate hadron state of given mass and quantum numbers. At SPS energies most of produced particles are delivered by resonance decays but not by Schwinger mechanism because produced chromofields are not strong enough. At higher beam energies particle production by chromofield decay becomes more important. It can be taken into account either by increasing string tension or by using a more advanced Friedberg-Lee model. Up to now this model has been implemented to compute fields corresponding to static configurations of color charges. Consideration of network of dynamic color charges linked by Friedberg-Lee strings reflects the physical situation more realistically. But in this case computational effort will be much more expensive.

1.5 Hydrodynamical approach

On the macroscopic level the time evolution of a thermalized system is governed by the hydrodynamical equations which express explicitly local conservation of energy and momentum. The applicability of hydrodynamic models to describe ultra-relativistic heavy ion collisions (SPS and higher energies) follows from the observation that the local thermal equilibrium is established very fast. For instance, the Parton Cascade Model(PCM) simulations for RHIC energies indicate that the momentum distributions of quarks and gluons become isotropic almost at the same time of about $1 - 2fm$ which is the time scale when the energy spectrum gets exponential [56]. On the other hand, simulations within QGSM gave the same time for achieving isentropic regime even at lower energies of SPS for Pb+Pb collisions [82]. This shows rather large uncertainties of these models. But of course advantage should be given to the more refined PCM model, since rescattering mechanism in QGSM is too naive.

Weakly non-equilibrium systems can also be studied within hydrodynamics, but in this case entropy is not conserved. Dissipative forces and corresponding to them transport coefficients were calculated in the linear responce theory [83]. Obviously if there is an influx of particles due to pair creation by external field then entropy current is also not conserved. Besides assumption of local thermal equilibrium, under certain conditions one can also assume local chemical equilibrium. One of the great advantages of hydrodynamic model is its ability to investigate the relation between the equation of state (EoS) and physical observables via comparison of calculations with experimental data. It is especially useful because first principle calculations based on lattice QCD at large baryon density are still not possible. In experiments at intermediate energies, where baryon density is quite large, integrating backwards hydrodynamic equations is the only possibility to gain information about initial state. At the same time, lack of a realistic hadronization theory makes backward integration of hydrodynamic equations ambiguous. This problem can be solved only by experimentally testing predictions of particular models. In all these hydrodynamic models a space-time F-Oh must be specified. After that Cooper-Frye formalism can be used to compute particle spectra and the final anisotropic flow pattern of hadrons [84]. Unfortunately, the Cooper-Frye prescription has serious problems too (see, e.g. Refs. [85]). Thus, the main disadvantages of the hydrodynamic approach is that both the initial and final (F-O) hypersurfaces must be specified. In reality, however, both these hypersurfaces are not sharp, but rather smooth transition layers [86]. In particular, hadron finite emission times indicate on smeared F-Oh. Thickness of the F-Oh depends on energy of collision [24]. As it was observed experimentally the higher is beam energy the smaller is thickness of F-Oh or hadron emission time. For instance, RHIC experiments suggest a very rapid F-O since measured two-particle correlation functions are consistent with an extremely short emission time in the local rest frame [87]. Therefore, as it was stated above, backtracing of experimental data to deduce initial conditions via suitable hydrodynamic scenario is rather ambiguous. This problem can be resolved by deriving some approach which incorporates evolution before and after F-O in unified way. The states of matter before and after F-O are radically different, since before F-O it is relativistic fluid and after F-O it is dilute relativistic gas of hadrons. In the first approximation this relativistic hadron gas can be also described by hydrodynamics. Therefore we have two fluids of vastly different densities constrained by dynamical boundary conditions applied on both sides of the finite width F-Oh. It can be shown by standard methods of mathematical physics that this system of Euler equations with specific boundary conditions can be reduced to a singular integro-differential equation [88]. Thanks to ef-

forts of Soviet mathematicians [89] efficient numerical methods have been developed to solve such equations. The other very promising approach was proposed in Ref. [90], where the hydrodynamical description of the QGP was supplemented at latter times by one of the hadronic transport models. Thermal distribution in this case serves as an input for subsequent cascade simulations. However, as was shown in Ref. [91], it is not so easy to connect both descriptions in a systematic and consistent way. Recently, in Ref. [92], it was proposed a gradual F-O with a finite transition layer instead of sharp hypersurface.

1.6 The problem of baryon stopping.

As measured by the BRAHMS collaboration [93], in central Au+Au collisions at highest RHIC energy $\sqrt{s_{NN}} = 200$ GeV the nuclear energy loss is very strong, about 70% of the initial kinetic energy. Obviously, the energy of produced particles and fields is taken entirely from the kinetic energy of colliding nuclei. An important result of the BRAHMS experiment is the measurement of the net-baryon rapidity distribution in a central rapidities region ($|y| < 3$). It demonstrates that a significant fraction of baryon charge has been transfered to this region.

Let us consider different mechanisms to describe phenomena of baryon stopping and particle production in high energy domain. In Ref.[95] a simple space-time model of baryon stopping at ultra-relativistic heavy ion collisions has been proposed. In this model baryon stopping was directly linked to the formation of strong chromofields. Nuclear trajectories were calculated under assumption that the field is neutralized at some sharp proper time τ_0. In this thesis we extend this model for the more general case when both time-dependent chromofield and partonic plasma are present. The basic idea is the same, i. e. to derive equations of motion of the baryonic slabs from the energy-momentum conservation. This approach makes it possible to relate the degree of baryon stopping and energy density of partonic plasma to the strength of the chromofield generated at the initial stage of the reaction. String-based or hadronic models like HSD [8] and uRQMD [7] can produce significant degree of baryon deceleration, which is associated with the action of strings. But these models are exceptionally well fitted to reproduce experimental data for intermediate energies. At higher energies deconfined state plays a major role, so concept of string becomes irrelevant. On the other hand, a string-based microscopic model qMD, where quark degrees of freedom are treated explicitly, is not able to produce sufficient baryon stopping [9]. This can be explained by insufficient string tension. It can be

corrected either by increasing the elementary parton-parton cross section or by assuming some additional mechanism which eventually generates larger string tension. It would be interesting to embed these string models to our model to explore transformation of partonic plasma to hadron gas.

The alternative way to describe production of parton plasma is advocated by parton cascade based models. This approach, however, gives no idea about evolution of the system, since quarks and gluons are assumed to be produced instantly with production rates calculated by pQCD. Observed excess of net-baryons at mid-rapidities for RHIC energies can be explained by parton cascade based model-VNI. As was shown in Ref.[55] already one parton scattering is sufficient to explain it. In this calculations collision term in Boltzmann equation includes all lowest-order pQCD scattering processes between massless quarks and gluons. Additionally, it was included the inelastic reactions $q \to qg$, $q \to q\gamma$, $g \to gg$ and $g \to q\bar{q}$ were included. The soft singularities in the showers are avoided by termination the branchings when the virtuality of the time-like partons drops below $\mu_0 = 1 GeV$. Initial parton distribution function of valence quarks is given by GRV-HO parameterization [96]. It should be noted that results are quite vulnerable to the factorization scale Q_0, and parameterization scheme for parton distribution.

Another possibility to study mid-rapidity region is to derive equation for quarks propagating across the strong background field by summing up the fan diagrams in the presence of the CGC as was done in Ref. [40]. The main result of this work is that valence quark distributions are power law behaved with non-integer powers in mid-rapidity region (for fixed coupling).

Among exotic mechanisms which can explain the drift of the net-baryon charge to central rapidities is the idea of baryon junction. Baryon junction can be thought as a topological knot in the gluon field configuration connecting the color flux tubes from three quarks into a color singlet gauge-invariant state [97]. This gluon knot carries baryon charge provided that baryon charge is conserved. At sufficiently high energies valence quarks of colliding nuclei do not have enough time to interact during collision, and they pass through each other leaving almost net-baryon free midrapidity region, provided that baryon number is associated with valence quarks, as assumed in naive quark model. On the other hand "string junction", composed of infinite number of wee gluons, has enough time for interaction. This leads to some stopped baryon junctions. These topological defects are seeds of new baryons, which are produced by condensation of sea quarks around them [98]. This mechanism has been implemented in HIJING/$B\bar{B}$ event generator [99], where it was shown, that, indeed, it can provide sufficient filling of midrapidity region.

Significant baryon stopping has also been observed at low energy of collision (AGS) [100], where the basic nucleon-nucleon mechanism of interac-

tion is different. Multi-fluid dynamics [101], as well as different versions of the kinetic models, like Vlasov-Uehling-Uhlenbeck (VUU, sometimes also called Boltzmann-Uehling-Uhlenbeck BUU [102]), and Relativistic Quantum Molecular Dynamics [103] models provide satisfactory description of reaction dynamics in this energy domain. The molecular dynamics models including mean fields are more advantageous, due to their ability to describe collective dynamics at low energies more realistically [104].

In Refs. [105] the net-baryon rapidity distribution for wide range of beam energies from AGS to RHIC was obtained as solution of the generalized Fokker-Plank equation with properly chosen drift and diffusion coefficients. This nonlinear Fokker-Plank equation describes anomalous diffusion in coordinate and momentum space. However, the microscopic mechanism for these processes was not specified in this work, that makes this approach somewhat abstract.

Apparently, the lower is the beam energy the larger is time interval, where dynamics is nonequilibrium. This is the first reason why transport models are more appropriate for low energies. There substantial part of nuclear stopping is generated on the strongly non-equilibrium hadronic stage of reaction. Therefore, viscosity and thermal conductivity are not appropriate for such situations, because by definition they are only suitabe for weak non-equilibrium. A possible way out is taking advantage of a multi-fluid approximation to heavy ion collisions, pioneered by Los Alamos group [106]. Approach to kinetic equilibrium at low energies, where the constituents of matter are mainly nucleons or their excited states, can be investigated by two [107] and three fluid models [17]. Two fluid dynamics can be derived from the Fokker-Plank equation which in turn follows from the system of Langevin equations. Interflow friction coefficient can be derived from Langevin equation by use of the Fokker-Plank expansion. Three fluid hydrodynamics considers time-delayed formation of a third baryon-free fluid of newly produced particles alongside with two baryon-rich fluids. After the formation it starts to interact with baryon-rich fluids and quickly gets thermalized. There the finite formation time of the third fluid was introduced, which is the conventional concept of the hadronic physics. It is associated with a finite time of string fragmentation. It is incorporated in the kinetic transport models such as UrQMD, QGSM and HSD. Along with assumption of finite formation time, it is assumed that the fireball matter gets quickly thermalized after its formation. The derivation of 3-fluid model is based on Boltzmann equation, which is valid strictly speaking only for dilute systems; the interaction between fireball and baryon-rich fluids is estimated on the basis of elementary hadron-hadron cross sections.

1.7   Description of the thesis

In the approach developed in this thesis to solve baryon stopping and partons production problems the coherent chromofield formation was explicitly assumed. As shown in [28], initial gluon dynamics in ultrarelativistic heavy ion collisions can be treated purely classically. Therefore, instead of dealing with baryon dynamics in quantized background field it is enough to consider interaction with classical field that is much simpler. This classical chromofield is formed shortly after collision of boost contracted nuclei. After that it decays gradually into the partons. To simplify the treatment it is assumed that these partons quickly thermalize and form a QGP [94]. Its evolution is described by the boost-invariant hydrodynamic equations with a source term describing chromofield decay rate. Further dynamics of hadronization and F-O, which might affect on the late stages of baryon stopping and particle production, though very interesting, is out of scope of this thesis. Since we treat the produced plasma as an ideal fluid, the entropy produced due to the field decay can be identified with parton multiplicity. A large amount of energy lost by net-baryons during collision can be considered as the signature of strong chromofields generated at the early stage of reaction.

Baryon stopping dynamics have been studied for different scenarious of chromofield decay. Experimental data for net-baryon rapidity spectra cannot be reproduced by the only value of parameter ϵ_0 in the whole rapidity interval. Larger energy densities correspond to mid-rapidity region, and lower for fragmentation region. This can be improved by taking into account rapidity dependence of saturation momentum, which goes in $\epsilon_f(\tau_0)$. We have considered two variants of calculations. In the first one the slab dynamics is assumed to be affected by the produced plasma, namely that the plasma particles crossing the slab trajectories are absorbed by the slabs. This leads to a very large increase of slab temperature and accordingly to the increase of average baryon transverse momentum. The plasma back reaction on baryon dynamics leads to the saturation of stopping power with increasing chromofield energy density or beam energy. It is interesting to note, that experimental data, measured at beam energies from AGS to RHIC, show rather logarithmic behavior than linear grows [93]. But mechanism of deceleration on this energy scale is different, since formation of strong chromofields there is hardly expected. Apparently, the influence of plasma is so strong because the boost invariant distribution of produced partons was assumed for simplicity, i.e. that plasma occupies the whole region between the slabs. This means that the edge effects were neglected. For instance, in Ref.[108], to cure this problem, initial conditions which take into account finite size of fluid were adopted for further isentropic evolution.

Most previous studies were done under assumption that the recoil effects do not affect significantly the baryon trajectories, i.e. that the source producing gluon fields moves nearly along the light cone. This fact was used in Ref. [2, 109] to compute quark and gluon structure functions in perturbative limit, as well as sea quark distribution in a hadron wave function at small x. The computations there were performed within an effective QCD motivated theory at small x (CGC model), where the gluon field can be treated classically. In contrast, our analysis shows that the recoil effect play an important role in the net-baryon dynamics and production of the QGP. It was proved numerically, that strong chromofields shift significantly initial net-baryon rapidity distribution to the mid-rapidity region. In the case without taking into account plasma back reaction the shift quantity depends strongly on the $\epsilon_f(\tau_0)$. On the other hand, the stronger is chromofield the stronger is back reaction of produced plasma, which prevents population of the midrapidity region. Our calculations in this case revealed that midrapidity region remains almost net-baryon free independently of how large $\epsilon_f(\tau_0)$ is.

Another extreme assumption is that the produced partonic plasma does not affect the dynamics of baryonic slabs. In this case the rapidity shift towards central rapidity is large enough to explain the observed rapidity loss. However the shape of the net-baryon rapidity distribution can not be reproduced by certain fixed values of the chromofield. We have tried to reproduce the BRAHMS data [93] by assuming color charge as gaussian random variable, or chromofield strength fluctuations. To be more specific, in accordance with the MV model [32], color charge is the classical random variable which fluctuates inside a region of transverse extent $\sim \frac{1}{Q_s}$, where Q_s is a so-called saturation scale. The average color charge in this region will be of course zero, but its square, which determines the chromofield energy density, is not. In fact, random color charge has a gamma distribution (2.22) with the mean value proportional to ϵ_0. Thus, various physical quantities, like number of emitted partons or net-baryon rapidity loss must be evaluated by averaging over many different evolutions corresponding to different initial chromofields. By this way contributions from higher energy densities are taken into account with appropriate statistical weight. This makes net-baryon rapidity distribution a more flat in the mid-rapidity region. But it is far not sufficient to reproduce the shape of experimental data at some fixed value of parameter ϵ_0. Therefore other mechanisms are required.

Experimental data can be fitted by all considered in this thesis chromofield decays, provided that strong plasma back reaction was not taken into account, and different values of parameter ϵ_0 were chosen for mid-rapidity and fragmentation regions. χ^2-analysis selects the power law of chromofield

decay with a reasonable decay time of about 0.6 fm as the most appropriate to fit the BRAHMS data. Corresponding initial chromofield energy densities are quite large: $30 - 50 GeV/fm^3$. Baryon transverse momentum is assumed generated only in the very initial hard processes.

It is important to keep in mind that our model is a very serious simplification of real physical process. The proper study of back reaction effects should be based on microscopic understanding of the particle production in a strong time-dependent finite-size field. In principle this can be done on the basis of Quantum Field Theory(QFT) or kinetic theory. For complete solution of this problem in QCD one should solve a set of coupled equations, including the Dirac equation and the Yang-Mills equation. Since this is a very difficult task, it is highly desirable to find a more practical method. This method should provide a direct connection between the field theory and kinetic theory. However, finding this precise connection is also a very challenging problem, which is also unsolved up to now. The further simplification is to introduce time-dependence artificially by some phenomenological external potential. For instance, in Ref.[48] the pair production process was studied by solving the kinetic equation derived by using the Bogoliubov transformation from Dirac/Klein-Gordon equation in external spatially homogeneous but time-dependent electric field. The particle producing source term in this kinetic equation is of non-Markovian character, even for the constant field. The Schwinger source term is reproduced in the low density limit. Interaction with classical external field leads to time-dependent dispersion relation.

We will use units with $\hbar = k_B = c = 1$ and Minkovski metric $g^{\mu\nu} = \text{diag}(1, -1, -1, -1)$ throughout this thesis.

Chapter 2

General formalism

2.1 Baryonic slabs

We consider only beam energies so high that before collision the nuclei can be thought of as very thin, Lorentz-contracted, sheets. Each sheet is divided into many small elements or slabs, of transverse area σ_0 labeled by an index a where $a = p$ for the projectile nucleus and $a = t$ for the target nucleus (see Fig. 1.3). Each slab is characterized by a baryon number N_a which is assumed to be strictly conserved.

We decompose a nucleus-nucleus collision into a multitude of pairwise collisions of individual slabs from projectile and target nuclei. Moreover, we assume that before and after the overlap at $t = 0$, both slabs propagate as rigid bodies in opposite directions along the beam axes z. The energy and momentum of slab a per unit area is parameterized in terms of its mass M_a and longitudinal rapidity Y_a (for more details see Ref. [107]),

$$E_a = M_a \cosh Y_a \ , \quad P_a = M_a \sinh Y_a \tag{2.1}$$

It is convenient to express M_a as

$$M_a = m_\perp \tilde{N}_a \tag{2.2}$$

where $m_\perp = \sqrt{m_N^2 + \langle p_\perp \rangle_\tau^2}$ is the baryon mean transverse mass, which is written in terms of the mean transverse momentum $\langle p_\perp \rangle_\tau$. As it will be demonstrated later, the time evolution of $\langle p_\perp \rangle_\tau$ strongly depends on the interaction with partonic plasma.

In the Glauber model [?] the average number of participants at impact parameter $\mathbf{b}$ is determined by integration over transverse plane:

$$N_{part}(\mathbf{b}) = \int d^2\mathbf{s} \left[\tilde{N}_p(\mathbf{b}, \mathbf{s}) + \tilde{N}_t(\mathbf{b}, \mathbf{s}) \right] \tag{2.3}$$

where
$$\tilde{N}_a(\mathbf{b}, \mathbf{s}) = A_a T_a(\mathbf{b}, \mathbf{s})(1 - (1 - \sigma_{NN} T_{\bar{a}}(\mathbf{b}, \mathbf{s}))^{A_{\bar{a}}}) \qquad (2.4)$$

is the number of participants from he nucleus a at transverse coordinate $\mathbf{s}$. Here A_a and $A_{\bar{a}}$ are baryon numbers of colliding nuclei, $\bar{a} = p$ for $a = t$ and vice versa, σ_{NN} is the total inelastic NN cross section. The profile function $T_a(\mathbf{b}, \mathbf{s})$ is introduced by integration of the baryon number density along the beam axis

$$T_a(\mathbf{b}, \mathbf{s}) = \frac{1}{A_a} \int \rho_a(\mathbf{r}) dz \qquad (2.5)$$

Below we use for $\rho_a(\mathbf{r})$ a Woods-Saxon parameterization consistent with nuclear data. It is obvious that the slab baryon number is given by

$$N_a(\mathbf{b}, \mathbf{s}) = \sigma_0 \tilde{N}_a(\mathbf{b}, \mathbf{s}) \qquad (2.6)$$

The number of nucleon-nucleon collisions within the slab area σ_0 is:

$$N_{coll}(\mathbf{b}, \mathbf{s}) = \sigma_0 \sigma_{NN} A_p A_t T_p(\mathbf{b} - \mathbf{s}) T_t(\mathbf{s}) \qquad (2.7)$$

The value of σ_0 serves as the coarse-graining scale for sampling string-like configurations sttretched between the slabs. Final results are not very sensitive to the choice of σ_0, and below we take it equal to the inelastic NN cross section σ_{NN}.

2.2   Region between the slabs

At sufficiently high collision energies the slabs will go through each other leaving behind a very unusual region occupied by strong chromofields and newly produced partons. It is most likely that vacuum condensates will be destroyed in this region so that chromofields and partons will live in a background of the perturbative QCD vacuum. We call this region "QCD vacuum bubble" or simply a "bubble". With time the bubble will expand, predominantly in the longitudinal direction, following the receding nuclear sheets. It is natural to assume that chromofields and partons can exist only inside the bubble. By expanding the bubble the color charges, localized on baryonic slabs, do work against the physical vacuum by expense of their kinetic energy. This picture follows from the Color Glass Condensate initial state proposed in Ref. [2] and studied in numerous subsequent works. In general, both transverse and longitudinal fieds can exist in bubble [6]. Although our approach can be easily formulated for arbitrary field configurations, below we consider only longitudinal chromoelectric fields characterized by strength $E_\parallel$. The transverse components of the chromofield, which certainly appear

in the Weizsäcker-Williams picture [2], in average will also act for the deceleration of color charges, but we shall put aside this issue until more detailed consideration. From a somewhat different point of view, the field configurations between the slabs can be represented as a collection of strings stretched between the projectile and target slabs. If the density of strings per unit transverse area is n, and string tensions for each string are equal $\sigma = \sigma_i$, then the energy density associated with this stringy field configuration is

$$\epsilon_f = \frac{1}{2}\mathbf{E}^2 = n\sigma \tag{2.8}$$

In ultrarelativistic heavy-ion collisions the string density may be so high that the individual string picture becomes meaningless. As pointed out by several authors [110, 111], at sufficiently high n the strings will fuse or even form percolated clusters, leading to more complicated configurations (see below). The energy-momentum tensor inside the bubble can be generally represented as

$$T^{\mu\nu} = T_{\text{vac}}^{\mu\nu} + T_{\text{field}}^{\mu\nu} + T_{\text{part}}^{\mu\nu} \; , \tag{2.9}$$

where the terms in the r.h.s. correspond to the vacuum, chromofield and partonic contributions, respectively. In the simplest consideration the vacuum contribution can be written as

$$T_{\text{vac}}^{\mu\nu} = Bg^{\mu\nu} \; , \tag{2.10}$$

where B is the "bag constant". In a particular case when only the longitudinal chromoelectric field is present, the energy-momentum tensor has the form

$$T_{\text{field}}^{\mu\nu} = \epsilon_f \cdot \text{diag}(1, 1, 1, -1) \; , \tag{2.11}$$

where ϵ_f is the energy density of the field. As explained in Ref. [112], by performing a proper Lorentz boost, one can obtain this diagonal form for the energy-momentum tensor for any field configuration, except the case when $\mathbf{E}$ and $\mathbf{H}$ are perpendicular and have equal values. By inspecting equations (2.10) and (2.11) one can notice that the vacuum contribution corresponds to a positive energy density $\epsilon_{vac} = B$ and a negative isotropic pressure $p_{vac} = -B$. But the pressure associated with the chromoelectric field is anisotropic, i. e. negative in the longitudinal direction and positive in the transverse direction with respect to the field. Therefore, in particular case when $\epsilon_f = B$ the transverse pressure vanishes. This observation was used by several authors (see e.g. Refs. [5, 117, 51, 118]) for modeling the color flux tube by combining chromo-electro-magnetic and scalar fields. At the same time, the longitudinal pressure components for both the vacuum and

the chromofield are both negative and act against of expansion of the bubble. In our calculations below we disregard effects of the transverse pressure on the slabs' longitudinal motion.

The last term in Eq. (2.9) is associated with the partonic contribution. This could be minijets produced at the very early stage of the collision [4], or partons produced later at the decay of the chromofield. We parameterize this contribution in a general form appropriate for a perfect fluid,

$$T_{\text{part}}^{\mu\nu} = (\epsilon + p)u^\mu u^\nu - pg^{\mu\nu} \tag{2.12}$$

where ϵ and p are the energy density and pressure of partonic plasma, and u^μ is its collective 4-velocity. Different physical situations can be modeled by choosing different equations of state $p(\epsilon)$ ranging from a free-streaming partonic system ($p = 0$) to an ideal quark-gluon plasma ($p \approx \epsilon/3$). For our numerical simulations further on we will use only ideal gas equation of state. Again, we assume that at early stages the plasma only expands in the longitudinal direction, i.e. $u^\mu = \gamma(1, 0, 0, v)$ and $\gamma = 1/\sqrt{1 - v^2}$.

2.3   Initial Chromofield Energy Density

In this section we follow the ideas formulated in Refs. [2, 6] and widely referred to now as the Color Glass Condensate initial state. Within this picture, random color charges are generated on the nuclear sheets as a result of soft gluon exchange at the interpenetration stage of a nuclear collision. In a single event these charges fluctuate from point to point in the transverse plane. The charges also fluctuate from event to event, so that in average over many events the areal charge is zero. It is convenient to introduce the color charge density, $\rho(\eta, \mathbf{b}, \mathbf{s})$, as a function of coordinate in transverse plane: $(\mathbf{b}, \mathbf{s})$ and longitudinal pseudorapidity: $\eta = \frac{1}{2} \ln \frac{t+z}{t-z}$. Following Refs. [2, 6] we assume it as a stochastic variable distributed with the Gaussian weight:

$$P[\rho] \sim \exp\left[-\int d\eta d^2\mathbf{s} \frac{1}{2\mu_a^2(\eta, \mathbf{b}, \mathbf{s})} Tr\rho^2(\eta, \mathbf{b}, \mathbf{s})\right] \tag{2.13}$$

where μ_a^2 is the corresponding variance. For our estimates below we disregard possible dependence of μ_a on (**b**,**s**) and η. Then, after integrating out η in Eq. (2.15) we introduce a new color charge density as only a function of transverse coordinates,

$$\rho^2(\mathbf{b}, \mathbf{s}) = \int d\eta \rho^2(\eta, \mathbf{b}, \mathbf{s}) \tag{2.14}$$

which is treated as a random variable with the Gaussian weight

$$P[\rho] \sim \exp\left(-\frac{1}{2\mu_a^2} \int d^2\mathbf{s} Tr \rho^2(\mathbf{b}, \mathbf{s})\right),\tag{2.15}$$

where Tr is taken over color indecies.

These fluctuations are characterized by a certain scale in the transverse plane, which is related to the saturation scale $\mathcal{A} \approx \frac{1}{Q_s}$ introduced in high-density QCD [35]. Since the transverse size of the baryonic slabs σ_0 is assumed to be much larger, this means that many string-like configurations (flux tubes) are stretched between the receding slabs. In this situation we can divide each slab into n small elements with equal transverse area $\mathcal{A} = \frac{\pi}{Q_s^2}$, corresponding to the resolution scale $\sim \frac{1}{Q_s}$ of hard probe at given energy, so that they cover the total slab area, i.e. $\sigma_0 = n\mathcal{A}$. Each flux tube configuration connects the spots of opposite charge, $\pm Q_i$, like in capacitor. In Abelian approximation the chromoelectric field strength in a static flux tube is obtained from the Gauss theorem [5],

$$E_i = \frac{Q_i}{\mathcal{A}} \equiv \rho_i \tag{2.16}$$

Then the force acting between opposite spots or string tension σ_i is

$$F_i = \frac{1}{2} Q_i E_i = \frac{1}{2} \rho_i^2 \mathcal{A} = \mathcal{A}\epsilon_i = \sigma_i \tag{2.17}$$

where ϵ_i is the energy density of the chromofield in the color flux tube. For simplicity we neglect contribution of bag constant here. It is important to note, that all flux tubes produce attractive force between opposite spots on the projectile and target slabs. The force lines and their structure are schematically dislayed in Fig. 1.3. The total force acting on each slab is then

$$F_a = \sum_{i=1}^{n} F_i = \frac{1}{2} \mathcal{A} \sum_{i=1}^{n} \rho_i^2 \,, \quad a = p, t \tag{2.18}$$

Accordingly, we can represent the integral in Eq. (2.15) as the sum over all elements, so that

$$P(\rho_1, \ldots, \rho_n) \sim \exp\left(-\frac{\mathcal{A}}{2} \sum_{i=1}^{n} \frac{\rho_i^2}{\mu_i^2}\right) = \prod_{i=1}^{n} \exp\left(-\frac{\mathcal{A}\rho_i^2}{2\mu_i^2}\right) \tag{2.19}$$

Obviously, the event-by-event distribution of color charge in each element follows the Gaussian distribution

$$P(\rho_i) = \sqrt{\frac{\mathcal{A}}{2\pi\mu_i^2}} \exp\left(-\frac{\mathcal{A}\rho_i^2}{2\mu_i^2}\right) \tag{2.20}$$

Therefore, in accordance with Eq. (2.17) mean values of force acting between two spots and the initial chromofield energy density are expressed as

$$< F_i >= \frac{\mu_i^2}{2} \ , \quad \langle \epsilon_i \rangle = \frac{\mu_i^2}{2\mathcal{A}} \tag{2.21}$$

The next step is to calculate the distribution of the total force acting between the slabs for an ensemble of events. This distribution is obtained by integrating $\delta(F - \sum_i F_i)$ over all charge densities ρ_i with weight $P(\rho_i)$. Taking for simplicity $\mu_1^2 = \ldots = \mu_n^2 = \mu^2$ we have:

$$w(F) = \prod_{i=1}^{n} \left(\int_{-\infty}^{\infty} P(\rho_i) d\rho_i \right) \delta \left(F - \frac{1}{2}\mathcal{A} \sum_{k=1}^{n} \rho_k^2 \right)$$

$$= \left(\frac{\mathcal{A}}{2\pi\mu^2} \right)^{n/2} \int \delta \left(F - \frac{\mathcal{A}\rho^2}{2} \right) \exp \left(-\frac{\rho^2}{\mu^2} \right) \frac{2\pi^{n/2}}{\Gamma(n/2)} \rho^{n-1} d\rho = \frac{1}{\Gamma(n/2)\mu^2} \left(\frac{F}{\mu^2} \right)^{n/2-1} e^{-\frac{F}{\mu^2}} \tag{2.22}$$

In the second expression we have used $O(4)$ symmetry of the integrand and made transformation to spherical coordinates in n-dimensional ρ space. As a result we get a gamma-distribution which has the following first moments:

$$< F >= \frac{n}{2}\mu^2 \ , \quad \sigma_F = \sqrt{\frac{n}{2}}\mu^2 \tag{2.23}$$

One can see that the parameter μ^2 introduced in Refs. [2, 6] in fact determines the mean force between the slabs and its dispersion. It is more convenient to express the mean energy density of the chromofield in the space between the slabs as:

$$\epsilon_f(\tau_0) = \frac{< F >}{\sigma_0} = \frac{\mu^2}{2\mathcal{A}} \tag{2.24}$$

Determination of parameter μ^2 is somewhat unbiguous. Discussion on this matter can be found in Ref. [30]. Therefore, we have to use some approximation for $\epsilon_f(\tau_0)$. We will follow a simple parameterization proposed in Ref. [95].

$$\epsilon_f(\tau_0) = \epsilon_0 \left(\frac{s}{s_0} \right)^{\lambda} N_{coll}(\mathbf{b}, \mathbf{s})^{\beta}, \tag{2.25}$$

where ϵ_0 has a sense of the mean energy density in an individual string and is considered as an adjustable parameter. The second factor is motivated by

the small x behavior of the gluon structure function, which is consistent with $\lambda = 0.3$ [29]. The last geometrical factor is introduced to take into account the fact that, in the case of independent strings the field energy density should be proportional to the number of binary NN collisions ($\beta = 1$). But at higher energies percolated clusters of strings can be formed. As was shown in Refs. [110, 111] this should lead to $\beta = 0.5$. Below we consider the case of $\beta = 1$ only. Moreover we have neglected rapidity dependence of $\epsilon_f(\tau_0)$ as follows from the transition from Eq. (2.13) to Eq. (2.15). According to our calculations below, parameter ϵ_0 varies within the range from 0.2 GeV/fm^3 to 3.0 GeV/fm^3 depending on the chromofield decay scenario and quantities to be calculated. The inelastic NN cross section at RHIC energy has value $\sigma_{NN} = 4.21$ fm^2 [113]. For central Au+Au collisions at RHIC energies the value $Q_s^2 \approx 1.44$ GeV^2 calculated in Ref. [27] was used. Thus, the "charged spots" on the transverse plane, where the color charge is essentially nonzero, have the characteristic area $\mathcal{A} = \frac{\pi}{Q_s^2} \approx 0.09$ fm^2.

2.4 Evolution of the chromofield

For sake of simplicity we disregard a short time delay, ~ 0.1 fm, which is needed for formation of the coherent field [4]. At $t > 0$ the region occupied by the field expands following color sources at the baryonic slabs. In the other words the field is nonzero only in the region constrained by the instantaneous slab positions, $z_t(t) < z < z_p(t)$. At later time the field decays gradually into quark and gluon pairs. For our further discussion we use the light-cone variables τ, η. We incorporate approximate boost invariance of the field configurations by assuming that the field energy density is a function of the proper time only $\epsilon_f(\tau)$. This means that we disregard the finite size and edge effects which have been studied earlier by several authors [49, 52]

Let us consider several examples. In the FTM [1, 3, 4] the field decay is caused by the quark and gluon pair creation via the Schwinger mechanism [47]. Quite generally the evolution equation for the field energy density can be written as [4]

$$\frac{d\epsilon_f}{d\tau} = - \left[\kappa(2\epsilon_f)^{5/4} + 2\sigma_c\epsilon_f \right] \ , \tag{2.26}$$

where the first term comes from the pair creation and the second one accounts for the Ohmic heating of produced partons. In Ref. [3] the constant κ was estimated in the Abelian approximation for massless partons,

$$\kappa = \frac{(4\pi\alpha_s)^{5/4}\zeta(5/2)}{16\pi^3} \left[\nu_B + (1 - 2^{-3/2})\nu_F \right] \ , \tag{2.27}$$

where $\nu_{B(F)}$ is the degeneracy factor for bosons (fermions) and α_s is the strong fine-structure constant. Corresponding degeneracy factors for quarks and gluons are

$$\nu_F = \nu_q = 2N_c N_f, \quad \nu_B = \nu_g = 2(N_c^2 - 1) \tag{2.28}$$

where $N_c = 3$ is the number of colors, and N_f is the number of quark flavors. In the numerical simulations we take $N_f = 2.5$ to take into account a non-zero mass of strange quarks. Expressions for the color conductivity σ_c can be found in Refs. [4]. At $\sigma_c = 0$ Eq. (2.26) has a simple analytical solution [4]:

$$\epsilon_f(\tau) = \epsilon_0 \left[1 + \frac{\tau}{\tau_d}\right]^{-4} , \tag{2.29}$$

where $\tau_d = 2/\left(\kappa(2\epsilon_0)^{1/4}\right)$ is a characteristic decay time and ϵ_0 is the initial field energy density. A somewhat different decay law of chromofield, $1 - (\tau/\tau_d)^3$, was suggested in Ref. [5].

In the CGC model, Refs. [2, 6], the gluon field evolution is governed by nonlinear equations derived from the QCD. Without going into details we point out only that according to this model the chromofield has not only transverse but also longitudinal component. Moreover, the longitudinal fields dominate at the early times. This follows from results of Ref. [6] which were derived for low density limit in the covariant gauge

$$x^+ A^- + x^- A^+ = 0 \tag{2.30}$$

In thi gauge light-cone vector potentials of the chromofield are expressed as

$$A^\pm = \pm x^\pm \alpha(\tau, x_\perp) \tag{2.31}$$

where $x^\pm = (t \pm z)/\sqrt{2}$ are the light-cone coordinates and function $\alpha(\tau, x_\perp)$ is perturbative solution of classical Yang-Mills equation, where color charge density serves as expansion parameter. As shown in the same paper, its Fourier transform over transverse coordinates is given by the Bessel function,

$$\alpha_k(\tau) = \alpha_k(0) \frac{2}{\omega_k \tau} J_1(\omega_k \tau) , \tag{2.32}$$

where $\omega_k = \sqrt{\mathbf{k}_\perp^2}$, and $\mathbf{k}_\perp$ is the transverse wave vector. A longitudinal field configuration of this type was used recently in Ref. [119] as external potential for the pair production problem in (1+1)-dimensional Dirac equation. Using standard definitions, one can get the longitudinal field strength for mode $k_\perp$ as

$$E_\parallel(\tau, \mathbf{k}_\perp) = 2\alpha_k + \tau \frac{d\alpha_k}{d\tau} = \alpha_k(0) J_0(\omega_k \tau) . \tag{2.33}$$

Accordingly, the field energy density can be expressed as

$$\epsilon_f(\tau) = \frac{1}{2}E_\parallel^2 = \epsilon_f(\tau_0)J_0^2(\omega_k\tau) \ . \tag{2.34}$$

This solution describes damped oscillations with the characteristic period $\sim 1/\omega_k$. Asymptotically the amplitude of oscillations decreases as $1/\tau$. In our estimates below we take $\omega_k = k_\perp \approx Q_s$, where Q_s is a saturation scale, Ref. [6, 27]. Since the field regeneration is physically unrealistic we shall cut evolution on the first zero of Bessel function at $\tau = 2.4/Q_s = 0.4$ fm for $Q_s = 1.2$ GeV.

Besides of these two cases of the field decay we will also consider an exponential decay

$$\epsilon_f(\tau) = \epsilon_f(\tau_0)e^{-\Gamma\tau}, \tag{2.35}$$

which follows from Eq. (2.26), when Ohmic heating term is dominating. In this case $\Gamma = 2\sigma_c$, and we take $\Gamma \approx 2.5/$fm in the numerical calculations.

2.5 Creation of partonic plasma

Decay of the chromofield results in the production of quarks and gluons that eventually leads to the formation of thermalized quark-gluon plasma. We are not going to study here all aspects of the thermalization process. Instead, we adopt a simple picture which is often used for describing the reheating process in cosmological inflation models (see e.g. [120]). Namely, we assume that the energy and momentum of the classical field are transferred into the equilibrated partonic plasma. In Ref. [95] this process was assumed to happen at a fixed proper time $\tau = const$. Then the energy and momentum conservation equations take a simple form,

$$T_{\text{part}}^{\mu\nu}d\Sigma_\nu = T_{\text{field}}^{\mu\nu}d\Sigma_\nu, \tag{2.36}$$

where hypersurface separating the region of field and the region of plasma is parameterized as

$$d\Sigma_\mu = d^2\mathbf{s}(dz, 0, 0, -dt) \tag{2.37}$$

Using Eqs.(2.11) and (2.12) we can rewrite these equations explicitly as

$$\left[(\epsilon + p)\gamma^2 - p\right]dz - \left[(\epsilon + p)\gamma^2 v\right]dt = (\epsilon_f + B)dz \ , \tag{2.38}$$
$$\left[(\epsilon + p)\gamma^2 v\right]dz - \left[(\epsilon + p)\gamma^2 v^2 + p\right]dt = (\epsilon_f + B)dt \ , \tag{2.39}$$

where dz and dt are taken along the hyperbola $\tau = const$, i.e. $tdt - zdz = 0$. One can easily see that these equations require

$$v(\tau_0) = \frac{z}{t} \ , \quad \epsilon(\tau_0) = \epsilon_f(\tau_0) \ , \tag{2.40}$$

which are exactly the Bjorken initial conditions for scaling hydrodynamics [13], [1].

In a more realistic consideration one should deal with a continuous transformation of chromofield into plasma. Still, one can derive a simple equation for the plasma evolution even in this more general case. This is achieved by using the local energy-momentum conservation equations, $\partial_\nu T^{\mu\nu} = 0$, which give generalized hydrodynamical equations. We assume that the chromofield energy density and the plasma energy density are functions of the proper time only, and defined in the finite interval of η: $\eta_t(\tau) \leq \eta \leq \eta_p(\tau)$. As follows from Eqs.(2.38),(2.39) in this case produced plasma has a Bjorken-like velocity field, $v = \frac{z}{t}$, and the hydrodynamical equations reduce to

$$\frac{\partial \epsilon}{\partial \tau} + \frac{\epsilon + p}{\tau} = -\frac{\partial \epsilon_f}{\partial \tau} \ . \tag{2.41}$$

This equation contains in the r.h.s. the source term due to the parton production from the chromofield. For given $\epsilon_f(\tau)$ Eq. (2.41) has a simple analytical solution. Taking equation of state for plasma in the form $p = c_s^2 \epsilon$ with constant sound velocity c_s, we get

$$\epsilon(\tau) = [\epsilon(\tau_0) + \epsilon_f(\tau_0)] \left(\frac{\tau_0}{\tau}\right)^{1+c_s^2} - \epsilon_f(\tau) + \frac{1+c_s^2}{\tau^{1+c_s^2}} \int_{\tau_0}^{\tau} \epsilon_f(\tau) \tau^{c_s^2} d\tau \ , \tag{2.42}$$

Here the initial condition for ϵ and ϵ_f is defined at proper time τ_0 which in principle can be moved arbitrarily close to zero. Now one can study dynamics of the plasma formation from the initial state, where the energy density was mainly stored in the chromofield.

To illustrate the general trend, let us consider an exponential field decay, $\epsilon_f(\tau) = \epsilon_f(\tau_0) \exp\left[-\Gamma\left(\tau - \tau_0\right)\right]$, where the decay rate is controlled by parameter $\Gamma \approx 2.5/\text{fm}$. The integral in Eq. (2.42) can be done analytically for $c_s^2 = 0$. This case corresponds to free-steaming partons ($p = 0$), and is especially appropriate for the early stages of plasma evolution. Eq. (2.42) gives in this case

$$\epsilon(\tau) = \epsilon(\tau_0)\frac{\tau_0}{\tau} + \epsilon_f(\tau_0)\left[\left(1 + \frac{1}{\tau_0 \Gamma}\right)\frac{\tau_0}{\tau} - \left(1 + \frac{1}{\tau \Gamma}\right)\exp\left[-\Gamma\left(\tau - \tau_0\right)\right]\right] \ , \tag{2.43}$$

where $\epsilon(\tau_0)$ is the initial energy density of partons (minijets). It is easy to find that starting from the initial state without partons $\epsilon(\tau_0) = 0$, at $\tau_0 = 0.01$ fm, the plasma energy density reaches its maximum value, $\epsilon_{\max} \approx 0.3\epsilon_f(\tau_0)$,

---

[1]In Ref. [95] the terms with dt in the l.h.s. of Eqs.(2.38) and (2.39) were missing that lead to an erroneous result for $\epsilon_f(\tau_0)$ as a function of η

at $\tau_{\max} \approx 1.79/\Gamma$. A similar behavior was found in Ref. [4] for the power-law field decay defined by Eq. (2.29), where $\epsilon_{\max}$ is only about $0.2\epsilon_f(\tau_0)$. In that paper the initial field energy density was taken for minijet initial state and evolution was started at $\tau_0 = 0.1$ fm. In our calculations we start evolution at even earlier time $\tau_0 = 0.01$ fm and neglect minijets contribution to the energy density.

A substantial reduction of the plasma energy density as compared with the initial field energy density is the common feature of all realistic calculations with the continuous plasma production. This important observation must be taken into account when estimating initial energy density of the plasma by extrapolating backward the hydrodynamical evolution.

We have considered several functional forms for the time dependence of the chromofield, resulting in the different plasma production rates and baryon deceleration patterns. Corresponding results are displayed in Fig. 2.1 for exponential and power law of chromofield decay as well as for the CGC and 'cosh-like' cases; 'cosh-like' field decay with

$$\epsilon_f(\tau) = \epsilon_f(\tau_0)/\cosh^4((\tau - \tau_0)/\tau_d) \qquad (2.44)$$

was proposed in Ref. [127] to study e^+e^- pair creation in the pulse of strong laser field (this case can be solved analytically, and was used as a benchmark for our numerical results). It is seen that the maximum plasma energy density reaches only 20% of the $\epsilon_f(\tau_0)$ for the power law (2.29) and 40% for the CGC (2.34) decay law. Among all considered cases the exponential decay law (Fig. 1a) leads to the longest survival of the chromofield and slowest production of the partonic plasma.

2.6   Equations of motion

After the collision at $t = 0$ the trajectories of the projectile and target slabs, $z_p(t)$ and $z_t(t)$, are affected by the energy and momentum losses due to the generation of classical fields and production of partons.

First assume that the chromofields and partonic plasma are confined between the baryonic slabs. Therefore, the slabs have normal vacuum from one side and excited QCD matter from the other. Then, the infinitesimal decrement of the 4-momentum of a slab a, dP_a^μ, after traversing distance dz in time dt must be equal to the increment of the energy and momentum contained in the QCD bubble. The latter quantities can be expressed in terms of the energy-momentum tensor as $dP_a^\mu = T^{\mu\nu}d\Sigma_\nu$, where $d\Sigma^\nu$ is an infinitesimal 4-vector orthogonal to the hypersurface constrained by dt, dz
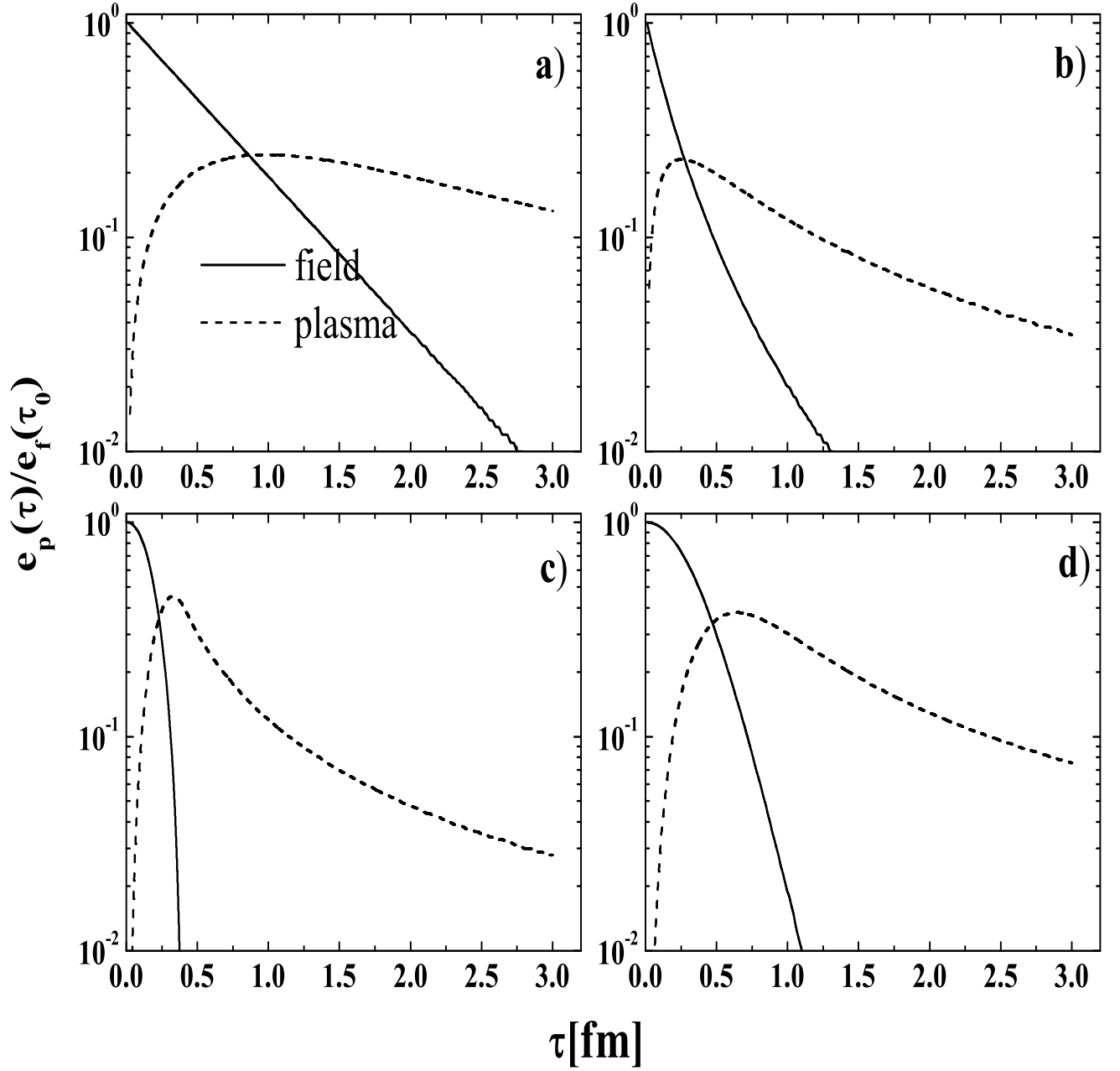
Figure 2.1: Evolution of the chromofield(thin solid line) and QGP(thick solid line) energy density in the units of the initial chromofield energy densities $e_f(\tau_0)$ for different assumptions concerning chromofield decay: a) exponential decay ($\tau_d = 0.6$ fm); b) power-law decay ($\tau_d = 0.6$ fm); c) CGC decay (evolution is cutted at the first zero of Besel function $\tau = 2.41/Q_s$ fm, see the text); d) 'cosh-like' chromofield decay ($\tau_d = 0.6$ fm).

and unit transverse area [84]. Assuming that the chromofield has only longitudinal components, the energy and momentum conservation equations can be written as

$$dE_a = -\left[T^{00}dz - T^{03}dt\right] , \qquad (2.45)$$
$$dP_a = -\left[T^{30}dz - T^{33}dt\right] . \qquad (2.46)$$

Eqs.(2.45) and (2.46) describe the classical trajectories of baryonic slabs, $z_p(t)$ and $z_t(t)$, with the initial conditions: $z_p(\tau_0) = z_t(\tau_0) \approx 0$, $y_p(\tau_0) = y_0$, $y_t(\tau_0) = -y_0$. Using Eqs.(2.10), (2.11) and (2.12), these equations can be rewritten in explicit form (for brevity we drop index a),

$$dE = -\left[A(\tau)\gamma^2 + B(\tau)\right]dz + \left[(A(\tau)\gamma^2 v\right]dt , \qquad (2.47)$$
$$dP = -\left[A(\tau)\gamma^2 v\right]dz + \left[A(\tau)\gamma^2 v^2 - B(\tau)\right]dt , \qquad (2.48)$$

where we have simplified the notations as

$$A(\tau) = \epsilon + p , \quad B(\tau) = \epsilon_{\text{vac}} + \epsilon_f - p . \qquad (2.49)$$

It is worth noticing that $A(\tau)$ is in fact the plasma enthalpy density, and $B(\tau)$ is the total longitudinal pressure taken with negative sign. Let us rewrite the instantaneous slab velocity V and the local parton velocity v as

$$V \equiv \frac{dz}{dt} = \tanh Y , \quad v = \frac{z}{t} = \tanh \eta . \qquad (2.50)$$

Then one can derive simple kinematic relations, valid on the slab trajectories,

$$\frac{dt}{d\tau} = \frac{\cosh Y}{\cosh (Y - \eta)} , \quad \frac{dz}{d\tau} = \frac{\sinh Y}{\cosh (Y - \eta)} , \quad \tau\frac{d\eta}{d\tau} = \tanh (Y - \eta) . \quad (2.51)$$

Now we can combine Eqs. (2.47), (2.48), and (2.51) to the following two equations

$$\left(\frac{dE}{d\tau}\right)^2 - \left(\frac{dP}{d\tau}\right)^2 = \left(\frac{dM}{d\tau}\right)^2 - M^2\left(\frac{dY}{d\tau}\right)^2$$
$$= [A(\tau) + B(\tau)]^2 \tanh^2 (Y - \eta) - B^2(\tau) , \qquad (2.52)$$

$$E\left(\frac{dE}{d\tau}\right) - P\left(\frac{dP}{d\tau}\right) = M\left(\frac{dM}{d\tau}\right)$$
$$= -A(\tau)M \sinh (Y - \eta) . \qquad (2.53)$$

After combining Eqs.(2.52), (2.53) and (2.51) one has

$$\frac{M}{\tau}\frac{dY}{d\eta} = A(\tau)\sinh(Y-\eta) - \frac{B(\tau)}{\sinh(Y-\eta)} \ . \tag{2.54}$$

After some additional algebra we obtain two coupled equations governing the motion of the baryonic slab

$$\frac{d\tilde{P}}{d\tau} = -B(\tau) - \frac{\tilde{P}}{\tau} \ , \tag{2.55}$$

$$\frac{dM^2}{d\tau} = -2A(\tau)\tilde{P} \ , \tag{2.56}$$

where $\tilde{P} = M\sinh(Y-\eta)$ is the slab momentum in the local frame moving with the slab pseudorapidity η. It is interesting that the plasma enthalpy density $A(\tau)$ has dropped out from equation (2.55). In the other words, the slab acceleration is determined entirely by the pressure difference $B(\tau) = \epsilon_{\text{vac}} + \epsilon_f - p$ from inside and outside the QCD bubble. Obviously, the slab will decelerate only if $B(\tau) > 0$, i.e. when the field and vacuum pressure dominates over the counter pressure of the plasma. Such situation is expected at early stages of the reaction when partonic plasma is in the free-streaming regime ($p \approx 0$). At later stages, when the field decays and plasma pressure builds up, the slab may re-accelerate again. The origin of this effect is very simple: when deriving equations (2.55) and (2.56) we have implicitly assumed that the plasma particles, whose trajectories are intercepted by the slab trajectory, are absorbed by the slab. This explains also the increase of the slab mass, as predicted by Eq. (2.55) at $A(\tau) > 0$ and $Y < \eta$.

Eq. (2.55) has an obvious solution

$$\tilde{P}(\tau) = \tilde{P}_0\frac{\tau_0}{\tau} - \frac{1}{\tau}\int_{\tau_0}^{\tau} B(\tau')\tau'd\tau' \ , \tag{2.57}$$

where the initial condition $\tilde{P}(\tau_0) = \tilde{P}_0$ is imposed. In the case of free motion ($B(\tau) = 0$) the first term in this equation describes gradual alignment of the initial velocity
$V_0 = \tanh Y_0$ along the ray $\frac{z}{t} = V_0$ or $\lim_{\tau\to\infty}\eta(\tau) = Y_0$. From Eq. (2.56) one obtains expression for the effective slab mass squared

$$M^2(\tau) = M^2(\tau_0) - 2\int_{\tau_0}^{\tau} A(\tau')\tilde{P}(\tau')d\tau' \ , \tag{2.58}$$

where $M(\tau_0) \equiv M_0$ is the initial slab mass, which was generated due to hard gluon exchange at early times, $\tau \sim 0$.

One can use the same equations to study another extreme situation, when the slabs are transparent for the partonic plasma produced at the early stages. If the plasma expands to the regions beyond the slabs, its pressure from inside and outside is equal, and one can simply drop it out from the energy-momentum conservation equations (2.47),(2.48). This equivalent to redefine the functions in Eq. (2.49) as

$$A(\tau) = 0 \quad , \quad B(\tau) = \epsilon_f(\tau) \tag{2.59}$$

In other words the slabs motion is only affected by the residual chromofield. This case is considered below in order to understand the role of plasma back reaction (see Sect. VIIIB).

Despite of their simple form Eqs.(2.55),(2.56) reflect important physics of ultrarelativistic nuclear collisions. Namely they allow to study the influence of a chromofield decay scenario and plasma back reaction on the baryon stopping. Integration of Eq. (2.55) was carried out by the routine based on a Chebyshev interpolation algorithm [116]. For the number of interpolation nodes $N = 40$ the 5% accuracy was achieved as follows from the comparison with analytical results for a constant field, Eq. (2.63).

2.7 Some interesting examples

In this section we shall present analytical and numerical results for several physically interesting cases.

2.7.1 Vacuum cleaner

Let us first discuss a simplest case when the region between the slabs is represented by the perturbative QCD vacuum characterized by the bag constant B. This is of course a non-realistic situation when no chromofield or partonic plasma is produced as the result of binary slab collisions. The baryonic slabs work in this case as a vacuum cleaner removing all nonperturbative condensates from the region between them and forcing transition into a false vacuum state. As follows from Eq. (2.56) at $A(\tau) = 0$, the slab mass remains constant, $M(\tau) = M(\tau_0) = M_0$. Then the deceleration equation (2.57) has a very simple solution

$$\tilde{P}(\tau) = \tilde{P}_0 \frac{\tau_0}{\tau} - \frac{B}{2\tau} \left(\tau^2 - \tau_0^2 \right) \quad . \tag{2.60}$$

Taking $\tau_0 = 0$ we get

$$\sinh(Y - \eta) = - \left(\frac{B\tau}{2M_0} \right) \quad . \tag{2.61}$$

On the other hand, from Eq. (2.54) with $A = 0$ and $B(\tau) = B = const$ one finds that

$$\frac{dY}{\tau d\eta} = -\frac{B}{M_0 \sinh (Y - \eta)} = \frac{2}{\tau} \ . \tag{2.62}$$

With initial condition $\eta(\tau_0) = Y_0$ this leads to the relation $\eta = (Y + Y_0)/2$. Finally we obtain the slab trajectory

$$\eta(\tau) = Y_0 - \text{Arcsinh} \left(\frac{B\tau}{2M_0} \right) \ . \tag{2.63}$$

In a similar context this solution was earlier discussed in Ref. [121]. If the vacuum bubble would exist forever, Eq. (2.63) would predict a "yo-yo" type motion for slab pairs [124]. In particular, the slabs will go through the turning point ($Y = 0$) at $\tau_1 = 2M_0 \sinh (Y_0/2)/B$ or $t_1 = M_0 \sinh Y_0/B$. Later on they collide again at $\eta = 0$ and $t = 2t_1$ and so on. Parametrically, the period of oscillations is long, because it is proportional to $\sinh Y_0$, where Y_0 is the initial beam rapidity. In reality the vacuum bubble will decay in a much shorter time.

2.7.2   Stringy state

Now we consider multi-string configurations where only the longitudinal chromoelectric fields are present. This case represents the earliest stages of the deceleration process when the fields are strong and almost no partonic plasma is present. Since in this case $A(\tau) = 0$, the slab mass remains constant, $M = M_0$, irrespective of time-dependence of the field. Possible scenarios of the field evolution were described in Sect. IIC.

Let us represent the field energy density as $\epsilon_f(\tau) = \epsilon_f(\tau_0)f(x)$, where $\epsilon_f(\tau_0)$ is its initial value parameterized in Eq. (2.25), and $f(x)$ is an arbitrary (decreasing) function of the dimensionless variable $x = \tau/\tau_d$ with τ_d being a characteristic decay time. Obviously, $f(x_0) = 1$, where $x_0 = \frac{\tau_0}{\tau_d}$. Introducing the dimensionless parameter

$$\alpha = \epsilon_f(\tau_0)\tau_d/M_0, \tag{2.64}$$

we can rewrite Eq. (2.57) with $\tilde{P}_0 = 0$ as

$$\sinh (Y - \eta) = -\alpha F(x) \ , \ \ F(x) \equiv \frac{1}{x} \int_{x_0}^{x} f(x')x'dx' \ . \tag{2.65}$$

From Eq. (2.54) we get

$$\frac{dY}{d\eta} = -\alpha \frac{xf(x)}{\sinh (Y - \eta)} = \frac{xf(x)}{F(x)} \ . \tag{2.66}$$

After differentiating Eq. (2.65) by x and eliminating $dY/d\eta$ by Eq. (2.66) we get an explicit expression for the slab pseudorapidity

$$\eta(x) = \eta(x_0) - \int_{x_0}^{x} \frac{\alpha F(x')}{\sqrt{(\alpha F(x'))^2 + 1}} \frac{dx'}{x'} \ . \tag{2.67}$$

Now calculations can be easily done for any specific $f(x)$. For instance, the choice $f(x) = 1$ corresponds to the time-independent chromofield, $\epsilon_f(\tau) = \epsilon_f(\tau_0)$, which is formally equivalent to the false vacuum case considered in the previous subsection. In this case $F(x) = x/2$ (for $x_0 = 0$) and, apart of notations, Eq. (2.67) gives the same result as Eq. (2.63). Numerical calculations of slab rapidities $Y_a(\tau)$ and slab trajectories $z_a(\tau)$ corresponding to this case are displayed in Fig. 2.2. At each intersection of slab trajectories, constant chromofield changes sign, and initial conditions are recalculated. Each instant of collision of two slabs corresponds to their maximum rapidities. This can be easily seen in behavior of trajectories and rapidities of two identical slabs (Fig. 2.2a,b). In this case laboratory time coincides with the proper time, $t_1 = \tau_1$. In an asymmetric collisions (Figs. 2.2c,d) energy loss of the smaller projectile slab is larger than energy loss of the target slab. After second collision the projectile slab reaccelerates again and gains kinetic energy larger than the initial one. Deceleration and reaccelaration of target slab is smaller due to its larger mass. This periodic motion states a challenge for the numerical simulations. Sufficient accuracy to find initial conditions at each intersection point was achieved only by increasing the number of nodes in Chebyshev interpolation from 40 to 60. It is seen that constant chromofield leads to the "yo-yo" type motion of baryonic slabs with the period strongly dependent on the initial slab rapidity and the chromofield energy density. This is in direct analogy with the Lund model for e^+e^- annihilation [45] and other string based models. The principle difference of our approach is that we describe the coherent action of many string-like configurations (2.17).

Let us consider now several more realistic time-dependent fields as discussed in Sect. V:

1. The field evolution motivated by the Schwinger mechanism, Eq. (2.29), is described by $f(x) = (1 + x)^{-4}$, that gives

$$F(x) = \frac{1}{x} \int_0^x \frac{x' dx'}{(1 + x')^4} = \frac{x(3 + x)}{6(1 + x)^3} \ . \tag{2.68}$$

2. The exponential decay, $f(x) = e^{-\gamma x}$ with $\gamma = \Gamma \tau_d = 1$, corresponds to

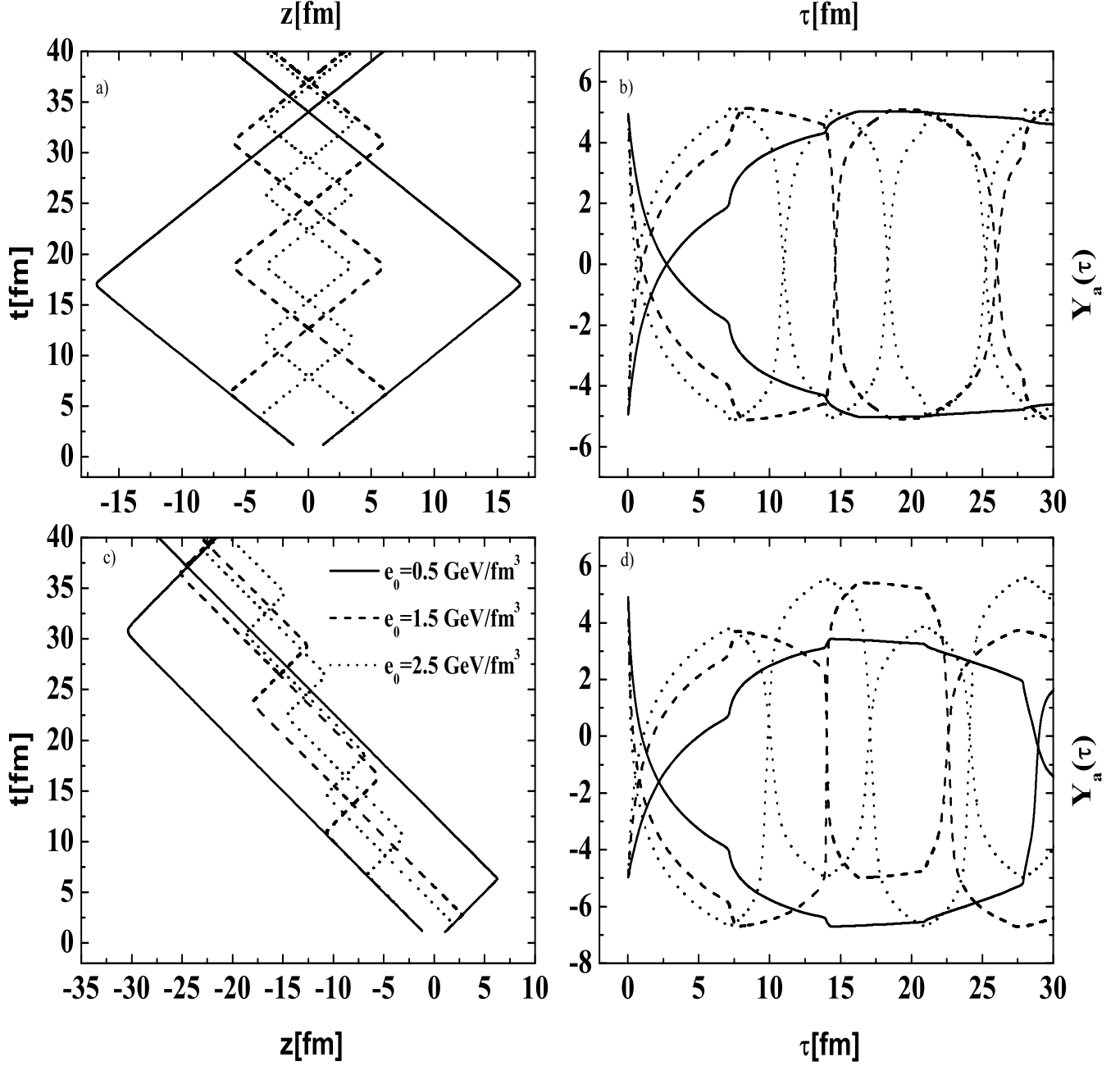$$F(x) = \frac{1}{x} \int_0^x e^{-x'} x' dx' = \frac{1}{x}(1 - e^{-x}) \ . \tag{2.69}$$

Figure 2.2: Projectile and target slab trajectories on $t - z$ plane (left panels), and projectile(upper curves) and target(lower curves) slab rapidities as functions of proper time (right panels) calculated for constant chromofield. Different pairs of curves correspond to various parameters e_0 displayed in the figure. Results are shown for two cases: a),b) equal slabs with $N_p = N_t = 2.58$ representing a central Au+Au collision, and c),d)$N_p = 1.01, N_t = 5.56$ representing peripheral collision.
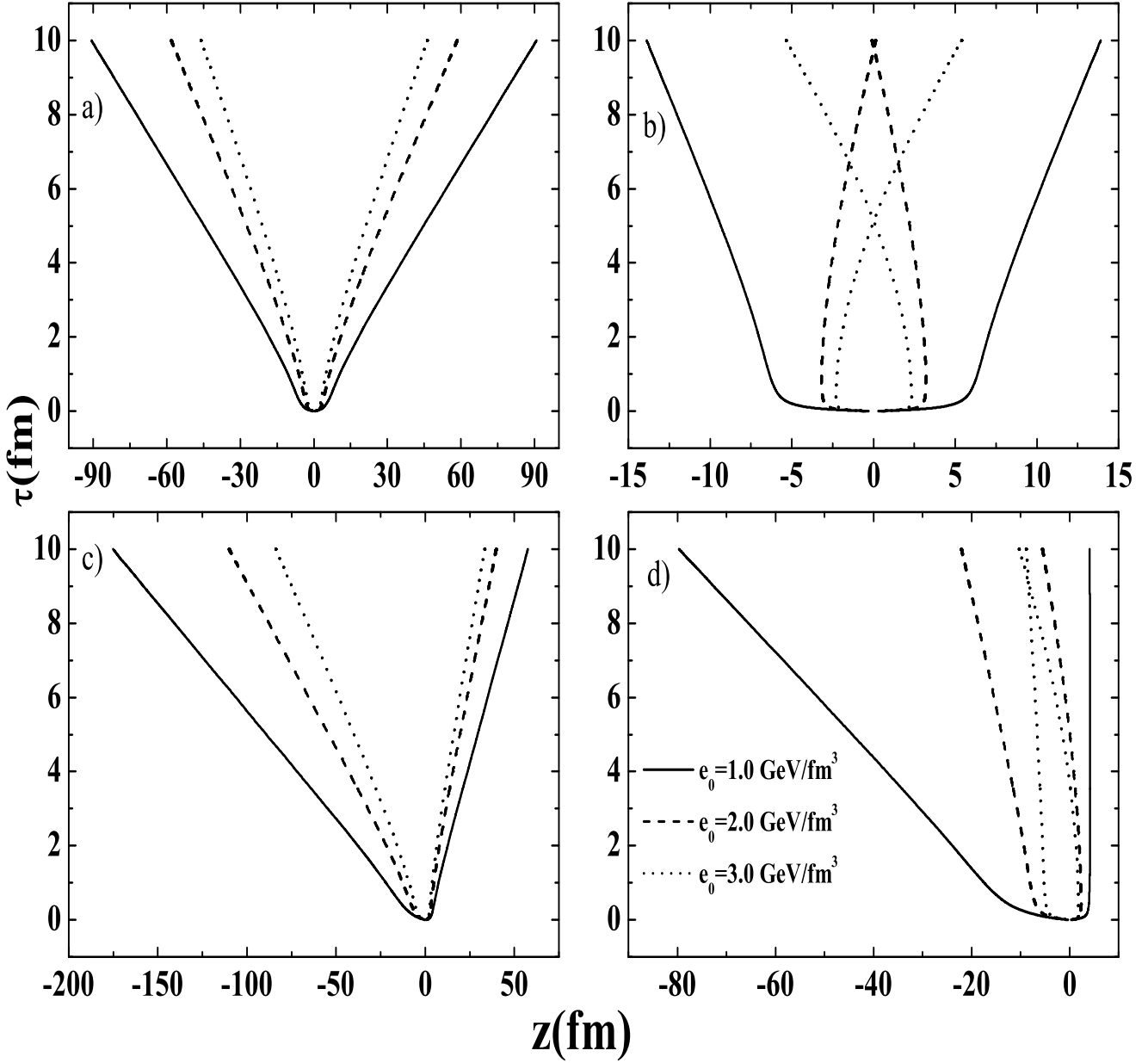
Figure 2.3: Projectile(right curves) and target(left curves) slab trajectories on $z - \tau$ plane calculated for the exponential chromofield decay with $\tau_d = 0.4$ fm. Different pairs of curves correspond to the different parameters ϵ_0 displayed in the figure. Results are shown for two cases: a),b) equal slabs with $N_p = N_t = 5.8$ representing a central Au+Au collision, and c),d) $N_p = 2.0, N_t = 8.8$ representing a central d+Au collision. Left and right panels show the calculations with and without the back reaction of produced plasma, respectively.
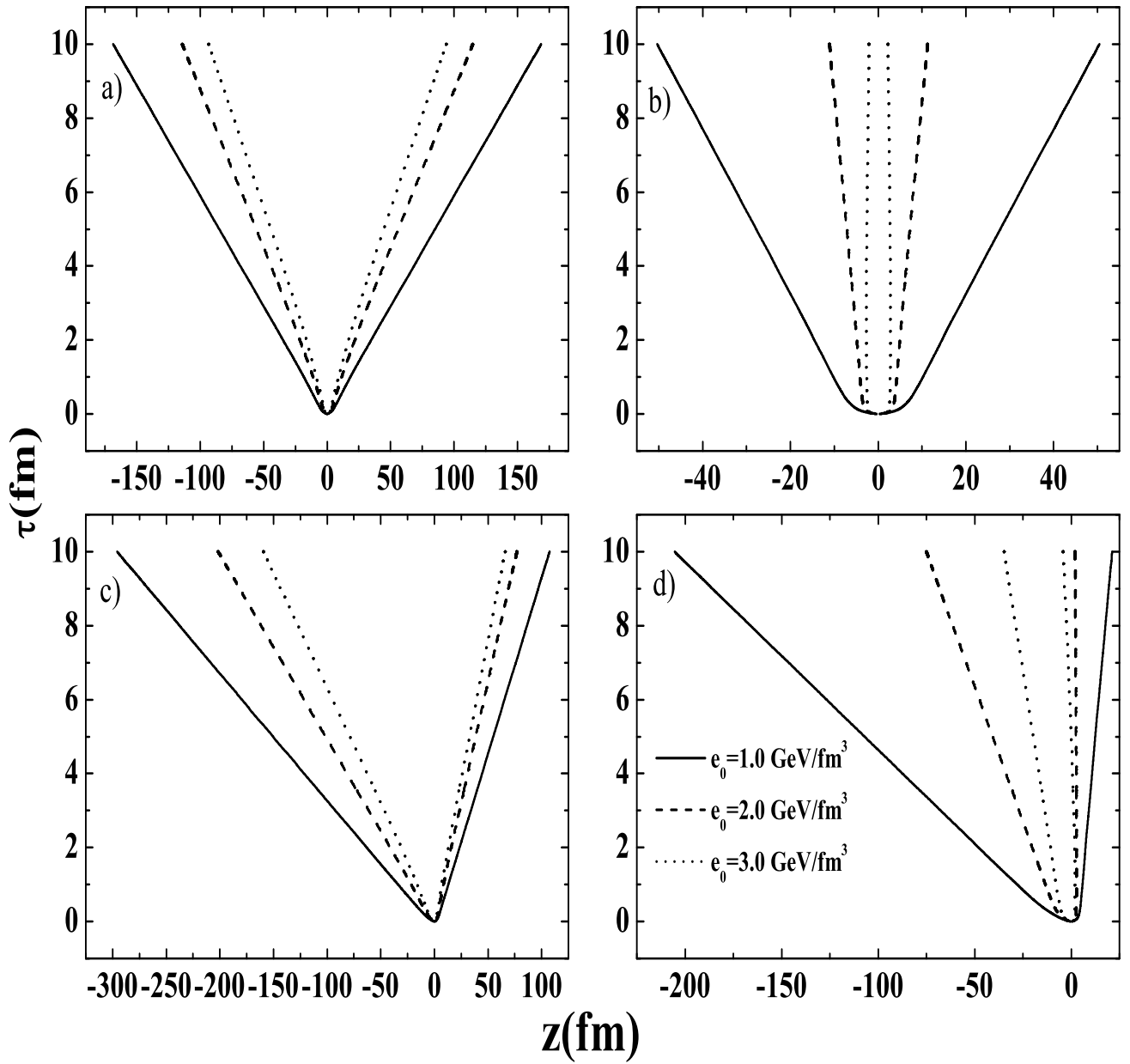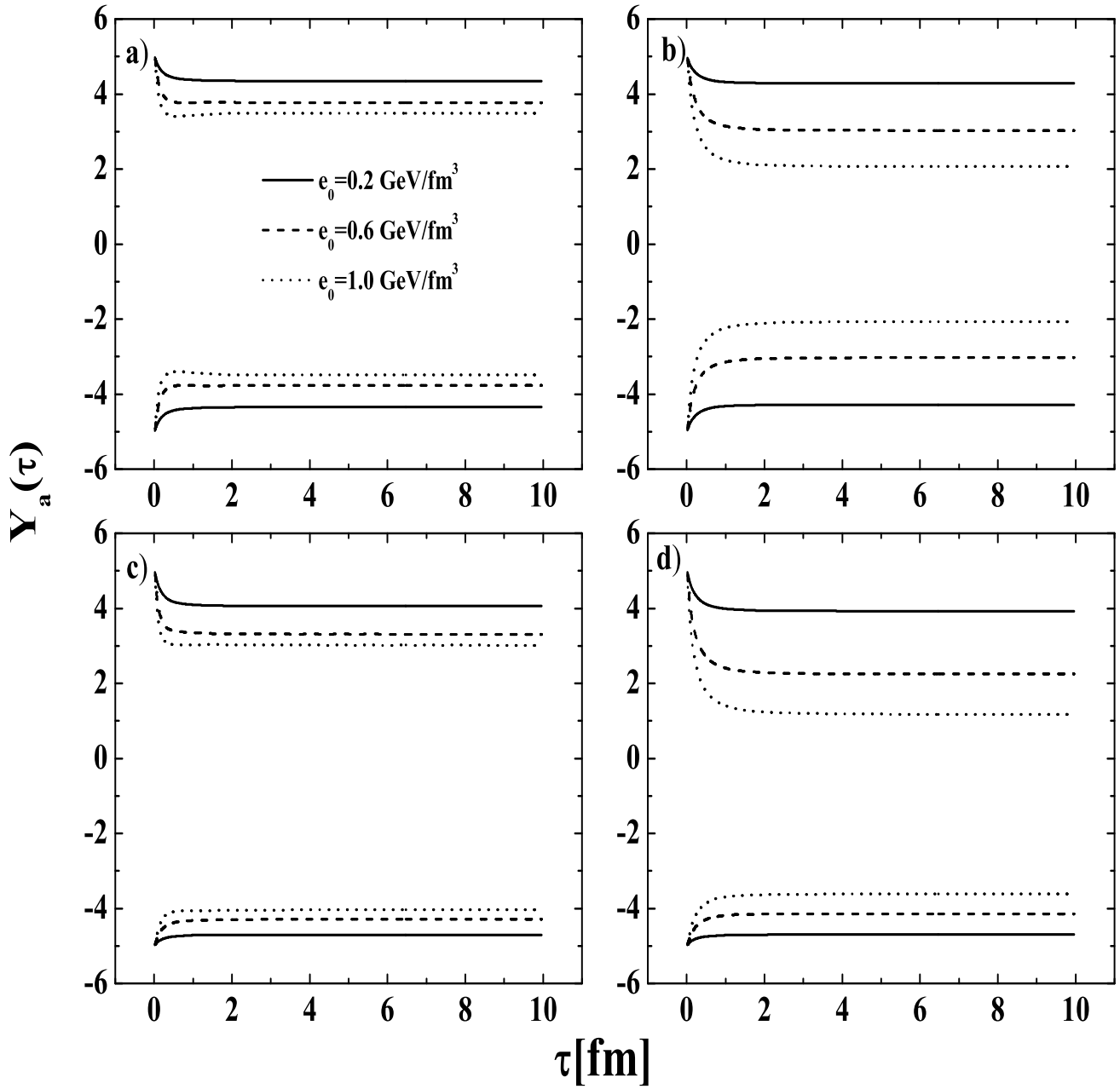
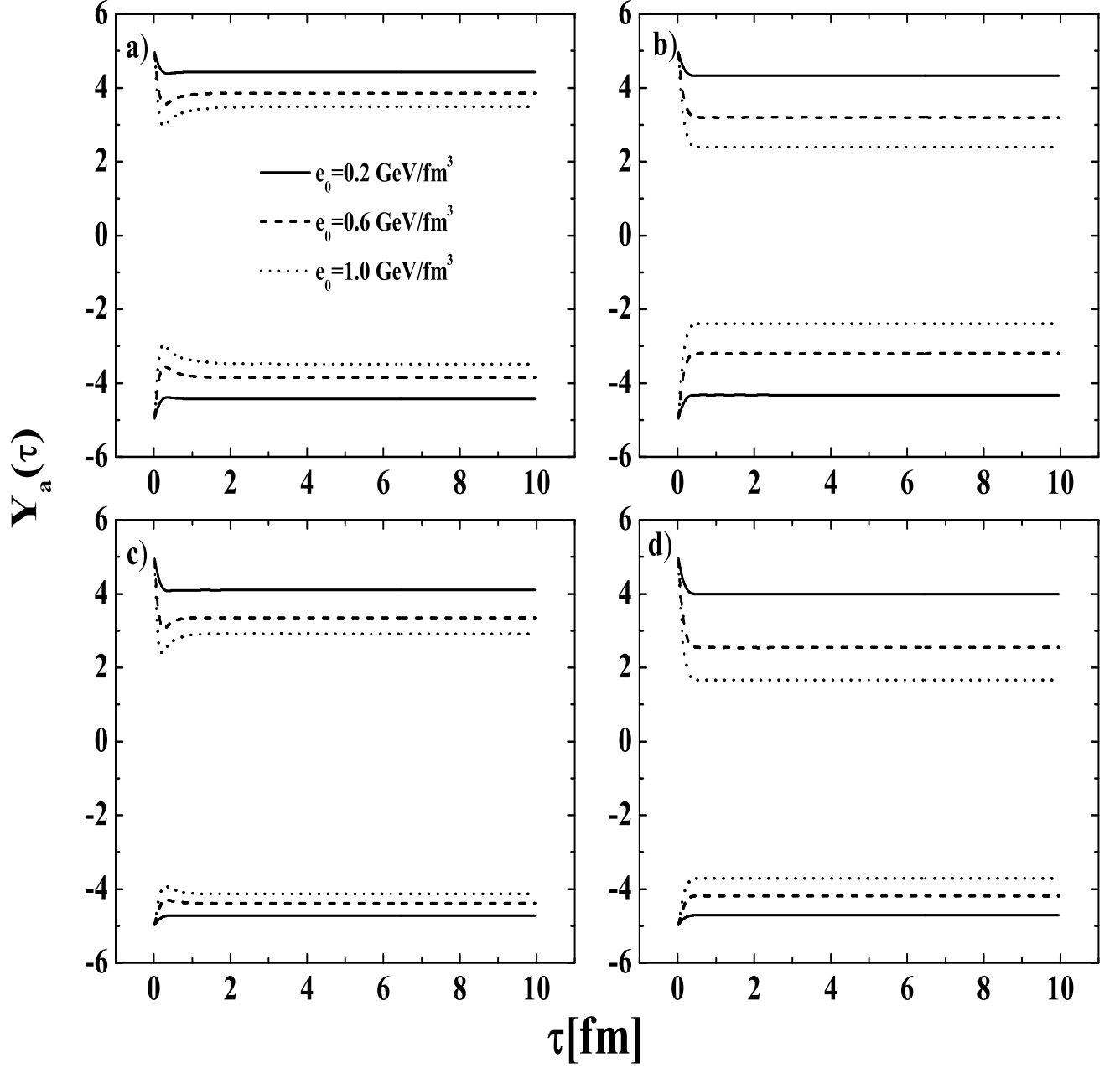Figure 2.4: The same as Fig. 2.6 but for the power-law chromofield decay.
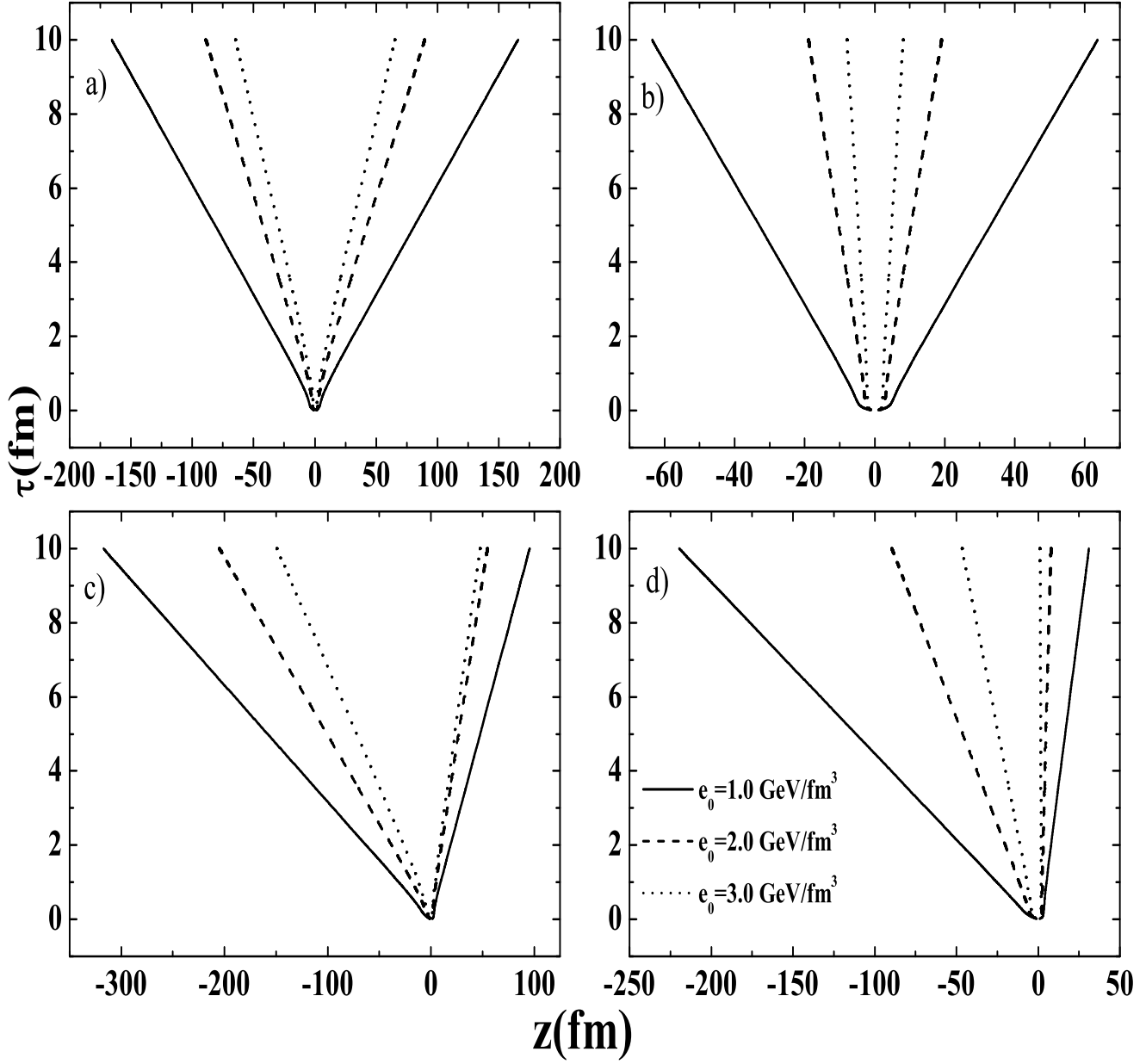
Figure 2.5: The same as Fig. 2.6 but for the CGC decay law of chromofield decay, Eq. (2.34), with $Q_s = 1.2$ GeV.
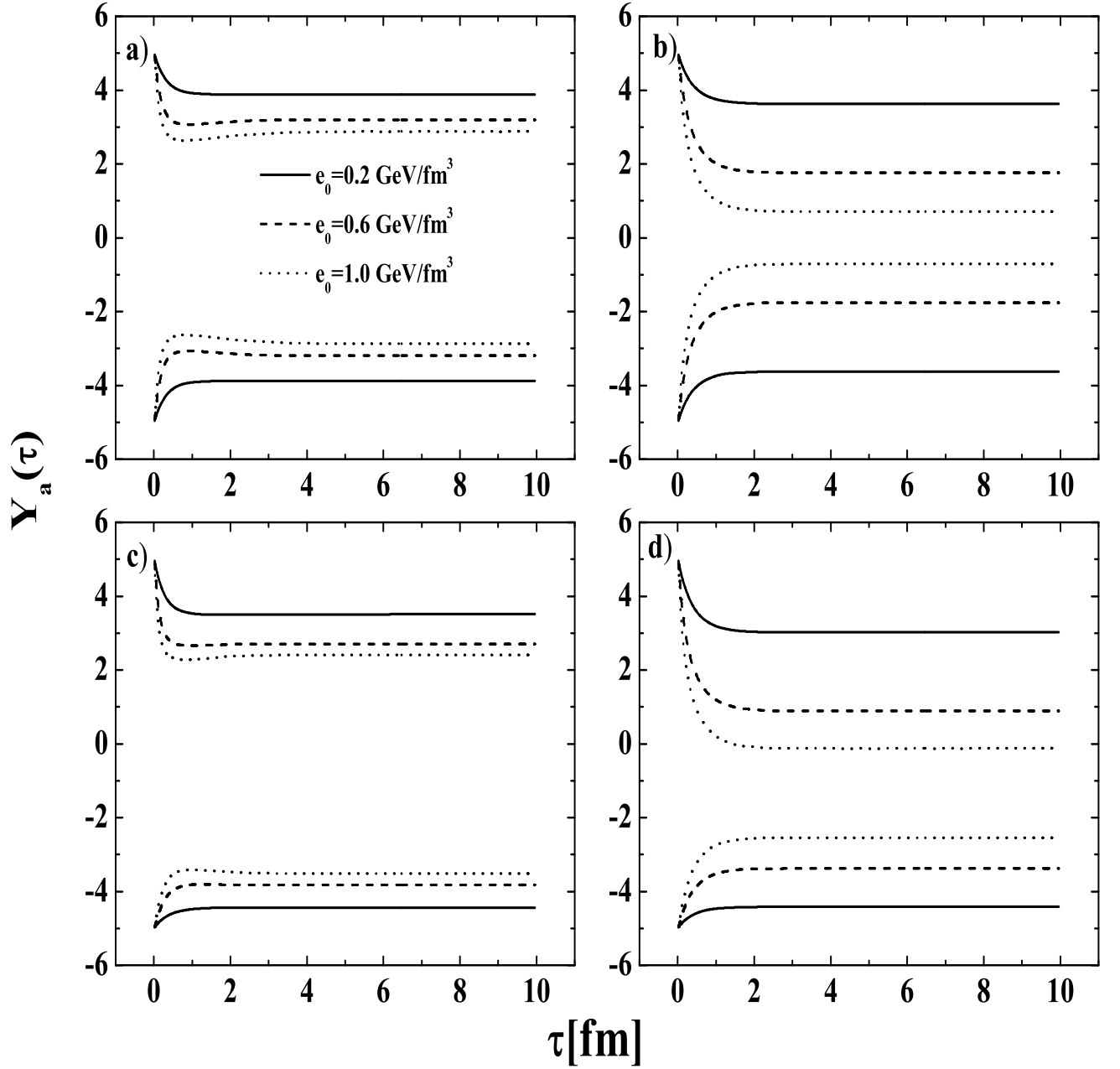
Figure 2.6: Projectile(upper curves) and target(lower curves) slab rapidities as functions of proper time calculated for the exponential law of chromofield decay with $\tau_d = 0.6$ fm. Different pairs of curves correspond to different parameters ϵ_0 displayed in the figure. Results are shown for two cases: a),b) equal slabs with $N_p = N_t = 5.8$ representing a central Au+Au collision, and c),d) $N_p = 2.0$, $N_t = 8.8$ representing a central d+Au collision. Left and right panels show the calculations with and without the back reaction of produced plasma, respectively.

Figure 2.7: The same as Fig. 2.6 but for the power-law of chromofield decay with $\tau_d = 0.6$ fm.

Figure 2.8: The same as Fig. 2.6 but for the CGC decay law of chromofield decay, Eq. (2.34) with $\tau_d = 0.4$ fm.

3. The CGC motivated decay, which leads to sharp disappearance of the field at $\tau_d \approx 2.4/Q_s$, i.e. to $F(x) = const$ at $x > 1$.

In Figs. 2.3-2.5 we show the slab trajectories $z_a(\tau)$ as a function of proper time. It is instructive to compare them with trajectories calculated for the constant field (Fig. 2.2). Due to the fast decay of the chromofield we do not observe generally any traces of the yo-yo motion. Peripheral collisions with large $\epsilon_f(\tau_0)$ and without taking into account plasma back reaction gives the largest deceleration of projectile slab (Fig. 2.6d). The increasing of impact parameter and ϵ_0 will eventually lead to reversal of the slab trajectories and their further collisions. The back reaction of the plasma generates strong push to the slabs. For comparison the distance between colliding slabs with equal baryon number ($N_p = N_t = 5.74$) corresponding to the proper time $\tau = 1.91$ fm for the case with plasma back reaction, is $\Delta z = 64.54$ fm, and for the case when plasma back reaction was not taken into account, is $\Delta z = 25.35$ fm, if $\epsilon_f(\tau_0)$ parameter $\epsilon_0 = 1$ GeV/fm^3 was chosen, and power of chromofield decay was considered. Numerical results for evolution of the collective slab rapidities are presented in Figs. 2.6-2.8. Calculations were performed for the values of parameter ϵ_0 ranging from 0.2 GeV/fm^3 to 1.0 GeV/fm^3 and two values of impact parameter. By comparing left and rights panels one can see in this figures that the slab dynamics is strongly affected by the plasma back reaction. Namely, the plasma back reaction leads to rapid saturation of the baryon rapidity loss with increasing $\epsilon_f(\tau_0)$. It is seen also that the rapidity lost by the smaller slab is significantly larger then the bigger one. This is of course a direct consequence of Newton's law that the equal forces cause larger deceleration for less massive body.

In Fig. 2.9 projectile rapidity loss is displayed as a function of beam rapidity calculated in the wide interval from RHIC to LHC energies at the different parameters ϵ_0. It is seen that strong counter pressure of plasma on slabs leads to slight violation from the linear grows of baryon energy loss with increasing the ϵ_0.

In Fig. 2.10 we show the evolution of the projectile slab energy loss $\Delta\varepsilon_p(\tau)$ per baryon, defined as

$$\Delta E_p(\tau) = (M_0 \cosh Y_0 - M_p(\tau) \cosh Y_p(\tau))/N_p, \qquad (2.70)$$

where M_0 is the initial slab mass and $M_p(\tau)$ is the projectile slab mass calculated by formula (2.58), N_p is the baryon number of projectile slab. The additional slab transverse mass $M_p(\tau)$ is generated entirely due to interaction with produced plasma. To demonstrate the strength of this interaction, in Fig. 2.11 we show the evolution of the baryon transverse momentum. The maximal value of baryon transverse momentum for central collisions is quite
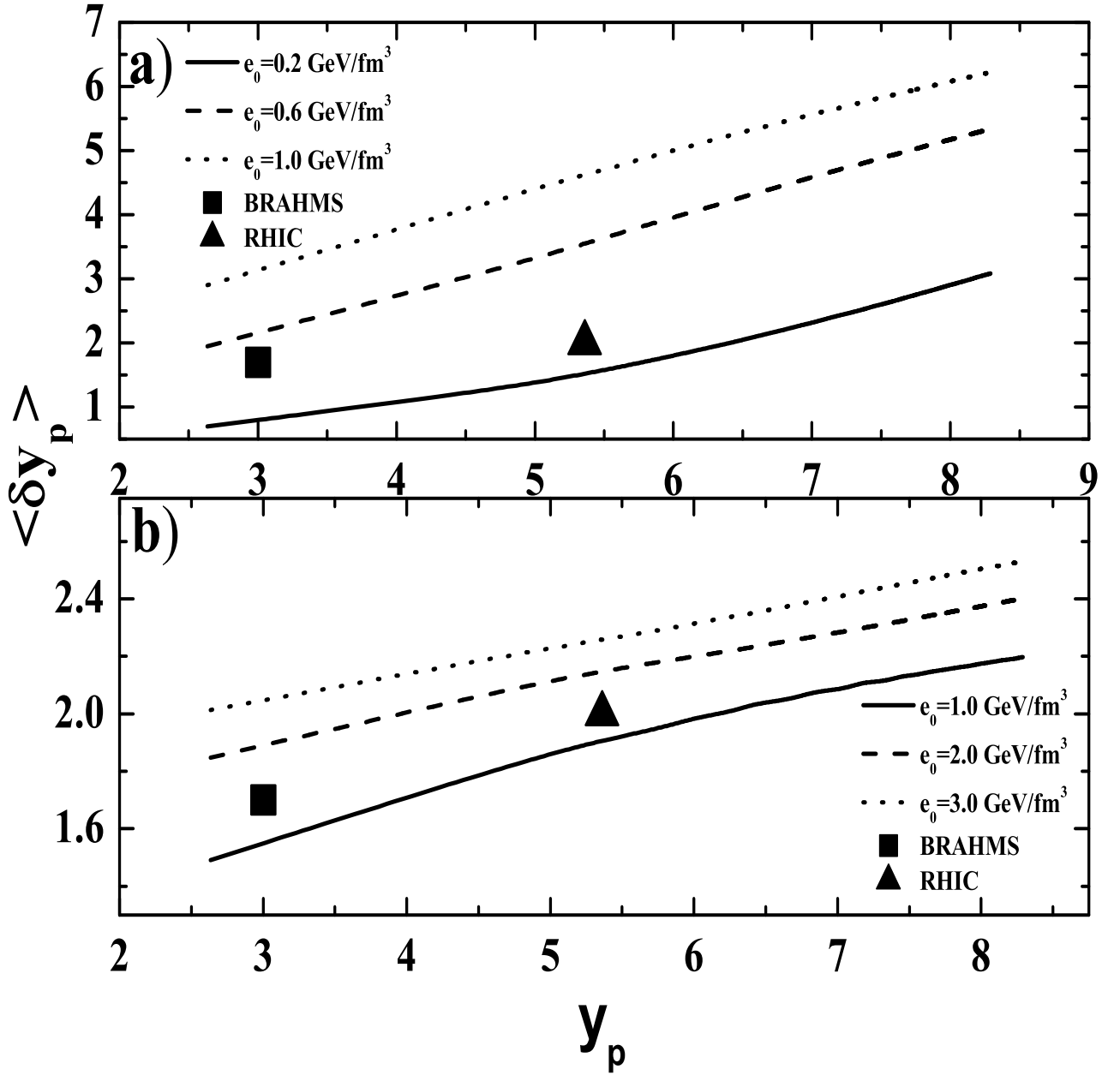
Figure 2.9: Projectile slab rapidity loss as a function of initial beam rapidity calculated for the power-law of chromofield decay. Different curves correspond to the different values of parameter ϵ_0 displayed in the figures. Color charge is assumed fixed. Results are shown for the two cases: a),b) equal slabs with $N_p = N_t = 5.75$ representing a central Au+Au collision, and c),d) $N_p = 2.01, N_t = 7.65$ representing central d+Au collision. Left and right panels show the calculations with and without the back reaction of produced plasma, respectively.
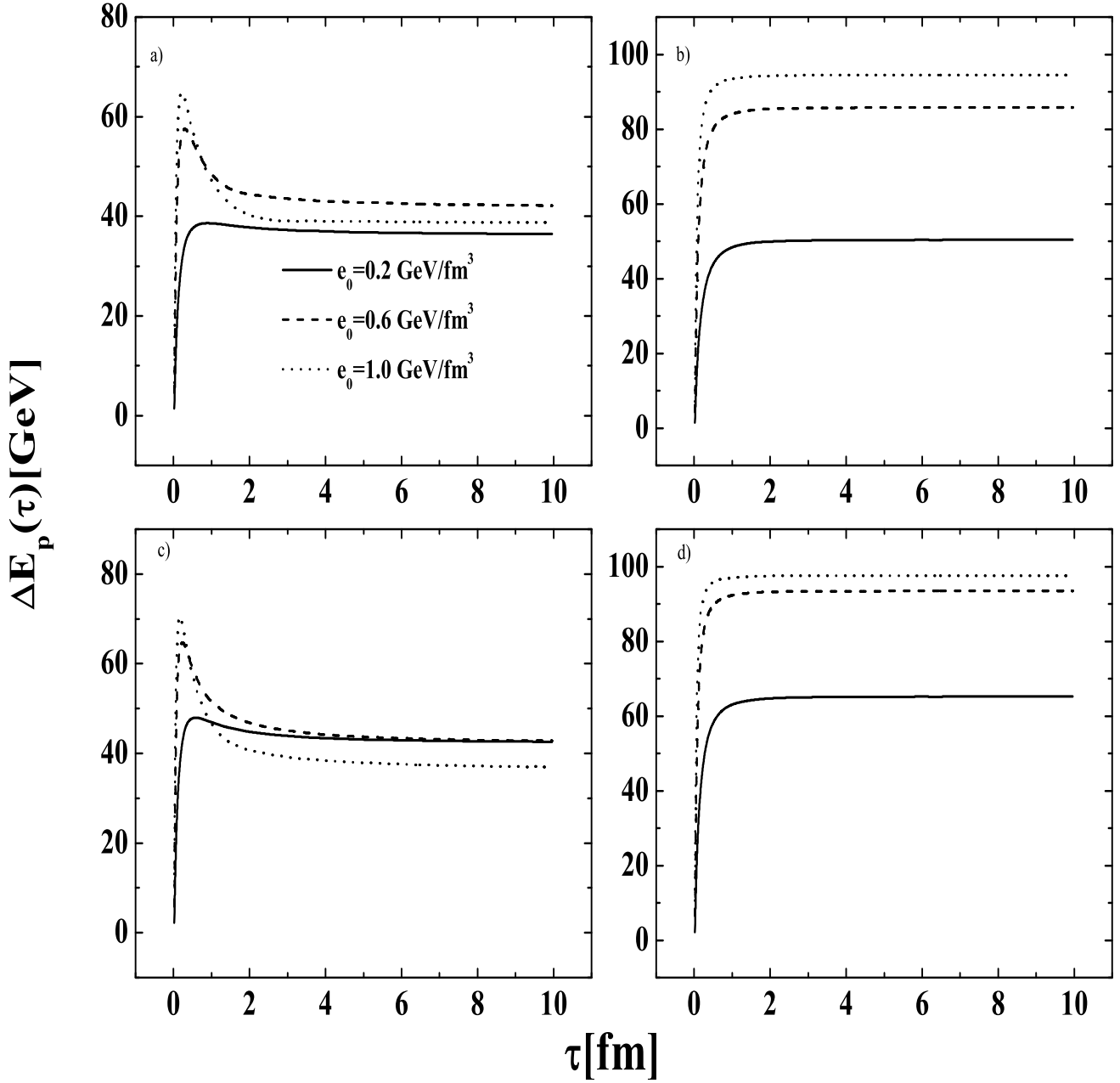
Figure 2.10: Evolution of the baryon energy loss from projectile nucleus calculated for power-law chromofield decay with $\tau_d = 0.6$fm. Different curves correspond to the different values of parameter ϵ_0 displayed in the figures. Results are shown for the two cases: a),b) equal slabs with $N_p = N_t = 5.75$ representing a central Au+Au collision, and c),d) $N_p = 2.01, N_t = 7.65$ representing central d+Au collision. Left and right panels show the calculations with and without the back reaction of produced plasma, respectively.
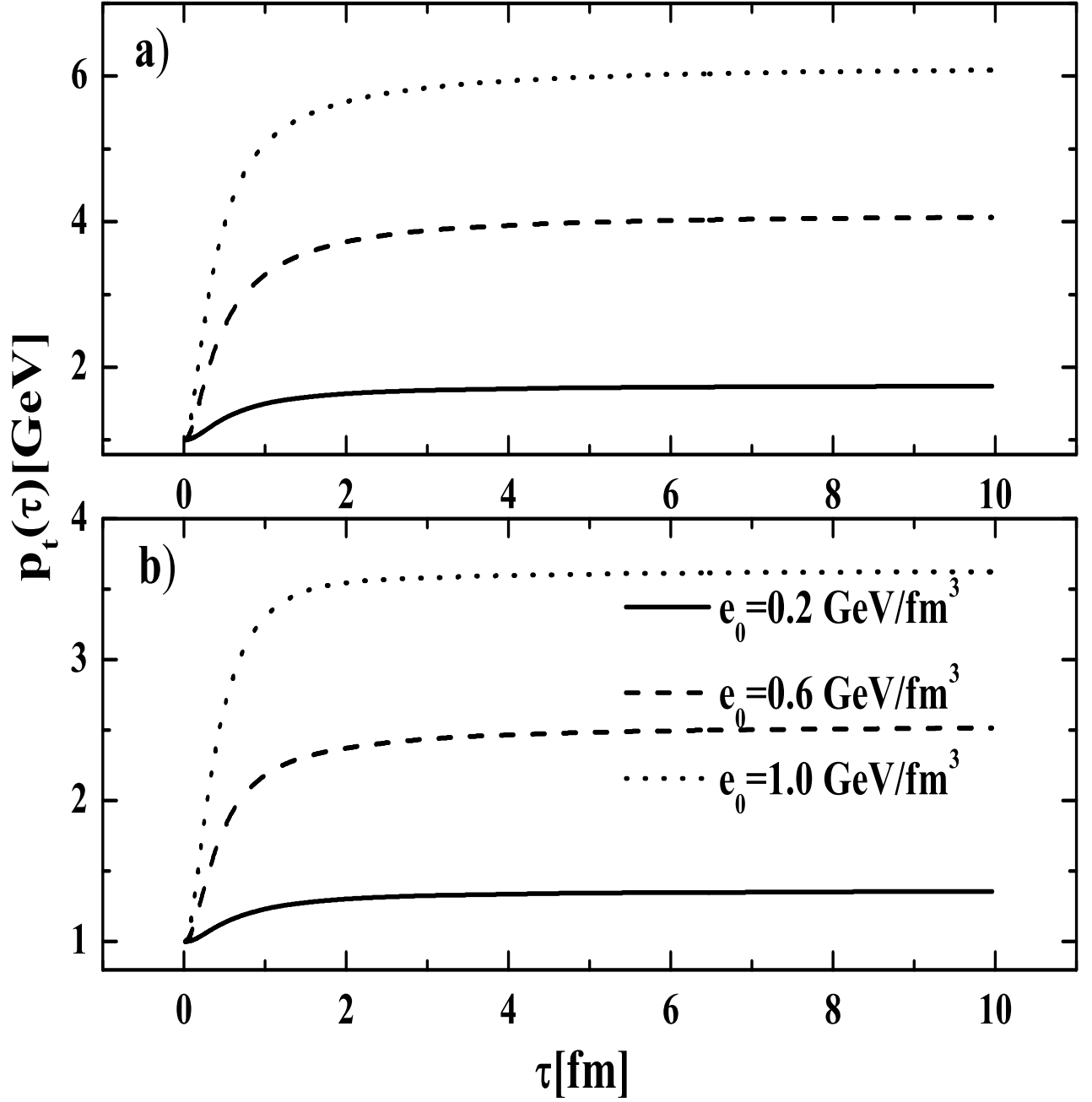
Figure 2.11: Evolution of the baryon transverse momentum calculated for power law of chromofield decay at different parameters ϵ_0 indicated in the figure. Results are shown for two cases: a) $N_p = 2.01$, $N_t = 7.65$ representing central d+Au collisions, and b) $N_p = N_t = 5.75$ representing central Au+Au collisions.

large: $\langle p_\perp \rangle = 3.5$ GeV. In our model we can only allow the final $\langle p_\perp \rangle$ value, which agree with the observed ones, $\langle p_\perp \rangle \approx 1$ GeV, [93]. To obtain such low value of baryon transverse momentum one has to take into account partial transparency of slabs with respect to the produced plasma. This can be implemented by assuming that plasma is created not uniformly on the whole hypersurface $\tau = const$, but only on the part of it which sufficiently far from the ends (edge effect). Thus, in a more realistic calculation, dependence of the plasma energy density on pseudorapidity should be explicitly taken into account. When the plasma back reaction is disregarded, the slab mass remains constant in the course of evolution. Therefore, we should assume that the observed value of the baryon transverse momentum was generated already at very early stage of the collisions, i.e. at $\tau \sim \tau_0$. Then the initial slab rapidities should also be shifted from y_0 to $y_0 = Arcosh\frac{\sqrt{s}}{2m_\perp}$. From Fig. 2.10 one can see that the 70% energy loss observed by the BRAHMS collaboration for central $Au + Au$ collisions at $\sqrt{s} = 200$ AGeV can be explained by the action of the chromofield with the energy density of about 20 GeV/fm^3 ($\epsilon_0 \simeq 0.5$ GeV/fm^3).

2.7.3 Partonic wind

In this subsection we address the question, how the baryon slab trajectories are affected by the collective partonic flux from the central region. The calculations can be done analytically for a step-like evolution of the chromofield, $\epsilon_f(\tau) = \epsilon_f(\tau_0)\theta(\tau_d - \tau)$. In this case the partonic plasma is produced at a fixed proper time $\tau = \tau_d$, exactly as postulated in the Bjorken model [13]. An interesting observation for this case is that predictions can be made without knowledge of equation of state. According to Eqs.(2.42) and (2.49), the pressure, energy density and enthalpy density of partonic plasma at later times ($\tau > \tau_d$) evolve as

$$p(\tau) = c_s^2 \epsilon(\tau) = c_s^2 \epsilon_f(\tau_0) \left(\frac{\tau_d}{\tau}\right)^{1+c_s^2} \; , \; A(\tau) = (1 + c_s^2)\epsilon_f(\tau_0) \left(\frac{\tau_d}{\tau}\right)^{1+c_s^2} \quad (2.71)$$

where c_s^2 is the constant sound velocity. From Eq. (2.57) we find that due to the action of the chromofield at $\tau < \tau_d$ the slab momentum decreases on the value $\tilde{P}(\tau_d) - \tilde{P}(0) = -\epsilon_f(\tau_0)\tau_d/2$. The additional momentum change due to the partonic wind at $\tau > \tau_d$ is found from Eq. (2.57) with $B(\tau) = -p(\tau)$:

$$\tilde{P}(\tau) - \tilde{P}(\tau_d) = -\frac{\epsilon_0 \tau_d^2}{2\tau} - \epsilon_0 \tau_d \left(\frac{c_s^2}{1 - c_s^2}\right) \left[\left(\frac{\tau_d}{\tau}\right)^{c_s^2} - \left(\frac{\tau_d}{\tau}\right)\right] \; . \quad (2.72)$$

According to Eq. (2.58) with $A(\tau)$ from Eq. (2.71), the additional slab

mass squared due to plasma absorption is given by

$$M^2(\tau) - M^2(\tau_0) = -\frac{\epsilon_0^2 \tau_d^2}{1 - c_s^2} \left(\frac{1 - 3c_s^2}{x^{1+c_s^2}} + \frac{1 + c_s^2}{x^{2c_s^2}} + 2(c_s^2 - 1) \right) \Bigg|_1^{\frac{\tau}{\tau_d}}, \quad (2.73)$$

where $x = \frac{\tau}{\tau_d}$ is a new variable. Asymptotically at $\tau \to \infty$ dependence on the sound velocity in the relative mass squared increment drops out

$$\frac{M^2 - M_0^2}{M_0^2} = 2\alpha^2 \qquad (2.74)$$

Parameter α was introduced in Eq. (2.64). Let us take $\epsilon_0 = 1.0$ GeV/fm^3, which according to Eq. (2.25) corresponds to average energy density for central $Au + Au$ collisions $\epsilon_f(\tau_0) = 30.65$ GeV/fm^3. The initial mass per unit area of the central slab is $M(\tau_0) = 2.89$ 1/fm^3. Characteristic time of chromofield decay was chosen as $\tau_d = 0.6$ fm. For this values parameter α is estimated as $\alpha = 6$. This eventually leads to the increasing of the slab mass in ~ 8.5 times, which is obviously unrealistic.

2.8   Net-baryon rapidity spectra

In this section we study the net-baryon rapidity distributions under different hypotheses concerning the chromofield decay and plasma back reaction. Our basic assumption is, that the baryon-rich matetr of slabs consists of nearly massless quarks, antiquarks and also gluons. For simplicity we also assume that that the kinetic equilibrium is established within individual slabs. The Parton Cascade Model(PCM) simulations for RHIC energies indicate that the momentum distributions of produced gluons become isotropic and Boltzmann-like at proper times of about $1-2$ fm [56]. On the other hand, simulations within the QGSM give similar times for achieving isentropic regime even at lower energies of SPS for Pb+Pb collisions [37, 82].

A simple analytival expression for the net-baryon rapidity density can be obtained within thermal model by applying the Cooper-Frye prescription [84]:

$$\frac{dN_{B-\bar{B}}}{dy} = \sum_{a=p,t} \int_{\Sigma} p^\mu d\Sigma_\mu S_a(\tau, \eta) \int d^2\mathbf{p}_\perp \mathcal{F}_a, \qquad (2.75)$$

where Σ is a $4-$dimensional hypersurface on which the distribution of particles is calculated. The function $S_a(\tau, \eta)$ describes the distribution of emitting sources in τ, η space. The baryon momentum distribution function in slab a

is taken in the standard form

$$\mathcal{F}_a = \frac{\nu_q}{3(2\pi)^3} \left[\frac{1}{\exp(\frac{(p^\mu u_\mu)^a - \mu^a}{T^a}) + 1} - \frac{1}{\exp(\frac{(p^\mu u_\mu)^a + \mu^a}{T^a}) + 1} \right] f_a(\tau, \eta), \quad (2.76)$$

where ν_q is the quark (antiquark) degeneracy factor given in Eq. (2.28). It is easy to see that $(p^\mu u_\mu)^a = m_\perp \cosh(y - Y_a)$ is the quark energy in the laboratory frame, where

$$u_a^\mu = (\cosh Y_a, \mathbf{0}, \sinh Y_a) \quad (2.77)$$

is the collective velocity of slab $a = p, t$, and

$$p^\mu = m_\perp (\cosh y, \mathbf{0}, \sinh y) \quad (2.78)$$

is the quark 4-momentum. For the case of massless quarks ($m_\perp = p_\perp$) the $p_\perp$ integration in Eq. (2.75) can be done analytically,

$$\int p_\perp d^2\mathbf{p}_\perp \mathcal{F}_a = \frac{n_B}{2 \cosh^3(y - Y_a)} \quad (2.79)$$

where the net-baryon number density carried by quarks is

$$n_B = \frac{\nu_q}{18\pi^2} (\mu^3 + \pi^2 T^2 \mu) \quad (2.80)$$

We used a standard parameterization of the hypersurface Σ in terms of τ and η coordinates such that

$$p^\mu d\Sigma_\mu = m_\perp [d\eta \tau \cosh(y - \eta) - d\tau \sinh(y - \eta)] d^2\mathbf{s} \quad (2.81)$$

Since we neglect the slab expansion the functional form of the source function $S_a(\tau, \eta)$ is only constrained by the slab trajectories $z = z_a(\tau)$ or $\eta = \eta_a(\tau)$, i.e.

$$S_a(\tau, \eta) = C_a \delta(\eta - \eta_a(\tau)) \quad (2.82)$$

Factor C_a is found from the normalization condition

$$\int dy \frac{dN}{dy} = N_{part}(\mathbf{b}) \quad (2.83)$$

where $N_{part}(\mathbf{b})$ is the number of participants given by Eq. (2.3). For each individual slab in the nucleus a it takes the following form

$$C_a = \frac{N_a(\mathbf{b}, \mathbf{s})}{n_B \tau \cosh(Y_a(\tau) - \eta_a(\tau))} \quad (2.84)$$

Since we shall perform all further calculations at some fixed proper time, $\tau = const$, contribution of the second term in Eq. (2.81) vanishes. The integration on η for the given form of $S_a(\tau, \eta)$ is trivial:

$$\frac{dN_{B-\bar{B}}}{dy} = \int d^2\mathbf{s} \sum_{a=p,t} \frac{\tilde{N}_a \cosh(y - \eta_a(\tau))}{2\cosh^3(y - Y_a(\tau))\cosh(Y_a(\tau) - \eta_a(\tau))}. \qquad (2.85)$$

In accordance with Eq. (2.57), $\lim_{\tau\to\infty}(Y_a(\tau) - \eta_a(\tau)) = 0$. Therefore, at times $\tau \gg \tau_d$ the net-baryon rapidity distribution is expressed as:

$$\frac{dN_{B-\bar{B}}}{dy} = \int d^2\mathbf{s} \sum_{a=p,t} \frac{\tilde{N}_a(\mathbf{b}, \mathbf{s})}{2\cosh^2(y - Y_a(\tau))}. \qquad (2.86)$$

In the case, when color charge is treated as a random variable, net-baryon rapidity density should be averaged over the random color field distribution given by Eq. (2.22),

$$\left\langle \frac{dN_{B-\bar{B}}}{dy} \right\rangle = \int \frac{dN_{B-\bar{B}}(F)}{dy} w(F) dF \qquad (2.87)$$

The net-baryon rapidity spectra calculated for different centralities and various chromofield decay patterns are shown in the Figs. 2.12-2.14. Averaging over impact parameters was performed within the Glauber model, according to the number of participants Eq. (2.3), in different centrality bins. Left and right panels present results with and without the back reaction of the partonic plasma. One can clearly see that the plasma back reaction is too strong, so that net-baryons are swept from the central rapidity region. When plasma back reaction is disregarded, the mid-rapidity region can be filled easily by proper choice of parameter ϵ_0, introduced in Eq. (2.25).

Comparison of two cases, when the color charge is treated as fixed or random quantity, shows that the field fluctuations contribute to filling the mid-rapidity region. However, as one can see from Table 2.1, this effect is rather small, and it is not sufficient to reproduce a rather flat shape of net-baryon rapidity distributions at ($|y| \lesssim 2$). The increase of net-baryon content at mid-rapidities is explained by the fact that the color field distribution (2.22) has a long tail at large fields, but their contributions are strongly suppressed by the exponential weight. This improvement of the model is still not enough to fit the data simultaneously at mid-rapidity and in fragmentation regions by varying only one parameter ϵ_0. The mid-rapidity region is better described by larger values of ϵ_0, but the fragmentation region, by smaller ϵ_0.
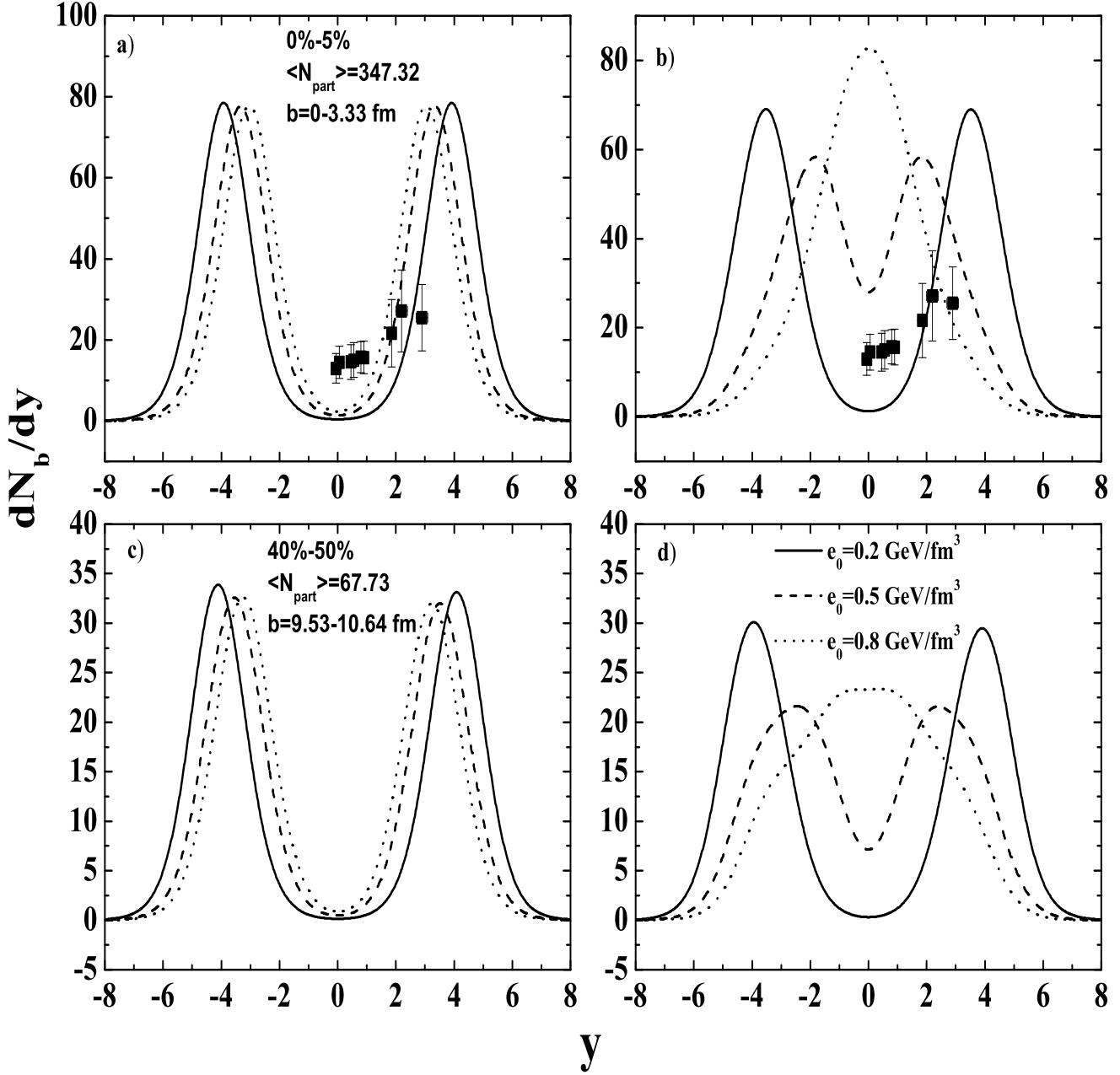
Figure 2.12: Net-baryon rapidity distributions for Au+Au collisions at $\sqrt{s_{NN}} = 200$ AGeV calculated for different centralities and different parameters ϵ_0 of $\epsilon_f(\tau_0)$, which are displayed in the figure. Exponential law of chromofield decay was chosen. Calculations with back reaction of produced partonic plasma on slab dynamics are displayed in the panels a),c), and without back reaction in the panels b),d). Fluctuations of the chromofield are taken into account by averaging of results over the gamma-distribution of chromofield energy density (2.22). Calculations were stopped at $\tau = 10$ fm.
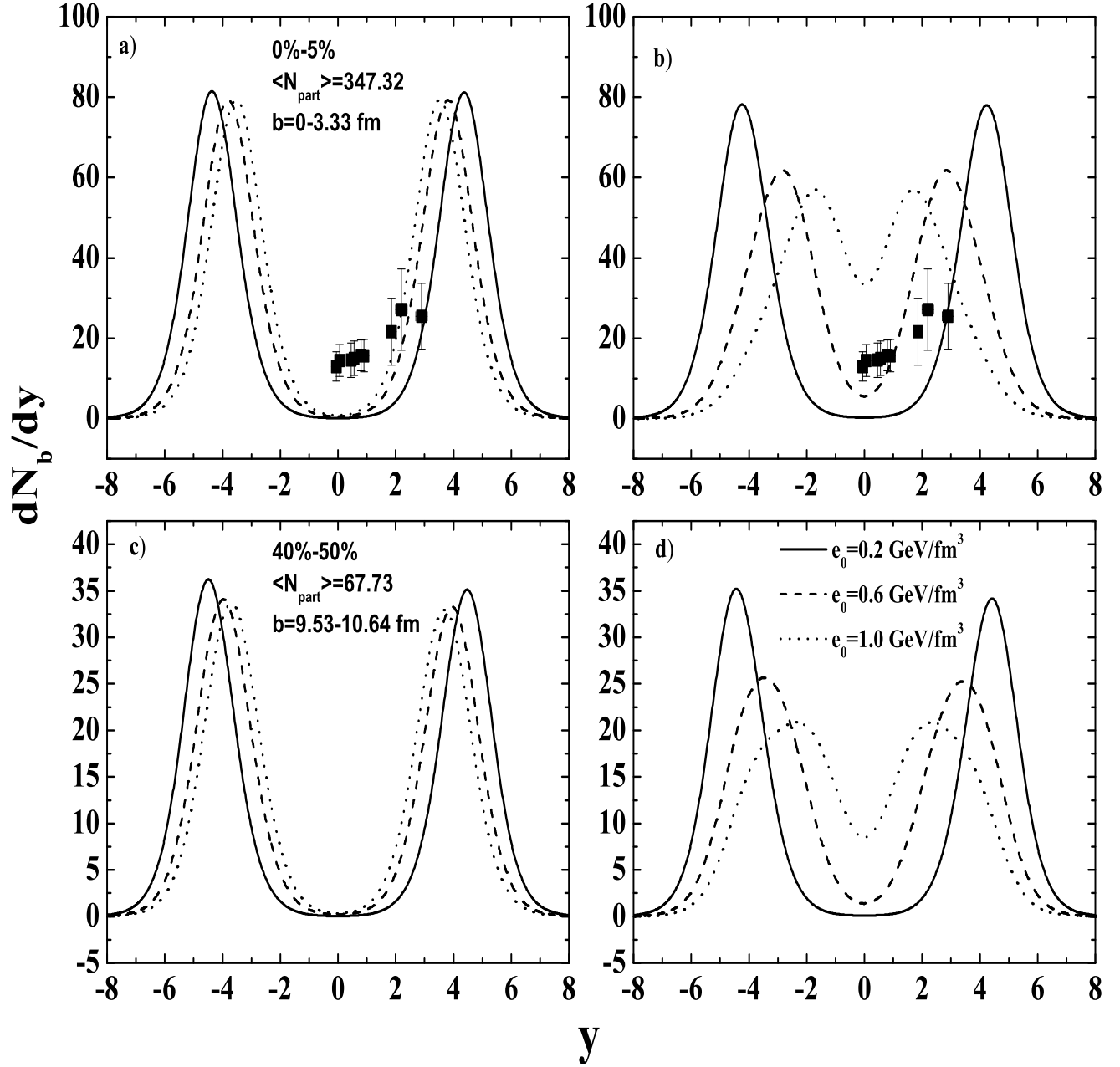
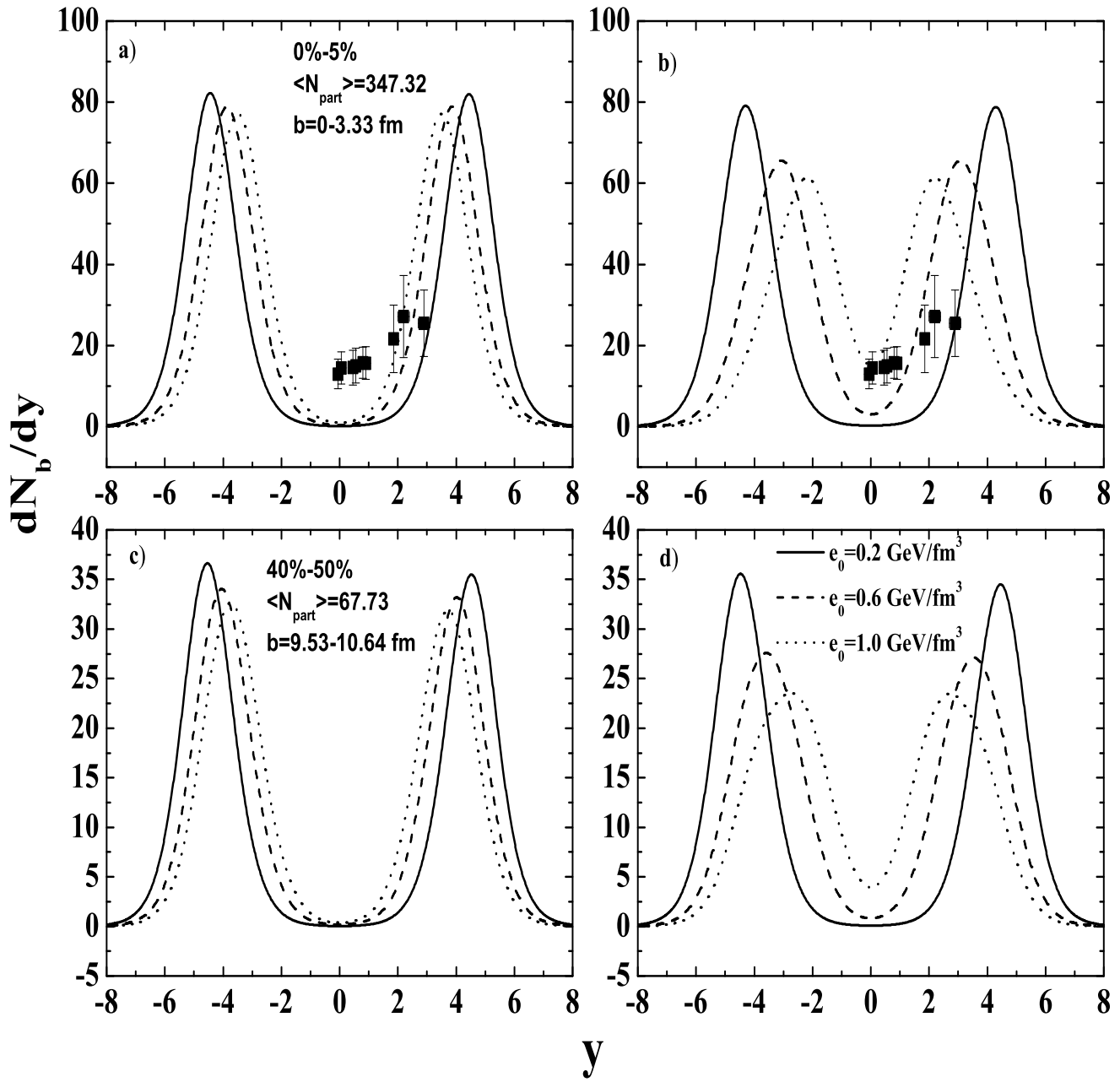Figure 2.13: The same as Fig. 2.12 but for power-law of chromofield decay.

Figure 2.14: The same as Fig. 2.12 but for the CGC-law of chromofield decay.

y	$\frac{dN_{B-\bar{B}}^{fix}}{dy}$		$\frac{dN_{B-\bar{B}}^{fluc}}{dy}$
2.77	69.6		64.7
2.17	59.26		53.28
1.56	30.85		30.29
0.94	11.42		12.64
0.31	4.42		5.25

Table 2.1: Comparative table for net-baryon spectra calculated for power law of chromofield decay in the central rapidity region with $\frac{dN_{B-\bar{B}}^{fluc}}{dy}$ and without $\frac{dN_{B-\bar{B}}^{fix}}{dy}$ taking into account color charge fluctuations. Corresponding initial chromofield field energy density is $\epsilon_f(\tau_0) = 48$ GeV/fm^3

For example, calculations for exponential chromofield decay (Fig. 2.12) give even lower values of $\epsilon_f(\tau_0)$, 32 GeV/fm^3 and 8 GeV/fm^3 for mid-rapidity and fragmentation region respectively. Results for power law (Fig. 2.13) are between this two cases: 50 GeV/fm^3 and 17 GeV/fm^3 respectively. Within the CGC model we need $\epsilon_f \approx 78$ GeV/fm^3 to better describe the mid-rapidity region, while $\epsilon_f \approx 16$ GeV/fm^3 to better describe the fragmentation region (see Fig. 2.14). Calculations within the MV model give $\epsilon_f(\tau_0)$ values intermediate between fragmentation and mid-rapidity regions $\epsilon_f(\tau_0) = 37.87$ GeV/fm^3. In this estimate we have used $Q_s^2 \approx 1.44$ GeV^2 used in Ref. [27] for the RHIC energy, and explicit expression,

$$\mu^2 = g_s^2(Q_s^2)N_a \left(N_c + \frac{1}{2} \right) \qquad (2.88)$$

obtained in Ref. [32]. By applying χ^2-criterion we conclude that the power-law of chromofield decay is the best of three to fit the experimental data. These results indicate that the geometrical factor N_{coll} in Eq. (2.25) is not sufficient to describe the difference of chromofields generated in the mid-rapidity and fragmentation regions, and because of that one should explicitly introduce the η- dependence of the chromofield.

In the rest of this section we present our estimates for the temperature and baryon density, which can be achieved in the baryonic slabs. They can be found in the following way. By assuming that baryon-rich plasma is an ideal gas of massless partons, the energy density can be expressed through the temperature T and baryon chemical potential μ [75],

$$\varepsilon = \frac{\pi^2}{15} \left(N_c^2 - 1 + \frac{7N_c N_f}{4} \right) T^4 + \frac{N_c N_f}{2} \left(T^2 \mu^2 + \frac{\mu^4}{2\pi^2} \right) + B \qquad (2.89)$$

Due to smallness of the vacuum energy density B compared to other terms in Eq. (2.89), it can be safely omitted. Usng the corresponding expression for the baryon density, Eq. (2.80) we can express the mean energy per baryon, $\epsilon_B = \frac{\varepsilon}{n}$, as: $\epsilon_B = Tf(z)$, where $z = \frac{\mu}{T}$, and

$$f(z) = \frac{a_1 + a_2 z^2 + a_3 z^4}{b_1 z^3 + b_2 z}. \tag{2.90}$$

This function is shown in Fig. 2.15. To get an idea about T and μ let us consider condition of minimum energy per baryon. At given T this corresponds to the minimum of $f(z)$, corresponding to $z_{min} = 1.8$ and $f_{min} = 15$

From the values z_{min}, f_{min}, and at given energy per baryon $\epsilon_B = \frac{M(\tau)}{N_a}$ obtained from our dynamical calculations, one can find the maximum temperature and corresponding chemical potential:

$$T_{max} = \frac{\epsilon_B}{f_{min}}, \quad \mu_{max} = z_{min}T_{max} \tag{2.91}$$

Maximal temperature and baryon density in calculations with plasma back reaction are unrealistically large, while in calculations without plasma back reaction they are more reasonable: $n = 0.59\text{fm}^{-3}$, and $T = 100$ MeV. This shows that baryonic slabs are composed of very dense and relatively cold quark-gluon plasma, which is expected to have first-order phase transition to hadronic phase [126].

2.9 Parton rapidity spectra

To calculate the parton rapidity distributions we also use the Cooper-Frye prescription, Eq. (2.75), discussed in the previous section. Integration on transverse momentum of Bose-Einstein and Fermi-Dirac distributions is easily done by changing variable $x \rightarrow p_\perp \cosh(y - \eta)$ that leads to the standard integrals

$$\int\limits_0^\infty dp_\perp p_\perp^2 \left\{ \exp\left(\frac{p_\perp \cosh(y - \eta)}{T}\right) \mp 1 \right\}^{-1} = \frac{T^3 \zeta(3)}{\cosh^3(y - \eta)} \times \begin{cases} 2, \text{ gluons} \\ \frac{3}{2}, \text{ quarks} \end{cases}$$
$$\tag{2.92}$$

The energy density of ideal massless plasma is described by the Stefan-Boltzmann law

$$\epsilon(\tau) = \sigma_{SB} T^4 \tag{2.93}$$

where $\sigma_{SB} = \frac{\pi^2}{30}(\nu_g + \frac{7}{4}\nu_q)$. The corresponding entropy is

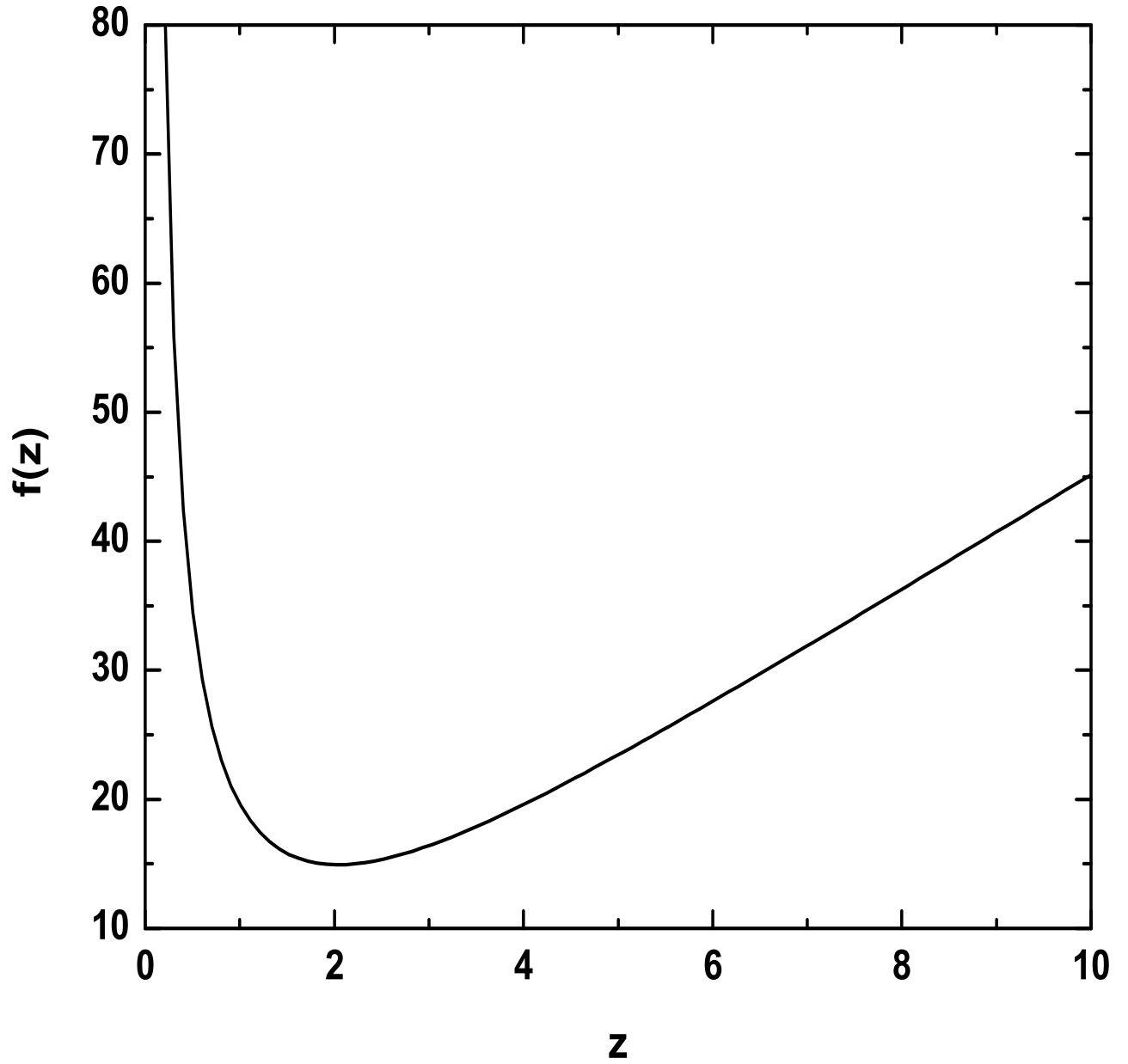$$s(\tau) = \frac{\epsilon + p}{T} = (1 + c_s^2)\sigma_{SB} T^3 \tag{2.94}$$

Figure 2.15: Characteristic function for calculation of temperature and chemical potential of baryon rich matter.

According to Eq. (2.81), the convolution $p^\mu d\Sigma_\mu$ has two contributions: 1) Integration along the slab trajectories as functions of τ; 2) η-integration along $\tau = const$ over space occupied by the baryon-free plasma. Different regions in the $\eta - \tau$ plane, occupied by the partonic plasma are schematically depicted in Fig. 2.16. The slab trajectories $\eta_t(\tau)$ and $\eta_p(\tau)$ are shown there too. In the Bjorken scaling expansion plasma particles propagate along trajectories $\eta = const$ and therefore can cross the slab trajectories at later times.

If these particles are absorbed by the baryonic slabs, the volume occupied by plasma is restricted by slab trajectories $\eta_a(\tau)$. In the other extreme, when plasma back reaction is not considered, produced partons are freely propagating across the slabs.

Usually parton spectra are calculated at some fixed proper time, corresponding to the freeze-out condition (the second horizontal line in Fig. 2.16). In this case the second term in Eq. (2.81) vanishes, and we have for the case when plasma back reaction is taken into account

$$\left.\frac{dN}{dy}\right|_{\tau=const} = \frac{\zeta(3)}{2\pi^2}\left(\nu_g + \frac{3}{4}\nu_q\right)\int d^2\mathbf{s} \int_{\eta_t(\tau)}^{\eta_p(\tau)} d\eta \frac{T^3\tau}{\cosh^2(y-\eta)} \qquad (2.95)$$

Since the temperature is a function of τ only (Bjorken's scaling), it can be taken out from the integral. Thus we have

$$\left.\frac{dN}{dy}\right|_{\tau=const} = \frac{\zeta(3)}{2\pi^2}\left(\nu_g + \frac{3}{4}\nu_q\right)\int d^2\mathbf{s}\, T^3(\tau)\tau\left[\tanh(\eta_p(\tau)-y) - \tanh(\eta_t(\tau)-y)\right]$$

$$(2.96)$$

Corresponding parton distributions calculated for different chromofield decay patterns are shown in the left panels of Figs. 2.17-2.19.

In the case of independent plasma and baryonic matter one should take into account that plasma is also present outside of the region between the slabs. The region of η integration is now wider: $-y_0 < \eta < y_0$. The difference between inside and outside regions is that between the slabs the chromofield is present, and due to its decay the entropy (baryon-free plasma) is continuously produced. Since the slab trajectories are not affected by the plasma, the slab deceleration effect is stronger. As the result, the region occupied by the chromofield is significantly smaller than in the case of strong plasma-slab interaction. The integration in region BC is done exactly as before and result is given by Eq. (2.96) with slab trajectories calculated accordingly. Outside the slabs there is no parton production and, therefore, the entropy is conserved, i.e.

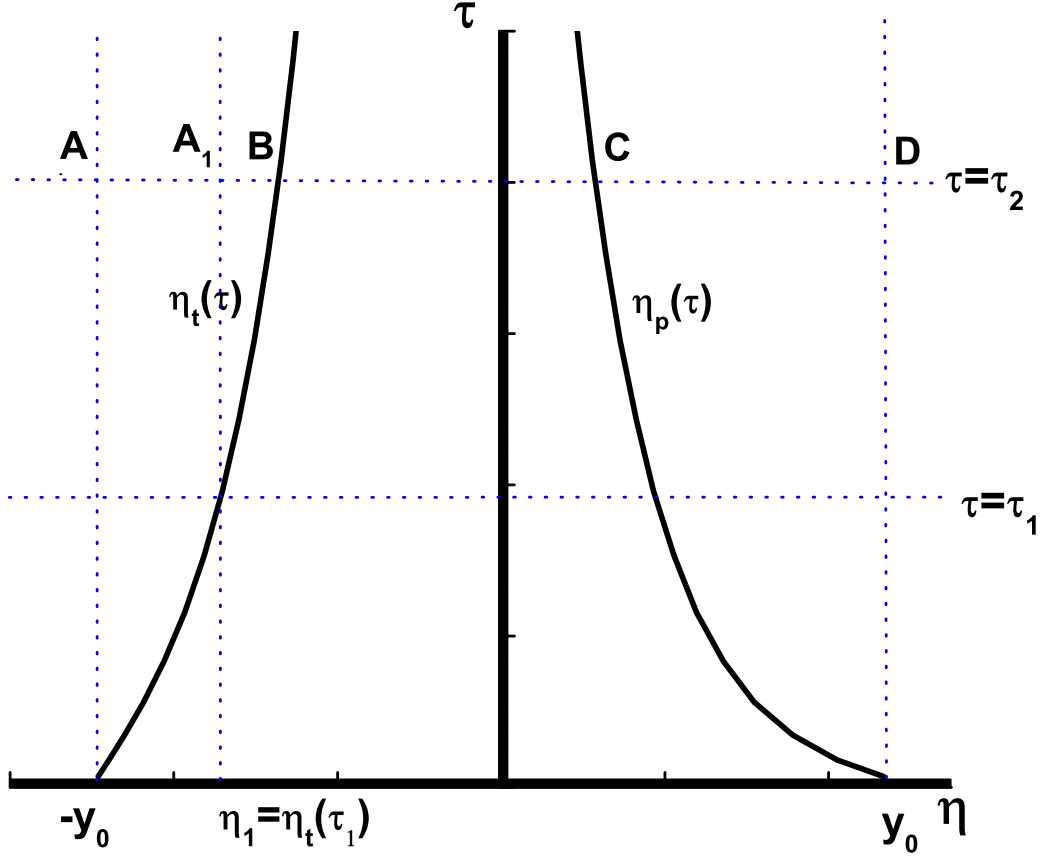$$\tau T^3(\tau) = const \qquad (2.97)$$

Figure 2.16: Illustrative figure for the calculations of partonic spectra at different assumptions concerning the back reaction of plasma on baryonic slabs (see text).

Hence, in regions AB and CD one should include plasma, which was produced earlier, and then expanded adiabatically after crossing the slab trajectory at certain proper time, say $\tau = \tau_1$. So the contribution from AB can be obtained by taking into account that in point A_1 the plasma temperature is

$$T_1^3(\tau) = T_1^3(\tau_1)\frac{\tau_1}{\tau} \tag{2.98}$$

Results for this case are presented in Fig. 2.17-2.19, right panels.

Following the above consideration one may come to the erroneous conclusion that the number of produced partons is larger in the case when the plasma back reaction is included (larger region occupied by chromofield). One should bear in mind, however, that a significant fraction of these partons is absorbed by the baryonic slabs. These partons will be emmited by

some kind of radiation in the baryon-rich environment at the decay of the baryonic slabs. This will happen at later stages of evolution which are out of scope of this work. When interaction of slabs and produced plasma is absent, all produced partons are freely propagating across the baryonic slabs and baryonic slabs are less excited. The overall energy difference between these two limiting cases is caused by the generation of the slab mass, additional to the mass gained at the initial stage of collision. This is clearly seen in Fig. 2.10: In the beginning of evolution, when slab deceleration is only due to the action of chromofield, the rapidity loss acheives its maximum value, but later, with gradual chromofield decay, the produced plasma is absorbed by the slabs, and they reaccelerate again. This leads, in turn, to increasing the slab mass, and regaining of their initially lost kinetic energy. Thus, there is no contradiction with the fact that kinetic energy lost by net-baryons in the case without the plasma back reaction is larger than in the case with plasma back reaction included.

This conclusion is confirmed by calculations of parton spectra displayed in Fig. 2.17-2.19. It is seen that maximum parton multiplicities at $y \sim 0$ are exactly the same in both cases, as it should be. One can see that reasonable values of rapidity density, $\frac{dN}{dy} \approx 10^3$ at $y \approx 0$ are obtained at ϵ_0 ranging from 0.5 GeV/fm^3(exponential decay) to 1.5 GeV/fm^3 (CGC decay). Generally, parton rapidity spectra predicted by our model are in good agreement with other models [27, 129]. Noticeable difference in the shape of $\frac{dN}{dy}$ appearers only at large y, where the plasma absorption effect might be important. This effect makes parton spectra broader, a nontrivial effect, which is not predicted by any other model. Therefore, the large y regions may contain important information about the plasma production mechanism.
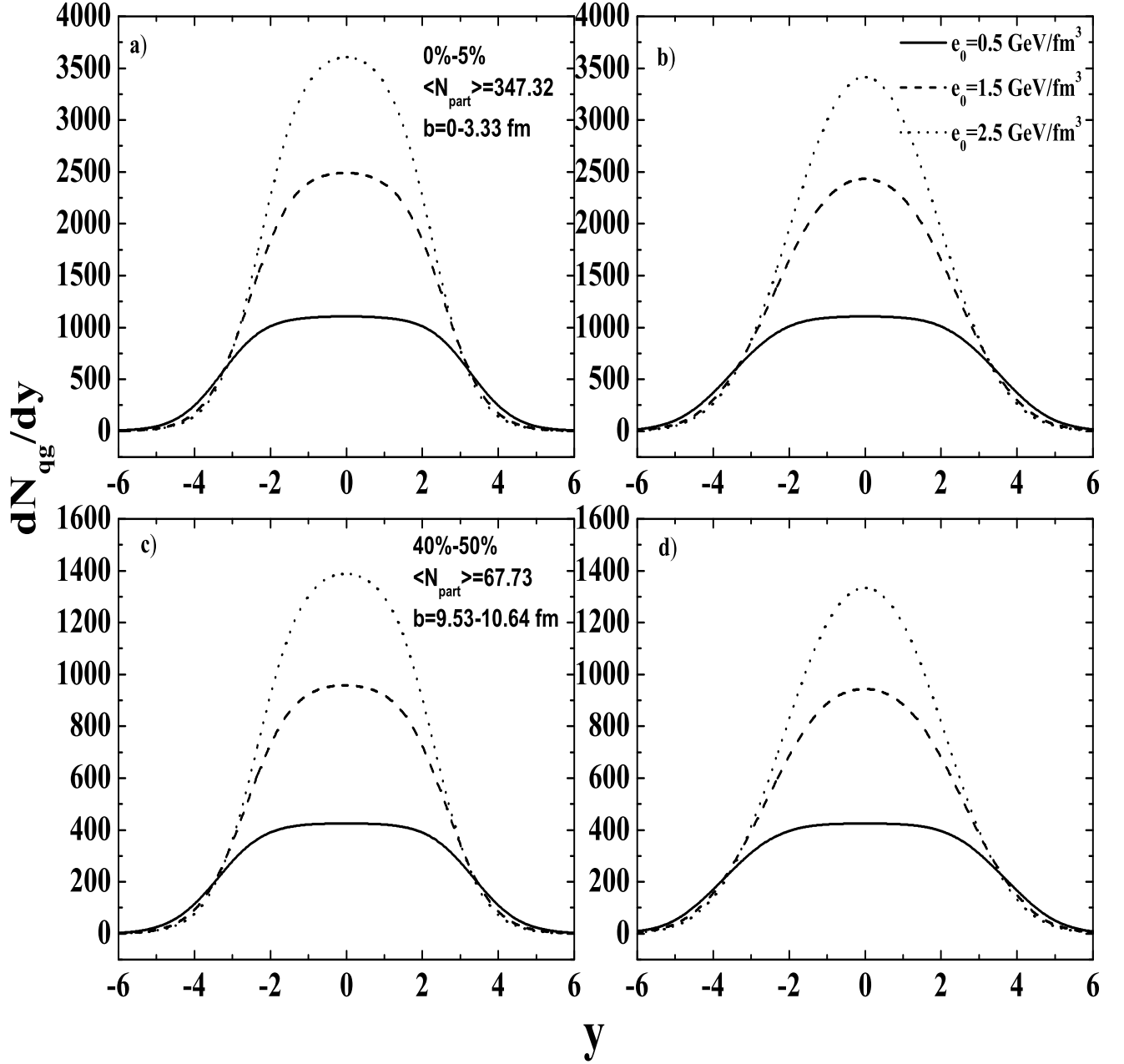
Figure 2.17: Parton rapidity distributions for Au+Au collisions at $\sqrt{s_{NN}} = 200$ AGeV, and different centralities calculated for different values of parameter ϵ_0 displayed in the figure. Exponential law of chromofield decay was chosen. Calculations, where back reaction of produced partonic plasma on slab dynamics was included, are displayed in the panels a),c), and, where it was not, in the panels b),d). Calculations are stopped at $\tau = 10$ fm.
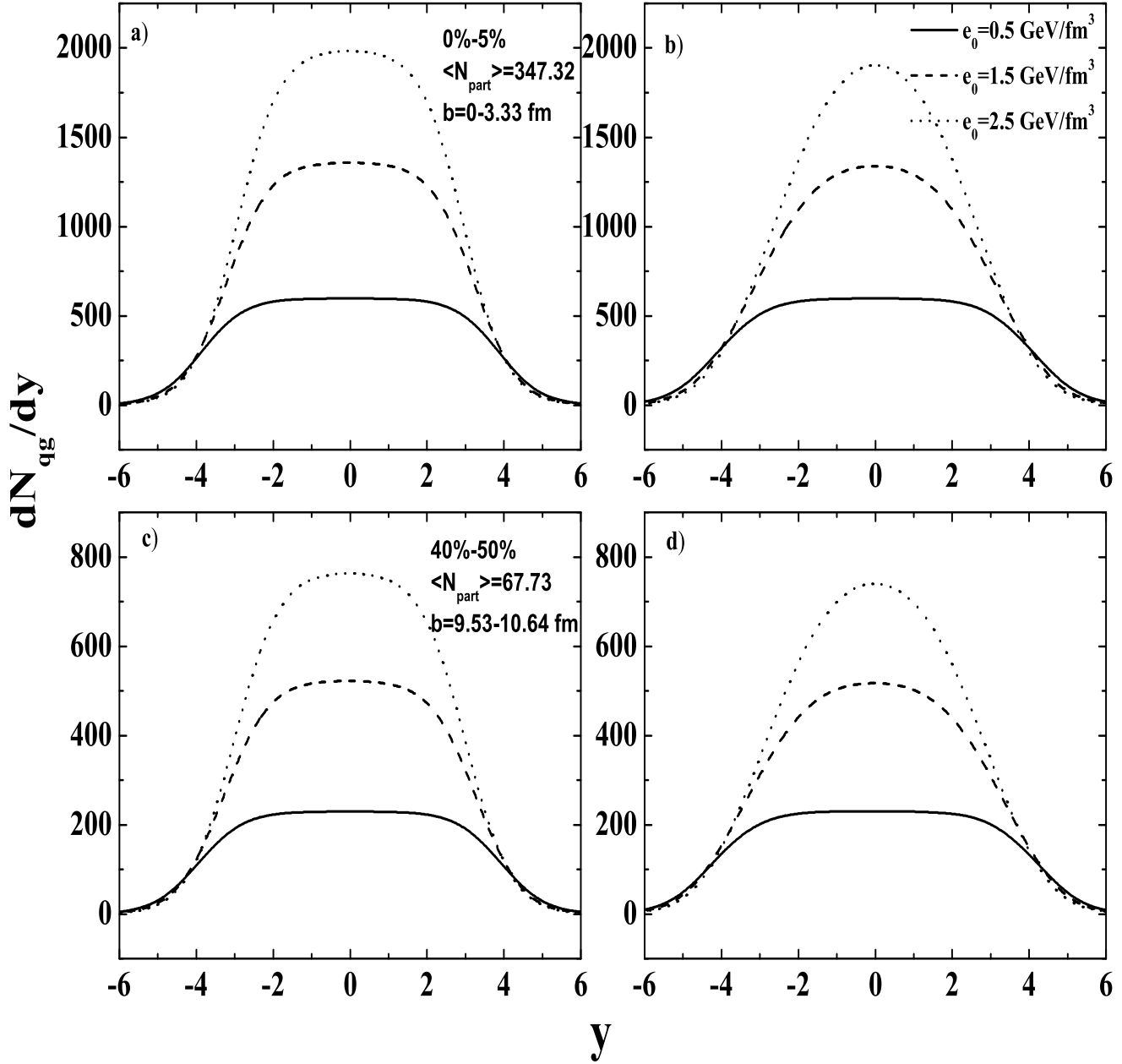
Figure 2.18: The same as Fig. 2.17 but for power law chromofield decay.
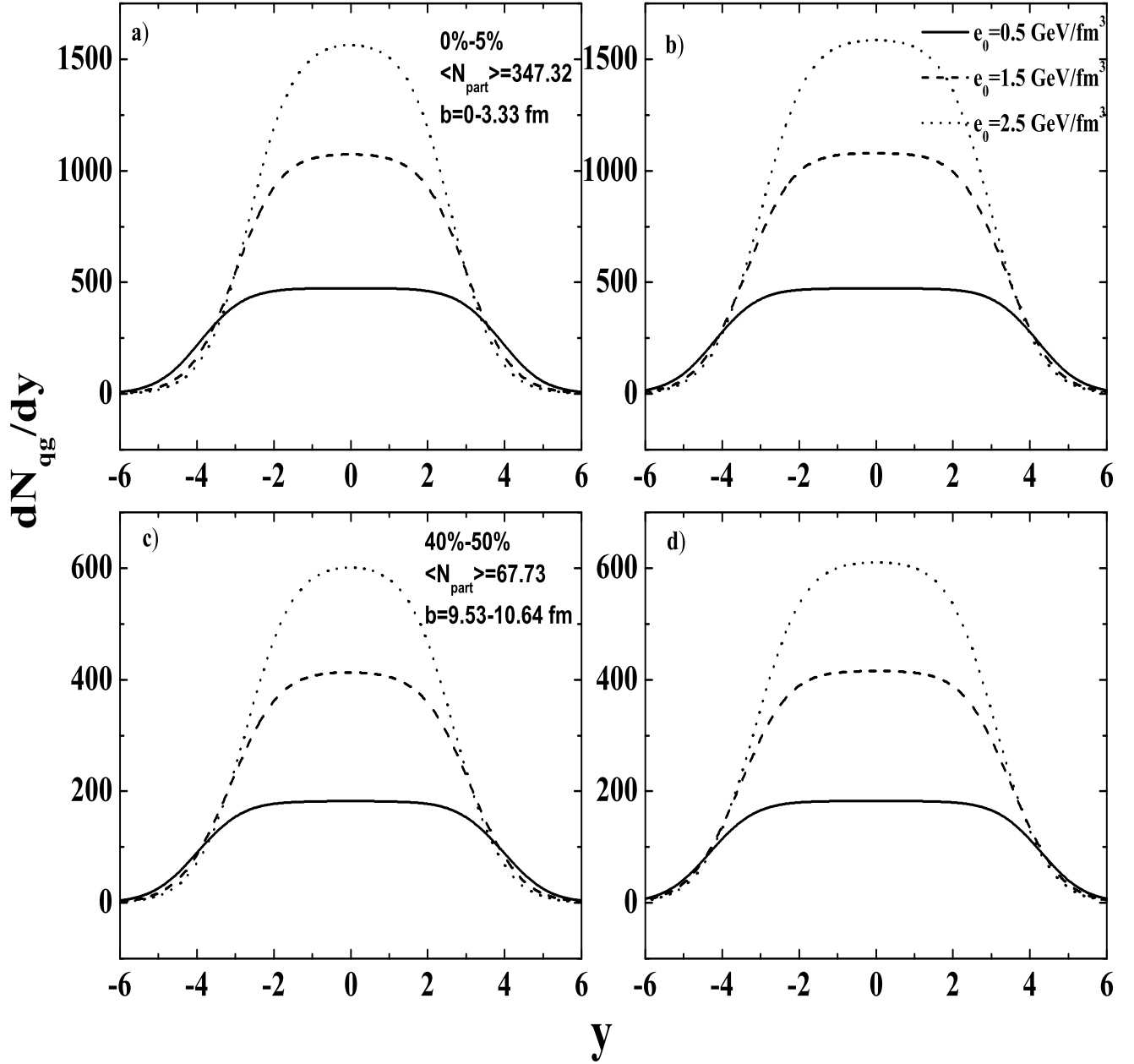
Figure 2.19: The same as Fig. 2.17 but for CGC chromofield decay.

Chapter 3

Summary

This thesis is devoted to the problem of baryon stopping in ultrarelativistic heavy-ion collisions. A new mechanism was proposed to describe net-baryon stopping phenomena. In this mechanism net-baryons are decelerated by strong chromofields, which are developed at the early stages of a heavy-ion collision.

We have divided the Lorentz contracted nuclei (nuclear sheets) into small slabs which interact pairwise. The QGP is produced as a result of the chromofield decay. Equations describing slab trajectories as well as time evolution of their masses and rapidities are derived from explicit energy-momentum conservation across the slab. The creation and evolution of the plasma was described by simple equations based on the Bjorken model with phenomenological source term responsible for chromofield decay. Stochastic nature of color charges based on the ideas of CGC was also taken into account. Different scenarios of chromofield decay were studied numerically. It was shown that due to the delayed QGP production the maximum of its energy density reaches only 20%-40% from the initial chromofield energy density. Baryon-rich as well as baryon-free components of the QGP are treated as an ideal fluids. Interaction between these fluids leads to increasing of slab temperature and therefore to increasing transverse momentum of baryons. It has been found that baryon-rich matter can be only heated up to some limited value.

Rapidity distributions of net-baryons and produced partons were calculated for different centralities. Averaging on centralities and calculation the number of participants was done in Glauber model. It has been demonstrated that taking into account fluctuations of color charges is not sufficient to reproduce the shape of net-baryon rapidity distribution in the midrapidity region by the only value of fitting parameter ϵ_0. In accordance with our analysis midrapidity region has larger initial chromofield energy density than

fragmentation region. The further step for improvement of our model is to take into account rapidity dependence of initial chromofield energy density. Calculations have been made for two limit cases: With and without back reaction of produced plasma. Agreement with BRAHMS data at $y \sim 0$ can be achieved only if we neglect the back reaction of the plasma. This was the main reason which led us to conclusion that the edge effects in the parton production are very important, i.e. the density of produced partons should be strongly reduced in the vicinity of the slabs. The net-baryon rapidity loss in Au+Au collisions at RHIC energy, $\langle \delta y \rangle \approx 2$, can be explained by the action of the chromofield with the initial energy density of about $35 GeV/fm^3$. Extrapolation to the LHC energy predicts $\langle \delta y \rangle \approx 3.9$, and initial field energy density around $95 GeV/fm^3$.

Bibliography

[1] A. Casher, H. Neuberger, and S. Nussinov, Phys. Rev. D **20** (1979);
N. K. Glendenning and T. Matsui, Nucl. Phys. **B245**, 449 (1984);
K. Kajantie and T. Matsui, Phys. Lett. **164B**, 373 (1985);
M. Gyulassy and A. Iwazaki, Phys. Lett. **165B**, 157 (1985).

[2] L. McLerran, and R. Venugopalan, Phys. Rev. D**49**, 2233 (1994); Phys. Rev. D **49**, 3352 (1994);
A. H. Mueller and J.Qui, Nucl. Phys. B **268**, 427 (1986).

[3] G. Gatoff, A. K. Kerman, and T. Matsui, Phys. Rev. D **36**, 114 (1987).

[4] K.J. Eskola and M. Gyulassy, Phys. Rev. C **47** 2329 (1993).

[5] L. Wilets, R.D. Puff, Phys. Rev. C**51**, 339-346 (1995).

[6] A. Kovner, L. McLerran, and H. Weigert, Phys. Rev. D **52**, 3809 (1995);
Phys. Rev. D **52**, 6231 (1995).

[7] S. A. Bass *et al.*, Prog. Part. Nucl. Phys. **41**, 225 (1998).

[8] W. Ehehalt, W. Cassing, Nucl. Phys. A **602**, 449 (1996).

[9] S. Hofmann *et al*, Phys. Lett. B **478**, 161-171(2000);
S.Sherer *et al.*, New J. Phys. **3**, 8 (2001).

[10] J.C. Collins and M.J. Perry, Phys. Rev. Lett. **34**, 1353 (1975);
P. Jaikumar, S. Reddy and A. W. Steiner, Phys. Rev. Lett. **96**, 041101 (2006).

[11] E. Fermi, Prog. Theor. Phys. **5**, 570 (1950).

[12] L. D. Landau, Izv. Akad. Nauk SSSR, ser. fiz., 17, 51 (1953).

[13] J. Bjorken, Phys. Rev. D**27**, 140 (1983).

[14] P. Braun-Munzinger, I. Heppe and J. Stachel, Phys.Lett.B **465**,15 (1999);
G. D. Yen and M.I.Gorenstein, Phys. Rev. C **59**, 2788 (1999);
F.Becattini *et al.*, Phys. Rev. C **64**, 024901 (2001);
W.Frolkowski, W.Broniowski and M.Michalec, Acta Phys. Polon. B **33**, 761 (2002).

[15] F. Becattini and U.W. Heinz, Z.Phys. C **76**, 269 (1997) [Erratum-ibid. C **76**, 578 (1997)];
F. Becattini, Z.Phys. C **69**, 485 (1996).

[16] G. Boyd *et al*, Phys. Rev. Lett. **75**, 4169-4172 (1995).

[17] Yu. B. Ivanov, V. N. Russkikh, and V. D. Toneev, Phys. Rev. C **73**, 044904 (2006).

[18] E.V. Shuryak and I.Zahed, Phys. Rev. C **70**, 021901 (2004).

[19] D.N. Voskresensky, Nucl. Phys. A **744**, 378 (2004).

[20] H.H.Gutbrod *et al.*, *FAIR Baseline Technical Report*, vol. 1

[21] A.N.Sisakyan *et al*, nucl-ex/0601034.

[22] A. S. Khvorostukhin, V. V. Skokov, V. D. Toneev, K. Redlich, Eur. Phys. J. C**48**, 531-543 (2006).

[23] Z. Fodor and S. D. Katz, J. High Energy Phys. **03**, 14 (2002); **04**, 50 (2004).

[24] R. Hakobyan, hep-ph/0012106.

[25] L.N. Lipatov, *Sov. J. Nucl. Phys.* **23**, 338 (1976);
E.A. Kuraev, L.N. Lipatov and V.S. Fadin, *Sov. Phys. JETP* **45**, 199 (1977);
Ya. Ya. Balitsky and L.N. Lipatov, *Sov. J. Nucl. Phys.* **28**, 822 (1978).

[26] V. N. Gribov, L. N. Lipatov, Sov. J. Nucl. Phys.**15**, 438, 675 (1972);
Y. L. Dokshitzer, Sov. Phys. JETP **46**, 641 (1977);
G. Altarelli, G. Parisi, Nucl. Phys. B **126**, 298 (1977).

[27] D. Kharzeev and E. Levin, Phys. Lett. B **523**, 79-87 (2001).

[28] L. McLerran, hep-ph/0202270; Nucl. Phys. A **699**, 73 (2002).

[29] A. H. Mller and V. N. Triatafyllopoulos, Nucl. Phys. B **640**, 331 (2002); V. N. Triatafyllopoulos, Nucl. Phys. B **648**, 293 (2003).

[30] M. Gyulassy, L. McLerran, Phys. Rev. C **56**, 2219 (1997).

[31] A. H. Mueller, Nucl. Phys. B **572**, 227 (2000).

[32] S.Jeon, R.Venugopalan, Phys. Rev. D **70**, 105012-1 (2004).

[33] R. Friedberg and T. D. Lee, Phys.Rev. D**15**, 1694 (1977); 16, 1096 (1977).

[34] M. Grabiak and M. Gyulassy, J. Phys. C**17**, 583 (1991).

[35] L. V. Gribov, E. M. Levin, and M. G. Ryskin, Phys. Rep. **100**, 1 (1983).

[36] R. I. Jaffe, Annals Phys. **132**, 32 (1981).

[37] N.S. Amelin, N. Armesto, C. Pajares, D. Souza, Eur. Phys. J. C **22**, 149 (2001).

[38] A. B. Kaidalov, K. A. Ter-Martirosyan, Phys. Lett. B**117**, 247 (1982).

[39] B. Anderson, G. Gustafson and T.Sjoestrand, Phys. Scrita **32**, 574 (1985).

[40] K. Itakura, Yu. Kovchegov, L. McLerran, D. Teaney, Nucl. Phys. A**730**,160 (2004).

[41] F.Lenz ,*Lectures on QCD. Applications* Springer-Verlag, 1997,vol.2

[42] R. D. Field and R. P. Feynman, Phys. Rev. D**15**, 2590 (1977); Nucl. Phys. B**136**, 1 (1978).

[43] G. Marchesini and B. R. Webber, Nucl. Phys. B**238**, 1 (1984); B. R. Webber, Nucl. Phys. B**238**, 492 (1984).

[44] B. Andersson *et al*, Z. Phys. C**1**, 105 (1979).

[45] B.Andersson, G.Gustafson, G.Ingelman, Phys.Rep. **97**, 31 (1983)

[46] B. Andersson *et al*, hep-ph/0212122.

[47] J. Schwinger, Phys. Rev. **82**, 664 (1951); F. Sauter, Z. Phys. **69**,742 (1931); W. Heisenberg and H. Euler, Z. Phys. **98**, 714 (1936).

[48] S. Schmidt *et al*, Int. J. Mod. Phys. E**7**, 709-722 (1998).

[49] R. C. Wang, C. Y. Wong, Phys. Rev. D **38**, 348 (1988).

[50] Th. Schoenfeld *et al*, Phys. Lett. B **247**, 5-12 (1990).

[51] P. Goddard, J. Goldstone, C. Rebbi, Charles B. Thorn, Nucl. Phys. **B56**, 109 (1973).

[52] C. Martin, D. Vautherin, Phys. Rev. D **38**, 3593 (1988).

[53] V. M. Mostepanenko, N. N. Trunov, *The Casimir Effect and its Appications* (Clarendon Press, Oxford, 1997), p. 53.

[54] K. Geiger, Nucl. Phys.**B 369**, 600-654 (1992).

[55] S. A. Bass, B. Mueller and D. K. Srivastava, Phys. Lett. B **551**, 277 (2003); Phys. Rev. Lett. **91**, 052302 (2003).

[56] Z. Xu, C. Greiner, Phys. Rev. C**71**, 064901 (2005).

[57] J. C. Collins, D. E. Sopper, G. Sterman, *Perturbative Quantum Chromodynamics* (World Scientific, Singapore, 1989).

[58] M. Hirai, S. Kumano, M. Miyama, Phys. Rev. D **64**, 034003 (2001).

[59] A. D. Martin *et al*, Eur. Phys. J. C **18**, 117-126 (2000).

[60] P. Romatschke, R. Venugopalan, Phys.Rev. Lett. **96**, 062302 (2006).

[61] D. I. Podolsky *et al*, Phys. Rev. D **73**, 023501 (2006).

[62] G. V. Dunne, arXiv: hep-th/0406216;
Shifman, M. (ed.) *et al: From fields to strings*, vol. 1, pp. 445-522, and references therein.

[63] S. A. Smolyansky *et al*, Phys. Part. Nucl. Lett. **2**, 293-299 (2005).

[64] V. V. Skokov *et al*, hep-ph/0210099.

[65] N.N. Bogoliubov, *The problems of dynamical theory in statistical mechanics* (Gostechizdat, Moscow, 1946).

[66] B. Zhang, Comput. Phys. Commun. **109**, 193 (1998).

[67] T.S.Biro Phys. Rev. C**48**, 1275 (1993).

[68] D. Kharzeev, E. Levin, and K. Tuchin, Phys. Rev.**C75**,044903(2007).

[69] L. McLerran, and R. Venugopalan, Phys. Rev. D **50**, 2225 (1994).

[70] G.Baym *et al*, Phys. Rev. Lett. **64**, 1867 (1990).

[71] T. Hirano and M. Gyulassy, Nucl. Phys. A **769**, 71-94 (2006).

[72] K. J. Eskola and H. Honkanen, Nucl. Phys. A **713**, 167 (2003).

[73] R. Baier, Yu. L. Dokshitzer, S. Peigne, D.Schiff, Phys. Lett. B**345**, 277 (1995).

[74] K. J. Eskola, B. Mller, X.N. Wang, Phys. Lett. B **374**, 20 (1996).

[75] J. I. Kapusta, Ch. Gale, *Finite-Temperature Field Theory: Principles and Applications* (Cambridge University Press, Cambridge, 2006).

[76] M. Bleicher and H. Stoecker, Phys. Lett. B **526**, 309-314 (2002).

[77] Yu. E. Pokrovsky, A. V. Selikhov, Nucl. Phys. A **525**, 669 (1991).

[78] E. S. Weibel, Phys. Rev. Lett. **2**, 83 (1959).

[79] P. Romatschke and A. Rebhan, Phys. Rev. Lett. **97**, 252301 (2006); M. Strickland, Nucl. Phys. A **785**, 50-57 (2007).

[80] M. Asakawa, S. A. Bass, and B. Mueller, Phys. Rev. Lett. **96**, 252301 (2006).

[81] U.-Th.Elze, U.Heinz, Phys.Rep **183**, 81 (1989).

[82] V. V. Skokov and V. D. Toneev, Phys. Rev. C **73**, 021902 (2006).

[83] S. R. Groot, *Relativistic Kinetic Theory: Principles and Applications*, (North Holland, 1980); U. Heinz, Ann. Phys.(N.Y.) **168**, 148 (1986); S. Mrowczynski, Acta Phys. Pol. B **19**, 91 (1988).

[84] F. Cooper and G. Frye, Phys. Rev. D **10**, 186 (1974).

[85] Cs. Anderlik *et al*, Phys. Rev. C **59**, 3309 (1999).

[86] L. V. Bravina *et al*, Phys. Lett. B **354**, 196 (1995).

[87] C. Adler *et al.*, STAR Collaboration, Phys. Rev. Lett. **87**, 082301 (2001); K. Adcox *et al.*, PHENIX Collaboration, *ibid.* **88**, 192302 (2002).

[88] V.S. Vladimirov, *Equations of mathematical physics*, (M. Dekker, 1971)

[89] S. M. Belozerkovsky, I. K. Lifanov, *Numerical methods in the singular and integral equations* (Nauka, 1985) (in Russian).

[90] S. A. Bass and A. Dumitru, Phys. Rev. C **61**, 064909 (2000);
D. Teaney, J. Lauret, and E. V. Shuryak, nucl-th/0110037.

[91] K. A. Bugaev, Phys. Rev. Lett. **90**, 252301 (2003).

[92] L. P. Csernai *et al*, Eur. Phys. J. A **25**, 65 (2005);
V. K. Magas *et al*, nucl-th/0702083.

[93] I.G. Bearden and BRAHMS Collaboration, Phys. Rev. Lett. (2004).

[94] E. V. Shuryak, Phys. Rep. **61**, 71-158 (1980).

[95] I.N. Mishustin, J.I. Kapusta, Phys. Rev. Lett. **88**, 112501 (2002).

[96] M. Glueck, E. Reya and A. Vogt, Z. Phys. C **67**, 433 (1995).

[97] D.Kharzeev, Phys. Lett. B **378**, 238 (1996).

[98] J. Ellis *et al*, Phys. Lett. B **233**, 223 (1989).

[99] S.E. Vance, M. Gyulassy, Phys. Rev. Lett. **83**, 1735 (1999).

[100] B.B. Back *et al*, Phys. Rev. Lett. **86**, 1970 (2001).

[101] L. P. Csernai *et al*, Phys. Rev. C **26**, 149 (1982);
A. Rosenhauer *et al*, Phys. Scripta **30**, 45 (1984); Z. Phys. A **326**, 213 (1987).

[102] K. Weber *et al.*, Nucl. Phys. A **515**, 747 (1990);
C. Fuchs and H. Wolter, Nucl. Phys. A **589**, 732 (1995).

[103] H. Sorge, H. Stoecker, and W. Greiner, Ann. Phys. **192**, 266 (1989).

[104] J. Aichelin and H. Stoecker, Phys, Lett. B **176**, 14 (1986);
C. Fuchs *et al*, Nucl. Phys. A **603**, 471 (1996).

[105] C. Tsallis, D. J. Bukman, Phys. Rev. E **54**, R2197 (1996);
G.Wolshin, Europhysics Lett., **74**(1), 29 (2006);
W.M. Alberico, P. Czerski, hep-ph/0510271.

[106] A. A. Amsden *et al*, Phys. Rev. C **17**, 2080 (1978);
R. B. Clare and D. Strottman, Phys. Rep. **141**, 177 (1986).

[107] Yu.B. Ivanov, I.N.Mishustin, L.M. Satarov, Nucl.Phys. **A433**, 713 (1985).

[108] L.M.Satarov, I.M. Mishustin, A.V. Merdeev, and H.Stoecker, Phys. Rev. C**75**, 024903 (2007).

[109] L. McLerran and R. Venugopalan, Phys. Rev. D **59**, 094002 (1999).

[110] S. Fortunato, F. Karsch, P. Petreczky, H. Satz, Phys.Lett. **B502**, 321 (2001).

[111] M.A. Braun, F. del Moral, and C. Pojares, Phys. Rev. C 65, 024907 (2002).

[112] L.D. Landau, I.M. Lifshitz, *The Classical Theory of Fields* (Pergamon Press, London, 1975).

[113] D. Kharzeev, M. Nardi, Phys. Lett. **B507**, 121 (2001).

[114] L.Frankfurt, G. Miller, M.Strickman, Annu. Rev. Nucl. Part.Sci. **44**, 501 (1994)

[115] L.Frankfurt, M.Strikman and Ch.Weiss hep-ph/0507286;

[116] W.H.Press et al., *Numerical Receipes on Fortran* (Cambridge University Press, 1988), p. 151.

[117] H.B. Nielsen and P. Olesen, Nucl. Phys. **B61**, 45 (1973).

[118] G. Martens, C. Greiner, S. Leupold and U. Mosel, Phys. Rev. D **70**, 116010 (2004).

[119] F. Gelis, K. Kajantie and T. Lappi, Phys. Rev. C **71**,024904 (2005).

[120] E. Kolb, M. Turner, *The Early Universe* (Addison-Wesley, Redwood City, California, 1990).

[121] A. Bialas, W. Czyz, A. Dyrek, W. Florkowski, Z. Phys. C **46**, 439 (1990).

[122] D. Kharzeev, C. Lourenco, M. Nardi, H. Satz, Z. Phys. C **74**, 307-318 (1997).

[123] L.P.Csernai, *Introduction to Relativistic Heavy Ion Collisions* (John Wiley&Sons, Ltd. 1994), p.88.

[124] A.Bialas and W.Czyz, Phys.Rev. **D 31**,198 (1985).

[125] T. Hiarano and Y. Nara, J.Phys. G**31**, S1-S14 (2005).

[126] A.S. Khvorostukhin et al., Eur. Phys. J. C**48**, 531 (2006); M. Stefanov, K. Rajagopal and E. Shuryak, Phys. Rev. D**60**, 114028 (1999).

[127] A.A. Grib, S.G. Mamaev, V.M. Mostepanenko, *Vacuum quantum effects in strong external fields*, (Atomizdat, Moscow,1988).

[128] C.Y. Wong, *Introduction to High Energy Heavy Ion Collisions*, (World Scientific, Singapore,1994),p.249

[129] T. Hiarano and Y. Nara, J.Phys. G**31**, S1-S14 (2005).

Curriculum Vitae

Family name: **Lyakhov** First name: **Konstantin**
Born: **5 July 1978** in Moscow

Address:
Frankfurt International Graduate School for Science, Goethe
University, Ruth-Moufang-Str. 1, D-60438 Frankfurt am Main,
Germany
Work telephone: +49 (069) 79847532
E-mail: lyakhov@fias.uni-frankfurt.de
lyakhov2000@yahoo.com

Doctor of natural philosophy in Theoretical Physics

Conferences and International Schools:

1)*"Quantum interacting particles systems", private communication "Bogoliubov's chain (hierarchy BBGKY) and the low density limit", September'2000, Levico Term (Italy)*
2)*"Lomonosov'2001", talk "Bogoliubov's chain in the Quantum Field Theory", April'2001, Moscow*
3)*"Lomonosov'2003", talk "Some questions of achieving thermodynamic equilibrium in the strongly interacting systems", April'2003, Moscow*
4)*"VIII International conference for nucleus-nucleus collisions" at the poster session with communication "Some questions of achieving thermodynamic equilibrium in the strongly interacting systems", June'2003, Moscow*
5)*"QCD (Quantum Chromodynamics) signatures in QGP (Quark Gluon Plasma)" January'2004, Hirschegg (Austria)*
6)*"Phase transitions and Critical Points in strongly interacting matter" Bergen (Norway) April'2005*
7)*"International Symposium on Heavy-Ion Physics" April'2006, Frankfurt*
8)*Dubna International School on Theoretical Physics "Dense Matter in Heavy Ion Collisions and Astrophysics", talk "Baryon Stopping by Strong Chromofields" 21-30 August'2006*
9)*"Dubna Advanced Summer School on Modern Mathematical Physics" 2-12 September'2006*
10)*Helmholtz Research School "Quark Matter Studies" 9 October'2006, Darmstadt*
11)*The Second International Symposium Atomic Clusters Collisions: Structure and Dynamics from the nuclear to the biological scale (ISACC2007), July"2007, Darmstadt (Germany)*
12)*Frankfurt International Graduate School on Neuro Science, August"2007*

EDUCATION: M.Sc. in Physics, **Moscow State University**, Moscow, Russia (22 January, 2001)

SKILLS: Fortran 77, 90, LaTeX, C, Maple, Mathematica, MatLab, OriginLab, MsOffice, OpenOffice, Perl, Shell, Linux, WindowsXP, MPI for Fortran

LANGUAGES: English(very good), German(poor)

EXPERIENCE: I have finished Independent Mathematical University at **Steklov's Mathematical Institute**. I've got diploma practice in the Mathematical Physics sub-department of the same Insitute. There topic of my research was focused on the problems of non-equilibrium relativistic kinetic theory and its application to the physics of Quark Gluon Plasma and explanation of Baryon Asymmetry of Universe under supervision of Corresponding Member the Russian Academy of Science (RAS) Dr. **Igor Volovich**. Title of my Master thesis was: " *Bogoliubov's chain* in the scalar Quantum Field Theory". Over three years I was a PhD student in the **Quantum Statistics and Field Theory Subdepartment** (2001 - 2004), where I was working under supervision of Academician of the RAS Victor Maslov. Topic of my research was "Generalization of semi-density equation for Quark Gluon Plasma(QGP)". In the same time I was teaching in seminars on Statistical physics and Quantum Field Theory. After June'2003 the topic of my PhD research was changed, because I've met my new advisor Prof. Dr. **Igor Mishustin** on the "*VIII International conference for nucleus-nucleus collisions"*. Since June'2004 and up to now I am working with him in the **Frankfurt International Graduate School for Science- FIGSS** at the **J.W.Goethe University**. My PhD project was "Baryon stopping and QGP production at RHIC and LHC".

Projects in other disciplines I've been involved: unfinished project on flame front stability conditions with Prof. Michael Liberman from Uppsala university (Sweden); unfinished project with Prof. Levich from Biological Department of MSU on the mathematical ecology.

FIGSS Courses:

1) Dr. Bratkovskaya and Prof. Igor Mishustin "Dynamical models of heavy-ion collisions"
2) Prof. Walter Greiner "Quantum Chromodynamics"
3) Dr. Berger, Dr. Holm, and Prof. A. Solov'yov "Theoretical descriptions of macromolecules". It was prepared review report on this course: "Polymer Physics Concepts Introduction"
4) Dr. M. Meyer-Hermann, Prof. H. Stöcker, Prof. J. Triesch "Theoretical Explorations in Immunology and Neuro-Science

PUBLICATIONS: Paper "Baryon stopping by strong chromofields" to be published in PEPAN Letters PEPAN 7 (2008): "Proceedings of Helmholtz Summer School "Dense Matter In Heavy Ion Collisions and Astrophysics" (hep-ph/0701115). Paper "Baryon deceleration by strong chromofields in ultra-relativistic heavy ion collisions" was published in Phys. Rev. C 76, 011603 (2007); big publication (50 pages) summarizing my PhD project: "Baryon stopping by strong chromofields" to be sent soon in the same journal. The paper "Baryon kinetic energy loss in the color flux tube model" is on the stage of preparation

SCIENTIFIC INTERESTS: Quark-gluon plasma; Equilibrium and non-equilibrium processes in high energy physics; Baryon asymmetry of Universe; Astrophysics; Plasma physics and Combustion theory; Quantum Computers; Condensed matter physics; Theoretical NeuroScience.